Università degli Studi di Torino
Doctoral School of the University of Torino
PhD Programme in Chemical and Materials Sciences XXXVI Cycle

Elucidating the deactivation pathways of Cu-zeolite-based industrial $DeNO_x$ catalysts by means of X-ray absorption spectroscopy

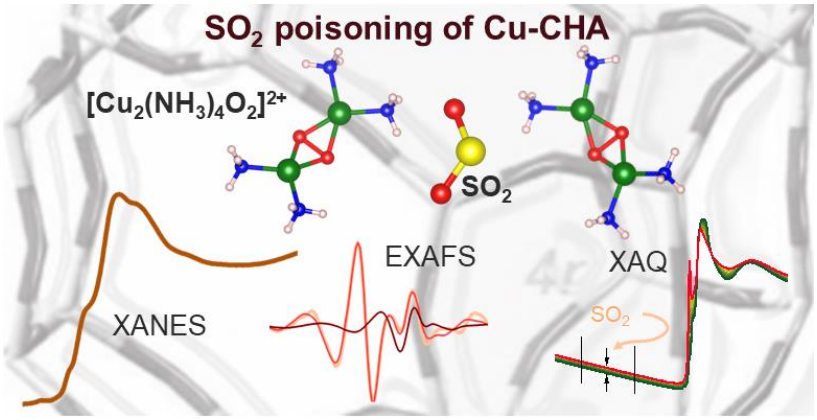

Anastasia Molokova

Supervisors:
Prof. Gloria Berlier
Dr. Kirill A. Lomachenko
Dr. Ton V.W. Janssens

Università degli Studi di Torino

Doctoral School of the University of Torino

PhD Programme in Chemical and Materials Sciences XXXVI cycle

Elucidating the deactivation pathways of Cu-zeolite-based industrial DeNO$_x$ catalysts by means of X-ray absorption spectroscopy

Candidate: **Anastasia Molokova**

Supervisor: Prof. **Gloria Berlier**
Università degli Studi di Torino
Dipartimento di Chimica

Dr. **Kirill A. Lomachenko**
European Synchrotron Radiation Facility
BM23/ID24 beamlines

Dr. **Ton V.W. Janssens**
Umicore Denmark ApS
Automotive Catalysts

Jury Members: Prof. **Lorenzo Mino**
Università degli Studi di Torino
Dipartimento di Chimica

Prof. **Andrew Beale**
University College London
Department of Chemistry

Dr. **Dmitry Doronkin**
Karlsruhe Institute of Technology
Institute for Catalysis Research and Technology

Head of the Doctoral School: Prof. Eleonora Bonifacio
PhD Programme Coordinator: Prof. Bartolomeo Civalleri

Torino, 2023

Table of Contents

1 Introduction

1.1 NO_x emission and NH_3 selective catalytic reduction (NH_3-SCR)

Air pollution is a significant global environmental issue. According to the World Health Organization (WHO), [1] every year, health risks caused by air pollution cause millions of deaths and the loss of healthy years of life. The recommended levels of harmful gases concentrations are often exceeded in highly populated areas, and mortality rates caused by air pollution continue to rise. [2] One of the important sources of air pollution is the emission of nitrogen oxides (NO_x) by diesel vehicles and industrial plants. Exposure to NO_x increases the risk of respiratory tract infections, aggregating the symptoms of respiratory diseases such as asthma and premature mortality risks. [3-6] The environmental impact of NO_x is also significant. [7, 8]

One of the major sources of NO_x emissions is diesel vehicles. The importance of reducing the emission of NO_x is a matter of concern at the European level. The Euro 6 regulation was introduced to achieve a substantial decrease in the emission of NO_x. [9] The necessity to meet the requirements outlined in the Euro 6 and the upcoming Euro 7 regulations and to make the air cleaner for better and longer lives[10] and for protecting the environment, drives the development and advancement of the technologies based on the selective catalytic reduction of NO_x by NH_3 in the diesel exhaust after-treatment systems. In this reaction, NO is selectively reduced to N_2 and H_2O by NH_3 in the presence of O_2, according to Equation (1.1).

$$4NO + 4NH_3 + O_2 \rightarrow 4N_2 + 6H_2O \quad (1.1)$$

In the diesel exhaust after-treatment system, the reaction takes place in the SCR catalyst. Cu-zeolites are efficient catalysts for this reaction, and the current state-of-the-art catalysts for this technology are based on Cu-chabazite (Cu-CHA). Such catalysts are commercially available for application in vehicles.

1.2 Cu-CHA as a catalyst for NH_3-SCR

The structure of the Cu-CHA has been actively studied for decades. [11-13] The chabazite is a porous material. The pores consist of layers of double six-membered rings (d6r), which are bound by units of four-member rings (4r). The blocks of two 6r layers are connected by the combination of 4r and eight-member rings (8r) (Figure 1.1). [12] The building units consist of Si^{4+} coordinated to oxygen atoms. If Al^{3+} replaces Si^{4+}, it creates a negative charge in the framework. These negative charges must be balanced by positively charged ions, which gives the zeolite the capability of ion exchange. In the case of Cu-CHA, Cu atoms compensate for the negative charge. Cu atoms work as active centers in NH_3-SCR catalytic cycle. [14-22]

In the NH_3-SCR reaction, the Cu-CHA catalyst demonstrates good low-temperature activity and hydrothermal stability. [12, 23-25] To describe the mechanism of the NH_3-SCR, two temperature regions are usually discussed: 180-300 °C corresponds to low-temperature SCR, and 350-550 °C corresponds to high-temperature SCR. One of the main advantages of Cu-CHA compared to other catalysts is its good low-temperature activity.

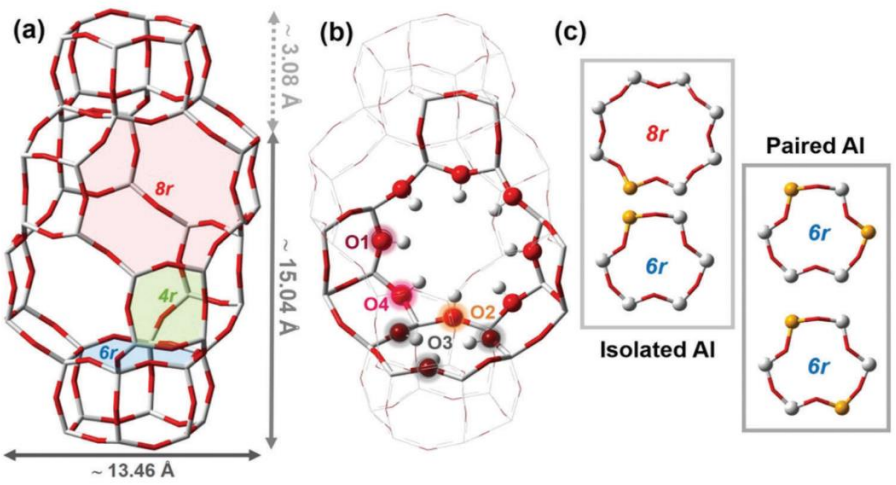

Figure 1.1 (a) Schematic representation of CHA topology, underlining the presence of 4r, 6r and 8r rings and the major dimension of the cages. (b) Illustration of the four different oxygens available in the framework. (c) Possibilities of isolated and paired Al sites, considered in the literature as most probable locations for Cu cations. Colour code: O red; Si grey; Al orange in case of zeolites (CHA or SSZ-13). Reproduced from Borfecchia et al., 2018 [12]

The proposed mechanism of the NH_3-SCR in Cu-CHA is a redox cycle. [16, 26] The oxidation state of Cu active centers changes between Cu^I and Cu^{II}. The reduction of Cu takes place in the presence of NO and NH_3. At low temperatures, it results in the formation of mobile $[Cu^I(NH_3)_2]^+$ complexes. [19, 23, 27] At high temperatures Cu^I is bound to the framework (fw-Cu^I). In the presence of oxygen in the low-temperature region, mobile $[Cu^I(NH_3)_2]^+$ complexes can form Cu pairs in peroxo $[Cu_2^{II}(NH_3)_4O_2]^{2+}$ complexes. [18, 20, 26, 28-31] Then the $[Cu_2^{II}(NH_3)_4O_2]^{2+}$ complexes are reduced back by NH_3 and NO with the formation of the reaction products N_2 and H_2O. The low temperature NH_3-SCR reaction cycle directly depends on the mobility of $[Cu^I(NH_3)_2]^+$ complexes enabling the formation of the Cu pairs required for O_2 activation. The reaction cycle includes the formation

of many different Cu-species formed by adsorption and the reaction of NO, NH_3, and O_2 as ligands inside the pores of the CHA zeolite. [18]

1.3 SO_2 poisoning of the Cu-CHA

Despite the advantages of the Cu-CHA catalyst for low-temperature NH_3-SCR, its performance is limited by the presence of SO_2 in the diesel exhaust gas. Depending on the regional fuel quality, the concentration of S in the diesel exhaust may reach 10 ppm, which is still within the Euro 6 standards. This results in the formation of 0.5-2 ppmv of SO_2 in the exhaust gas. Long-term exposure to SO_2, even in such small concentrations, significantly damages the exhaust after-treatment system, including the SCR system. The sensitivity of the Cu-CHA catalyst to SO_2 at temperatures below 300 °C is a severe challenge for its application in NH_3-SCR. [32-38]

The effect of SO_2 poisoning on the performance of the Cu-CHA catalyst depends on the exposure temperature. Figure 1.2a shows the decrease of NO_x conversion by Cu-CHA in the case of exposure to 100 ppmv SO_2 as a function of reaction temperature. Indeed, the decrease in the NO_x conversion is especially strong in the low-temperature region (Figure 1.2a). [32] High-temperature activity is much less affected by SO_2 poisoning.

Various studies show that the activity of SO_2-poisoned Cu-CHA catalyst can be partially restored by heating the catalyst to 500-550 °C. However, 5-15 % of the deactivation remains. This remaining deactivation corresponds to irreversible deactivation as opposed to reversible deactivation, which can be removed by heating. [32, 39, 40] Figure 1.2b shows the reversible and irreversible part of the deactivation in different

poisoning conditions. The nature of the reversibility of the deactivation remains not understood.

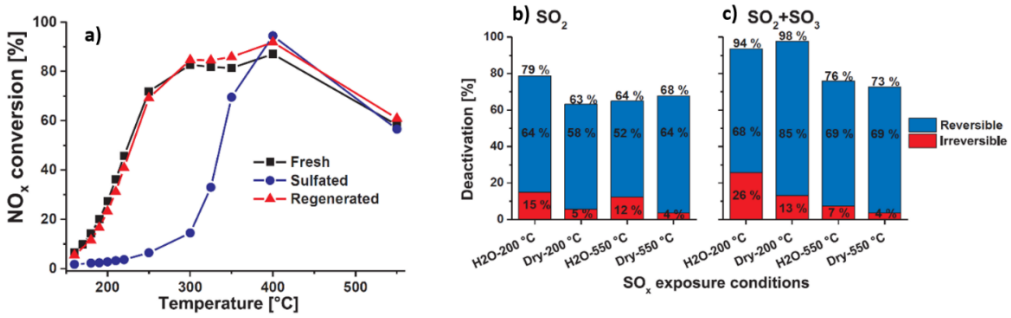

Figure 1.2 a) NO_x conversion as function of temperature of a Cu-CHA catalyst (Si/Al=14.7, Cu/Al=0.5, and 2.8 wt% Cu) in fresh, sulfated and regenerated state. SCR conditions: 500 ppmv NO, 530 ppmv NH_3, 10 % O_2, 5 % H_2O, N_2 balance to 0.225 NL/min on 5.0 mg catalyst in reactor with an inner diameter of 2 mm. SO_x exposure conditions: 100 ppmv SO_2, 16 % O_2, N_2 balance to 0.2 NL/min for 16 h at 550 °C. Regeneration conditions: 4.6 h at 550 °C in SCR-gas. b,c) The reversible deactivation (blue bars), irreversible deactivation (red bars) and total deactivation (sum of red and blue bars) plotted for each SO_x exposure condition of the Cu-CHA/cordierite catalysts. b) samples exposed to 100 ppmv SO_2, c) samples exposed to 70 ppmv SO_2 and 30 ppmv SO_3. Reproduced from Hammershoi et al., 2018 [32].

Another critical factor for the SO_2 poisoning of Cu-CHA catalyst is the gas composition during the poisoning. If oxygen is present in the gas mixture with SO_2, sulfur can oxidize and form SO_3, which causes similar deactivation of Cu-CHA catalyst, but on a larger scale (Figure 1.2 b,c). [32, 34, 39]

A complete scheme of the SO_2 poisoning of Cu-CHA is still under investigation. One of the proposed mechanisms considers the physical cause of the deactivation of the Cu-CHA. A recent theoretical study [33] suggests that upon exposure to SO_2, the NH_3-SCR catalytic cycle

completes with the formation of several S-containing Cu species and sulfuric acid H_2SO_4 (Figure 1.3). In the presence of NH_3, sulfuric acid can form ammonium bisulfate $HSO_4(NH_4)$, which is considered a primary factor of the deactivation preventing the diffusion of mobile $[Cu^{I}(NH_3)_2]^+$ species for the formation of the $[Cu_2^{II}(NH_3)_4O_2]^{2+}$ complex. This effect was proposed to cause the reversible deactivation of Cu-CHA as opposed to the irreversible deactivation [32] caused by the formation of S-containing Cu-species not participating in the low-temperature SCR catalytic cycle. Ammonium sulfate was also suggested as one of the possible species forming in the catalyst cages preventing the mobility of Cu species. [41-43]

Another proposed mechanism includes the formation of the S-containing Cu species such as Cu sulfate, [42, 43] and Cu bisulfate. [41, 44] These S-containing Cu species are proposed to make the Cu active sites unavailable for the NH_3-SCR redox cycle. Some studies also focus on the Cu oxidation state and the structure of Cu species as critical factors defining the deactivation mechanism. They show that SO_2 might absorb better on Cu^{I} than on Cu^{II} using the Density Functional Theory (DFT) calculations. [41, 45]

Although many publications and studies discussed the deactivation of Cu-CHA by SO_2, most of the studies either focused on overall effect of SO_2 poisoning on the activity of the catalysts or used pre-sulfated samples. This brings us to the objectives of this work, monitoring the deactivation of Cu-CHA catalyst by SO_2 in situ and studying the active sites on the atomic scale.

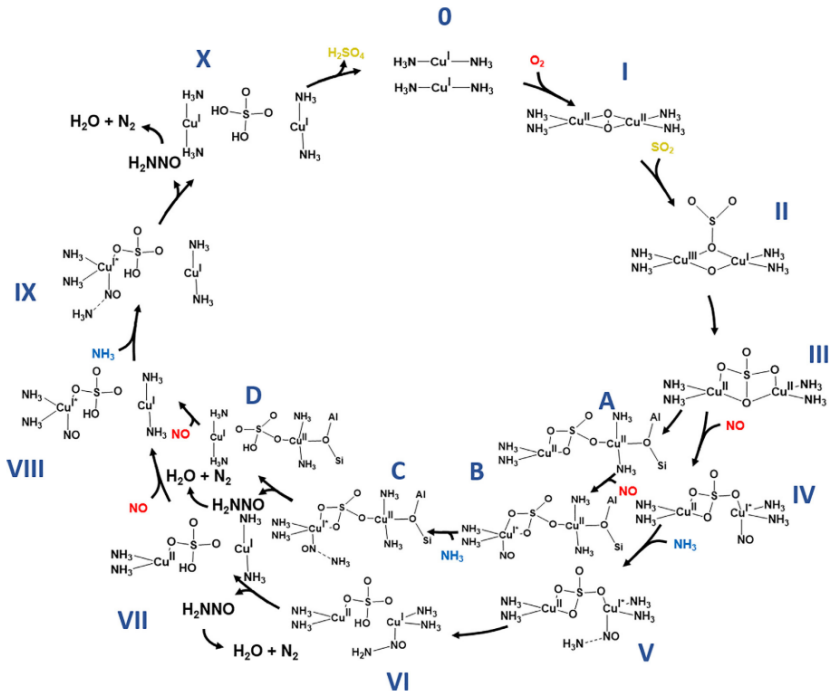

Figure 1.3 Proposed reaction cycle for low temperature NH_3-SCR in the presence of SO_2. The oxidation state for Cu is indicated. Al-O-Si represents a negative charge on the framework, and is only shown if the $[Cu^{I}(NH_3)_2]^+$ complex is chemically bound to the framework. Oxidation state of I* indicate an intermediate oxidation state between I and II with magnetic moment of 0.2–0.3. H_2SO_4 is formed during the SCR reaction. Reproduced from Feng et al., 2021[33]

1.4 Objectives

In the Introduction, it was discussed that in the NH_3-SCR redox cycle, Cu undergoes changes in its oxidation state between Cu^{I} and Cu^{II}, resulting in various Cu species when NO, O_2, and NH_3 are present in the gas mixture. To understand the deactivation of Cu-CHA catalyst by SO_2, studying the reactivity of individual Cu species towards SO_2 is crucial. This can be achieved by monitoring Cu oxidation state and the local environment

during exposure to different Cu species and SO_2. Chapter 3 reports the results of this part of the study.

The next step is the analysis of the products of the reaction between SO_2 and the sensitive Cu species. In Chapter 4, a detailed analysis of the structure of the SO_2-poisoned species is presented. Additionally, the mechanism of their formation is proposed.

One of the critical points of the reaction cycle is the interaction of the peroxo $[Cu_2^{II}(NH_3)_4O_2]^{2+}$ complexes with NO. Chapter 5 reports the changes in this reaction for the fresh and SO_2-poisoned Cu-CHA catalyst. The kinetics study of the reaction on the fresh and poisoned catalysts provides evidence of the chemical poisoning of the Cu-CHA catalyst by SO_2.

Finally, Chapter 6 contains a summary and conclusions of this study on the deactivation of Cu-CHA catalyst by SO_2. The report on the Ph.D. activities, including published articles and contributions to conferences can be found in Chapter 7. In Chapter 8, I would like to thank everyone involved in the project and my PhD journey. Chapter 9 presents the copies of the published articles.

1.5 References

1. World Health, O., *WHO global air quality guidelines: particulate matter (PM2.5 and PM10), ozone, nitrogen dioxide, sulfur dioxide and carbon monoxide*. World Health Organization: Geneva, 2021.
2. Spiteri, J.; von Brockdorff, P., Transboundary air pollution and respiratory disease mortality: evidence from European countries. *Journal of Economic Studies* **2021,** *48* (7), 1371-1387.

3. Chen, T.-M.; Kuschner, W. G.; Gokhale, J.; Shofer, S., Outdoor Air Pollution: Nitrogen Dioxide, Sulfur Dioxide, and Carbon Monoxide Health Effects. *The American Journal of the Medical Sciences* **2007,** *333* (4), 249-256.
4. Gillespie-Bennett, J.; Pierse, N.; Wickens, K.; Crane, J.; Howden-Chapman, P.; and the Housing, H.; Health Study Research, T., The respiratory health effects of nitrogen dioxide in children with asthma. *European Respiratory Journal* **2011,** *38* (2), 303.
5. Jonson, J. E.; Borken-Kleefeld, J.; Simpson, D.; Nyíri, A.; Posch, M.; Heyes, C., Impact of excess NOx emissions from diesel cars on air quality, public health and eutrophication in Europe. *Environmental Research Letters* **2017,** *12* (9).
6. Demetriou, E.; Hadjistassou, C., Lowering mortality risks in urban areas by containing atmospheric pollution. *Environ Res* **2022,** *211*, 113096.
7. Bray, C. D.; Battye, W. H.; Aneja, V. P.; Schlesinger, W. H., Global emissions of NH(3), NO(x), and N(2)O from biomass burning and the impact of climate change. *J Air Waste Manag Assoc* **2021,** *71* (1), 102-114.
8. Grewe, V.; Dahlmann, K.; Matthes, S.; Steinbrecht, W., Attributing ozone to NOx emissions: Implications for climate mitigation measures. *Atmospheric Environment* **2012,** *59*, 102-107.
9. *Official Journal of the European Union*; 2007.
10. Mulholland, E.; Miller, J.; Bernard, Y.; Lee, K.; Rodríguez, F., The role of NOx emission reductions in Euro 7/VII vehicle emission standards to reduce adverse health impacts in the EU27 through 2050. *Transportation Engineering* **2022,** *9*.
11. Beale, A. M.; Gao, F.; Lezcano-Gonzalez, I.; Peden, C. H.; Szanyi, J., Recent advances in automotive catalysis for NOx emission control by small-pore microporous materials. *Chem Soc Rev* **2015,** *44* (20), 7371-405.
12. Borfecchia, E.; Beato, P.; Svelle, S.; Olsbye, U.; Lamberti, C.; Bordiga, S., Cu-CHA - a model system for applied selective redox catalysis. *Chem. Soc. Rev.* **2018,** *47* (22), 8097-8133.
13. Dent, L. S.; Smith, J. V., Crystal Structure of Chabazite, a Molecular Sieve. *Nature* **1958,** *181* (4626), 1794-1796.
14. Borfecchia, E.; Lomachenko, K. A.; Giordanino, F.; Falsig, H.; Beato, P.; Soldatov, A. V.; Bordiga, S.; Lamberti, C., Revisiting the nature of Cu-sites in activated Cu-SSZ-13 catalyst for SCR reaction. *Chem. Sci.* **2015,** *6*, 548-563.
15. Borfecchia, E.; Negri, C.; Lomachenko, K. A.; Lamberti, C.; Janssens, T. V. W.; Berlier, G., Temperature-dependent dynamics of NH3-derived Cu species in the Cu-CHA SCR catalyst. *React Chem Eng* **2019,** *4* (6), 1067-1080.
16. Chen, L.; Janssens, T. V. W.; Vennestrom, P. N. R.; Jansson, J.; Skoglundh, M.; Gronbeck, H., A Complete Multisite Reaction Mechanism for Low-Temperature NH3-SCR over Cu-CHA. *ACS Catal.* **2020,** *10* (10), 5646-5656.

17. Fahami, A. R.; Günter, T.; Doronkin, D. E.; Casapu, M.; Zengel, D.; Vuong, T. H.; Simon, M.; Breher, F.; Kucherov, A. V.; Brückner, A.; Grunwaldt, J. D., The dynamic nature of Cu sites in Cu-SSZ-13 and the origin of the seagull NOx conversion profile during NH3-SCR. *React Chem Eng* **2019,** *4* (6), 1000-1018.
18. Janssens, T. V. W.; Falsig, H.; Lundegaard, L. F.; Vennestrom, P. N. R.; Rasmussen, S. B.; Moses, P. G.; Giordanino, F.; Borfecchia, E.; Lomachenko, K. A.; Lamberti, C.; Bordiga, S.; Godiksen, A.; Mossin, S.; Beato, P., A Consistent Reaction Scheme for the Selective Catalytic Reduction of Nitrogen Oxides with Ammonia. *ACS Catal.* **2015,** *5* (5), 2832-2845.
19. Millan, R.; Cnudde, P.; van Speybroeck, V.; Boronat, M., Mobility and Reactivity of Cu+ Species in Cu-CHA Catalysts under NH3-SCR-NOx Reaction Conditions: Insights from AIMD Simulations. *JACS Au* **2021,** *1* (10), 1778-1787.
20. Negri, C.; Selleri, T.; Borfecchia, E.; Martini, A.; Lomachenko, K. A.; Janssens, T. V. W.; Cutini, M.; Bordiga, S.; Berlier, G., Structure and Reactivity of Oxygen-Bridged Diamino Dicopper(II) Complexes in Cu-Ion-Exchanged Chabazite Catalyst for NH3-Mediated Selective Catalytic Reduction. *J. Am. Chem. Soc.* **2020,** *142* (37), 15884-15896.
21. Paolucci, C.; Parekh, A. A.; Khurana, I.; Di Iorio, J. R.; Li, H.; Caballero, J. D. A.; Shih, A. J.; Anggara, T.; Delgass, W. N.; Miller, J. T.; Ribeiro, F. H.; Gounder, R.; Schneider, W. F., Catalysis in a Cage: Condition-Dependent Speciation and Dynamics of Exchanged Cu Cations in SSZ-13 Zeolites. *J. Am. Chem. Soc.* **2016,** *138* (18), 6028-6048.
22. Villamaina, R.; Liu, S.; Nova, I.; Tronconi, E.; Ruggeri, M. P.; Collier, J.; York, A.; Thompsett, D., Speciation of Cu Cations in Cu-CHA Catalysts for NH3-SCR: Effects of SiO2/AlO3 Ratio and Cu-Loading Investigated by Transient Response Methods. *ACS Catal.* **2019,** *9* (10), 8916-8927.
23. Lomachenko, K. A.; Borfecchia, E.; Negri, C.; Berlier, G.; Lamberti, C.; Beato, P.; Falsig, H.; Bordiga, S., The Cu-CHA deNO_x catalyst in action: temperature-dependent NH_3-assisted selective catalytic reduction monitored by operando XAS and XES. *J. Am. Chem. Soc.* **2016,** *138* (37), 12025−12028.
24. Wu, Y.; Andana, T.; Wang, Y.; Chen, Y.; Walter, E. D.; Engelhard, M. H.; Rappé, K. G.; Wang, Y.; Gao, F.; Menon, U.; Daya, R.; Trandal, D.; An, H.; Zha, Y.; Kamasamudram, K., A comparative study between real-world and laboratory accelerated aging of Cu/SSZ-13 SCR catalysts. *Applied Catalysis B: Environmental* **2022,** *318*.
25. Peden, C. H. F., Cu/Chabazite catalysts for 'Lean-Burn' vehicle emission control. *J. Catal.* **2019,** *373*, 384-389.
26. Feng, Y.; Wang, X.; Janssens, T. V. W.; Vennestrøm, P. N. R.; Jansson, J.; Skoglundh, M.; Grönbeck, H., First-Principles Microkinetic Model for Low-Temperature NH3-Assisted Selective Catalytic Reduction of NO over Cu-CHA. *ACS Catal.* **2021**, 14395-14407.

27. Pankin, I. A.; Issa Hamoud, H.; Lomachenko, K. A.; Rasmussen, S. B.; Martini, A.; Bazin, P.; Valtchev, V.; Daturi, M.; Lamberti, C.; Bordiga, S., Cu- and Fe-speciation in a composite zeolite catalyst for selective catalytic reduction of NOx: insights from operando XAS. *Catal. Sci. Technol.* **2021,** *11* (3), 846-860.
28. Gao, F.; Mei, D.; Wang, Y.; Szanyi, J.; Peden, C. H., Selective Catalytic Reduction over Cu/SSZ-13: Linking Homo- and Heterogeneous Catalysis. *J Am Chem Soc* **2017,** *139* (13), 4935-4942.
29. Paolucci, C.; Khurana, I.; Parekh, A. A.; Li, S. C.; Shih, A. J.; Li, H.; Di Iorio, J. R.; Albarracin-Caballero, J. D.; Yezerets, A.; Miller, J. T.; Delgass, W. N.; Ribeiro, F. H.; Schneider, W. F.; Gounder, R., Dynamic multinuclear sites formed by mobilized copper ions in NOx selective catalytic reduction. *Science* **2017,** *357* (6354), 898-903.
30. Martini, A.; Negri, C.; Bugarin, L.; Deplano, G.; Abasabadi, R. K.; Lomachenko, K. A.; Janssens, T. V. W.; Bordiga, S.; Berlier, G.; Borfecchia, E., Assessing the Influence of Zeolite Composition on Oxygen-Bridged Diamino Dicopper(II) Complexes in Cu-CHA DeNOx Catalysts by Machine Learning-Assisted X-ray Absorption Spectroscopy. *J Phys Chem Lett* **2022,** *13* (26), 6164-6170.
31. Negri, C.; Martini, A.; Deplano, G.; Lomachenko, K. A.; Janssens, T. V. W.; Borfecchia, E.; Berlier, G.; Bordiga, S., Investigating the role of Cu-oxo species in Cu-nitrate formation over Cu-CHA catalysts. *Phys Chem Chem Phys* **2021,** *23* (34), 18322-18337.
32. Hammershoi, P. S.; Jangjou, Y.; Epling, W. S.; Jensen, A. D.; Janssens, T. V. W., Reversible and irreversible deactivation of Cu-CHA NH3-SCRcatalysts by SO2 and SO3. *Appl. Catal. B: Environ* **2018,** *226*, 38-45.
33. Bjerregaard, J. D.; Votsmeier, M.; Grönbeck, H., Mechanism for SO2 poisoning of Cu-CHA during low temperature NH3-SCR. *J. Catal.* **2023,** *417*, 497-506.
34. Cheng, Y. S.; Lambert, C.; Kim, D. H.; Kwak, J. H.; Cho, S. J.; Peden, C. H. F., The different impacts of SO2 and SO3 on Cu/zeolite SCR catalysts. *Catal. Today* **2010,** *151* (3-4), 266-270.
35. Hammershoi, P. S.; Jensen, A. D.; Janssens, T. V. W., Impact of SO2-poisoning over the lifetime of a Cu-CHA catalyst for NH3-SCR. *Appl. Catal. B: Environ* **2018,** *238*, 104-110.
36. Mesilov, V. V.; Bergman, S. L.; Dahlin, S.; Yang, X.; Xi, S. B.; Ma, Z. R.; Lian, X.; Wei, C.; Pettersson, L. J.; Bernasek, S. L., Differences in oxidation-reduction kinetics and mobility of Cu species in fresh and SO2-poisoned Cu-SSZ-13 catalysts. *Appl. Catal. B-Environ.* **2021,** *284*.
37. Zhang, L.; Wang, D.; Liu, Y.; Kamasamudram, K.; Li, J.; Epling, W., SO2 poisoning impact on the NH3-SCR reaction over a commercial Cu-SAPO-34 SCR catalyst. *Applied Catalysis B: Environmental* **2014,** *156-157*, 371-377.

38. Wijayanti, K.; Leistner, K.; Chand, S.; Kumar, A.; Kamasamudram, K.; Currier, N. W.; Yezerets, A.; Olsson, L., Deactivation of Cu-SSZ-13 by SO2 exposure under SCR conditions. *Catal. Sci. Technol.* **2016,** *6* (8), 2565-2579.
39. Auvray, X.; Arvanitidou, M.; Högström, Å.; Jansson, J.; Fouladvand, S.; Olsson, L., Comparative Study of SO2 and SO2/SO3 Poisoning and Regeneration of Cu/BEA and Cu/SSZ-13 for NH3 SCR. *Emission Control Science and Technology* **2021,** *7* (4), 232-246.
40. Mesilov, V.; Dahlin, S.; Bergman, S. L.; Hammershøi, P. S.; Xi, S.; Pettersson, L. J.; Bernasek, S. L., Insights into sulfur poisoning and regeneration of Cu-SSZ-13 catalysts: in situ Cu and S K-edge XAS studies. *Catal. Sci. Technol.* **2021,** *11* (16), 5619-5632.
41. Jangjou, Y.; Do, Q.; Gu, Y. T.; Lim, L. G.; Sun, H.; Wang, D.; Kumar, A.; Li, J. H.; Grabow, L. C.; Epling, W. S., Nature of Cu Active Centers in Cu-SSZ-13 and Their Responses to SO2 Exposure. *ACS Catal.* **2018,** *8* (2), 1325-1337.
42. Wijayanti, K.; Xie, K.; Kumar, A.; Kamasamudram, K.; Olsson, L., Effect of gas compositions on SO2 poisoning over Cu/SSZ-13 used for NH3-SCR. *Applied Catalysis B: Environmental* **2017,** *219*, 142-154.
43. Jangjou, Y.; Wang, D.; Kumar, A.; Li, J.; Epling, W. S., SO2 Poisoning of the NH3-SCR Reaction over Cu-SAPO-34: Effect of Ammonium Sulfate versus Other S-Containing Species. *ACS Catal.* **2016,** *6* (10), 6612-6622.
44. Bergman, U. L.; Dahlin, S.; Mesilov, V. V.; Xiao, Y.; Englund, J.; Xi, S.; Tang, C. H.; Skoglundh, M.; Pettersson, L. J.; Bernasek, S. L., In-situ studies of oxidation/reduction of copper in Cu-CHA SCR catalysts: Comparison of fresh and SO2-poisoned catalysts. *Appl. Catal. B-Environ.* **2020,** *269*, 11.
45. Hammershoi, P. S.; Vennestrom, P. N. R.; Falsig, H.; Jensen, A. D.; Janssens, T. V. W., Importance of the Cu oxidation state for the SO2-poisoning of a Cu-SAPO-34 catalyst in the NH3-SCR reaction. *Appl. Catal. B: Environ* **2018,** *236*, 377-383.

2 Materials and Methods

2.1 Materials

Umicore Denmark, an industrial partner of the project, provided commercial Cu-CHA catalyst samples.

The Cu-CHA catalyst was prepared by impregnating the parent H-CHA zeolite material (Si/Al = 6.7) with the appropriate amount of an aqueous solution of Cu-nitrate. After impregnation, the samples were dried for 2 h at 90 °C, followed by 1 h of calcination at 500 °C in the air to decompose the nitrates.

In this work, the Cu-CHA catalysts with two Cu contents were measured: 0.8 wt% Cu/CHA and 3.2 wt % Cu/CHA. The designations in the text are low-Cu (0.8 wt% Cu/CHA) and high-Cu (3.2 wt% Cu-CHA) catalysts.

2.2 Methods

2.2.1 X-ray absorption spectroscopy

X-ray absorption spectroscopy (XAS) is an effective technique in material science to study materials' electronic and geometric structure at the atomic level. It is based on the interaction of the X-rays with matter. When X-rays pass through a sample, they can be absorbed by the core electrons of specific atoms. The absorption probability depends on the X-rays' energy and the targeted atoms' electronic configuration. [1]

The structural information of the sample is extracted from the absorption coefficient, which corresponds to an exponential drop in the intensity of

the X-ray beam passing through the sample. In the case of the transmission experiment, the absorption coefficient μ is measured by comparing the intensities of the beam before and after the sample of the thickness d (the Beer-Lambert law for absorption):

$$\frac{I}{I_0} = e^{-\mu d} \qquad (2.1)$$

The absorption spectrum is obtained by changing the incident energy, which is possible to perform at synchrotron facilities. With the increase in energy, more photons can go through the sample, μ varies approximately as the inverse third power of the photon energy. This trend is interrupted by step-like increases in absorption as the photon energy matches the ionization potential of an occupied electron state in the atom.[1] This makes the technique element selective, allowing it to distinguish the contributions from different atoms in a complex material.

Usually, a XAS spectrum is divided into two regions: X-ray Absorption Near Edge Structure (XANES) and Extended X-ray Absorption Fine Structure (EXAFS). XANES focuses on the features in the absorption spectra near the absorption edge of an element, which corresponds to the energy level at which an electron is excited from a core level to an unoccupied state. XANES provides information about the oxidation state, coordination geometry, and the electronic and chemical environment of the absorbing atom.

EXAFS analyzes the fine structure oscillations in the X-ray absorption spectrum at energies above the absorption edge. The oscillations in the EXAFS signal are caused by single backscattering events by nearest-

neighbor atoms of the outgoing photoelectron produced through X-ray absorption. These scattered waves interfere with the original photoelectron wave, causing variations in the electron density surrounding the absorbing atom. Consequently, the absorption coefficient μ(E) fluctuates when the photon energy is scanned, revealing valuable information about the local atomic environment, including the neighboring atoms' bond lengths, coordination numbers, and chemical states.

XAS, including XANES and EXAFS, was successfully applied to study the Cu-CHA catalysts for NH_3-SCR. In situ, XAS measurements were used for defining the species forming during the catalytic cycle. [2-12]

2.2.2 X-ray emission spectroscopy

X-ray Emission Spectroscopy (XES) is a powerful experimental technique used to probe the electronic structure of materials. XES measures the emission of photons from the sample due to the deexcitation from a conduction state to a valence state.[13] An emission spectrum is related to the density of occupied states. [14] Experimentally, the incident energy of the X-ray beam is fixed, and the intensity of the emitted radiation is measured for different emitted energies. For this, a set of crystal analyzers and an X-ray detector are used.

XES using synchrotron radiation provides detailed information about the electronic structure, including the energy levels of the valence electrons and their chemical environment. The method proved especially useful for identifying the preferential ligation of the Cu active centers. Valence to core (vtc) XES allowed to distinguish between N and O ligands in Cu

species formed in Cu-CHA. [4] It is also helpful to identify other types of ligands, such as sulfur, [15] which is important for the current work.

2.2.3 X-ray absorption spectroscopy at BM23

The XAS experiments were performed at the BM23 beamline of the ESRF. [16] The storage ring operated in 4-bunch top-up mode at 30 mA maximum current. We chose low-current modes to limit the radiation-induced effects during the prolonged exposures. Measurements were performed in transmission mode at Cu K-edge, using a double-crystal Si(111) monochromator moving in a continuous mode. The acquisition time for one XAS spectrum was 3 min, with an energy range of 8800-10000 eV and an energy step of 0.3 eV. A pair of flat Si mirrors at 2.8 mrad angle was used for harmonic rejection. Ionization chambers were used to detect incident and transmitted photons. I_0 chamber was filled with 1.57 bar N_2, I_1, and I_2 with 0.33 bar Ar, all three topped up with He to the total pressure of 2 bar. The spectra of the Cu reference foil were measured together with the sample and then used for alignment. A scheme of a typical in situ XAS experiment in transmission is presented in Figure 2.1.

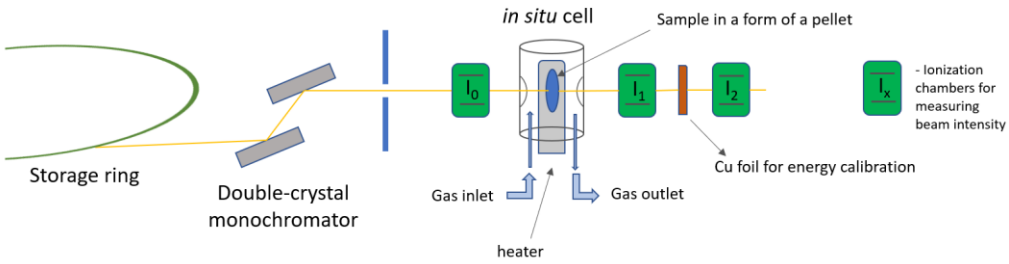

Figure 2.1 Scheme of a typical in situ XAS experiment in transmission at BM23.

The samples were measured as self-supported pellets of a non-diluted catalyst in a Microtomo cell for in situ measurements (Figure 2.2). The pellet was fixed on the plate connected to the resistive heater. The thermocouple was inside the plate to measure the temperature of the sample. The plate was located perpendicular to the X-ray beam going through the sample. The sample could be heated up to 600 °C. The cell was covered with a cap (Figure 2.2) with two Kapton windows for transmission measurements. The configuration of the cell allows to create a gas flow inside the cap. A mobile gas mixing system was used to create the desired gas composition for each experiment.

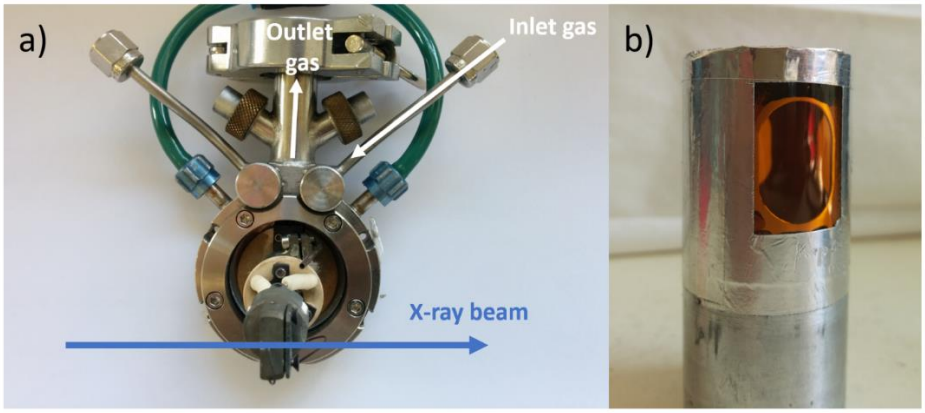

Figure 2.2 Microtomo cell for in situ XAS experiments in transmission mode. a) Top view without the cap; b) The cap with Kapton windows for transmission measurements.

2.2.4 XANES and XES at ID26

The XANES and XES experiments at the S K-edge were performed at the ID26 beamline of the ESRF. The storage ring operated in uniform top-up mode at 200 mA maximum current. The measurements were done using the in-vacuum tender X-ray emission spectrometer based on eleven

Johansson crystal analyzers (TEXS) [17, 18] in a vacuum chamber to minimize X-ray absorption along the sample-analyzers-detector path. The view of the vacuum chamber and the setup of the spectrometer is presented in Figure 2.3. The vacuum level inside the chamber is high with pressure below 1 $\cdot 10^{-5}$ mbar.

The acquisition time for one XANES spectrum was 5 s, an energy range of 2.465-2.51 keV. For the S Kα measurements, incident radiation energy was fixed at 2.65 keV. Scans of emitted radiation energy were performed using the reflection of five identical Si (111) analyzer crystals. S Kα XES data were collected by integrating 1 s per point, each point collected at the fresh spot of the sample.

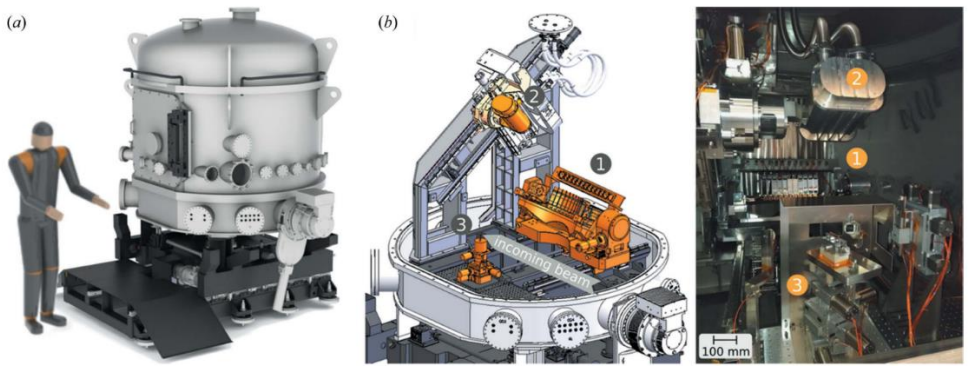

Figure 2.3 Mechanical layout of the spectrometer of the TEXS chamber. Three dimensional (3D) rendering of the external view (a). Internal view (b) as 3D drawing (left, upper parts of the vacuum vessel are removed for clarity) and photograph (right), showing the spectrometer frame with the main sub-assemblies: analyzer table (1), detector (2) and sample environment (3). The incoming beam direction (X) is represented with a grey arrow. Reproduced from Rovezzi et al., 2020[17]

Cu Kβ valence to core (vtc) XES measurements were also carried out at the ID26 beamline of the ESRF. The storage ring operated in uniform top-

up mode at 200 mA maximum current. The measurements were done using a spectrometer with five analyzer crystals in vertical Rowland geometry. Incident radiation energy was fixed at 9050 eV, set by a flat Si (311) double-crystal monochromator. Scans of emitted radiation energy were performed using the (800) reflection of five identical Ge (100) analyzer crystals. The crystals were spherically bent following the Johann scheme to focus the fluorescence radiation on the APD detector. Sample-analyzer distance was ca. 1m. The FWHM of the elastic peak estimated the average energy resolution of ca. 1.7 eV. A He-filled bag was placed between the cell, analyzer crystals, and detector to minimize X-ray absorption along the sample-analyzers-APD path. The incident beam was attenuated by a factor of 10 to decrease radiation damage. Vtc XES data were collected integrating 0.5 s per point, each point collected at the fresh spot of the sample. After each vtc-XES scan, a correction scan was performed with the same integration time, measuring the intensity of Kβ1,3 main line in the same spots on the sample, which was then used to normalize vtc XES data. A background function was subtracted from the XES spectra.

Cu Kβ vtc-XES was measured in the Microtomo cell discussed earlier. The geometry of the cell was different in this case: the pellet was at 45 ° to the incident beam and to the crystal analyzers reflecting the radiation to the detector.

The S edge XANES and XES were measured in a TEXS chamber inside a vacuum catalysis cell adapted for the chamber (Figure 2.4). The cell also has a heater allowing it to heat the sample to 600 °C and a possibility to have a gas flow inside the cell. The pellet is placed parallel to the Kapton

window. The cell is placed at 45 ° to the incident X-ray beam and a set of crystal analyzers reflecting the emitted radiation to the detector.

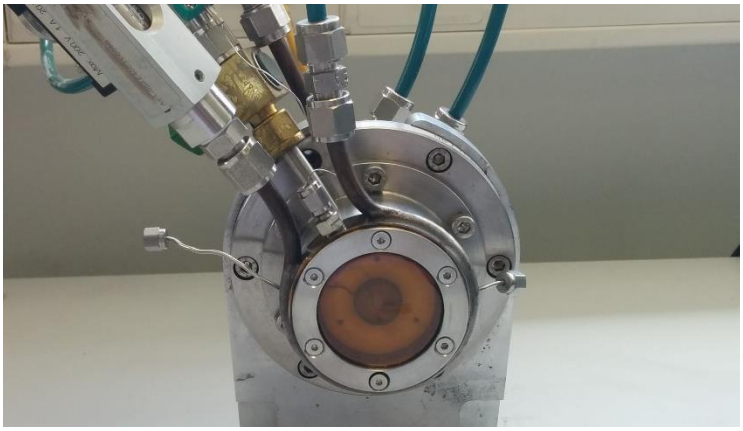

Figure 2.4 Vacuum catalyze cell for measuring in situ XANES and XES inside a vacuum TEXS chamber on ID26 beamline of the ESRF.

2.2.5 XAS data analysis

The first essential step for analyzing XANES and EXAFS spectra is normalization. Normalization regulates the data with respect to sample preparation, absorber concentration, detection etc. The background function must be subtracted from the spectrum for normalization. The background function includes the contribution from the features referred to the absorbing element, such as pre-edge and slowly varying post-edge line, and the constant “external” contribution from the detection or other elements in the sample. There is also a scaling factor dependent on the concentration of the absorbing atom, the sample's thickness, and the detectors' gains. The spectra are normalized by subtracting the background and dividing by the edge step, representing the scaling factor.

After the common normalization procedure, the XANES and EXAFS parts of the spectrum are analyzed separately.

The near-edge features are referred to as the XANES part of the spectrum. The contribution of the multiple scattering of the photoelectron in the near-edge range complicates the theory behind the XANES signal. Therefore, XANES spectra are often analyzed by their interpretation and fingerprinting. The features on the XANES spectra are susceptible to the absorbing atom's oxidation state and local geometry. So, often plotting the normalized spectra together and comparing them with the known reference spectra already makes it possible to draw some conclusions.

Besides fingerprinting, there is progress in the theoretical modeling and quantitative interpretation of the XANES spectra, [19-22] but it remains challenging for many systems. In this work, the theoretical modeling of XANES will not be discussed.

Mixture-resolving techniques or XAS spectral decomposition techniques are another way of extracting valuable information from the XANES spectra. For a complex compound, the resulting XANES spectrum consists of the contributions from the species present in the compound. Linear combination fitting and other mixture resolving techniques discussed further make it possible to find the distinct species present in the compound and estimate their concentrations.

The theory behind the EXAFS analysis is more straightforward compared to XANES since single scattering contributes to the EXAFS signal. The modern analysis of the EXAFS was first presented in 1971 by Sayers, Stern

and Lytle[23] quite quickly developed further. [24, 25] Nowadays, the EXAFS signal is modeled with the EXAFS equation:

$$\chi(\mathrm{k}) = \sum_{j} \frac{\mathrm{N_j} S_0^2}{\mathrm{kR_j^2}} F_j(\mathrm{k}) \mathrm{e}^{-2\mathrm{R}_j/\lambda_j(\mathrm{k})} \mathrm{e}^{-2\mathrm{k}^2\sigma_\mathrm{j}^2} \sin[2\mathrm{kR_j} + \Phi_\mathrm{j}(\mathrm{k})] \quad (2.2)$$

where k is photoelectron wavenumber expressed through energy E:

$$\mathrm{k} = \frac{2\pi}{\lambda} = \sqrt{\frac{2\mathrm{m_e}(\mathrm{E} - \mathrm{E_0})}{\hbar^2}} \quad (2.3)$$

E_0 is the energy of the absorption edge, and m_e is the electron mass. The sum in the EXAFS equation is a sum over shells of atoms of a particular type j and similar distances from the origin of the initial photoelectron. N_j is the coordination number, R_j is the interatomic distance, and σ_j^2 is the mean-square disorder in the distance for the j-th shell. F_j is the photoelectron (back-)scattering amplitude, and $\Phi_j(k)$ is the corresponding (back-)scattering phase for the j-th atomic shell. S_0^2 is an amplitude reduction factor accounting for the relaxation of the absorbing atom due to the presence of the empty core level and multi-electron excitations. $\lambda_j(k)$ is the photoelectron inelastic mean free path, which has a strong dependence upon k, and has values in the range of 1 to 100 Å over the XAFS regime. Both Fj(k) and Φj(k) depend upon the atomic number Z of the scattering atom and have non-linear dependence on k.

Practically, for EXAFS analysis, a slowly varying background function is subtracted from the experimental μ(E) to isolate the fine structure χ(E). Then the energy is converted to the wavenumber to obtain χ(k), which can

be fitted with the EXAFS function. To increase the contribution of the oscillations at high k, $\chi(k)$ is multiplied by k^2 or k^3. Then $(\chi(k)\cdot k^n)$ is subjected to a Fourier transform which gives a function in real space representing the average coordination of the absorbing atom. The EXAFS data analysis based on the EXAFS equation is implemented in the classical packages used for XAS data analysis, such as the Artemis program from Demeter package[26] and Larch[27] code. For building the EXAFS function the structural information of the sample is required. So, EXAFS fit can be used to verify an existing hypothesis on the structure.

2.2.6 XAS spectral decomposition

Sometimes, a XAS spectrum is an average of several contributions from different species present in the sample. In this case, it is possible to decompose XAS spectra and analyze distinct components. Generally, mixture resolving techniques for XAS spectra are based on solving the following matrix equation:

$$X = SC^T + \varepsilon \quad (2.4)$$

Where X is an experimental dataset composed of m energy points and n spectra, S is the matrix of the pure spectral profiles (m energy points, N pure components), C^T is the transpose of the matrix C, containing the concentration profiles of n spectra associated to each pure spectrum of S, $dim(C^T) = (N \times n)$. ε represents the noise matrix ($m \times n$) corresponding to the dataset X. A pictorial representation of the described strategy of spectral decomposition taken from the literature [28] is shown in Figure 2.5.

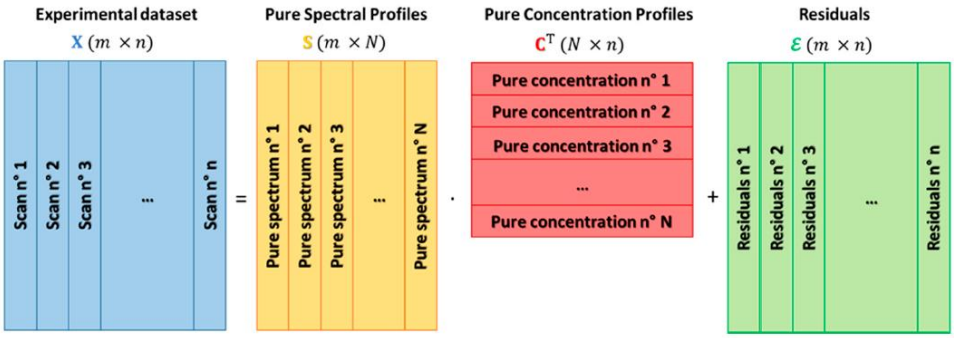

Figure 2.5 Schematic representation of the spectral decomposition regarding an X-ray absorption spectroscopy (XAS) experimental dataset *X*, composed of *n* spectra (scans) and by *m* energy points, in the product of a matrix *S*, containing *N* pure spectral profiles, and matrix *C*, containing their related concentration values. The error in the proposed decomposition is represented by the residual matrix *ε*. It is worth noting that, if the correct number of pure species characterizing the measurements is identified, matrix ε must contains on its columns only the contributions coming from the experimental noise. Reproduced from Martini et al., 2020 [28]

Usually, the first step in the process of the XAS spectral decomposition is to identify the number of pure components *N* in the dataset. For this, several procedures can be used. In the case of a dataset with a simple reaction, sometimes it is possible to locate isosbestic points visually. They indicate the transformation of one species to another during the reaction, thus proving the presence of only two pure components. However, this method is not precise and does not exclude the formation of a small fraction of other species. A more accurate method is Principle component analysis (PCA). PCA is based on the singular value decomposition (SVD) [29] algorithm. In the output of the PCA, there are principal components of the dataset without any chemical and physical sense. A more valuable output is statistical results that estimate how many principal components should be considered in further calculations. There are efficient software

packages available for PCA, such as PyFitit, [30] providing necessary statistics for choosing a suitable number of components.

Once the number of components *N* is identified, there can be two cases: either the pure components and their spectra are known and available, or the pure components are unknown. In the first case, a linear combination fitting is an excellent instrument to resolve the composition of the spectra. It is described in Section 2.2.7. In the case of not known components, additional methods, such as multivariate curve resolution, can be employed (described in Section 2.2.8).

2.2.7 Linear combination fitting

One of the most well-known mixture resolving techniques is a linear combination fitting (LCF) of the spectrum with known reference spectra. When the individual species contributing to the spectrum of interest are known, but the ratio between them is not, LCF is an excellent instrument for data analysis.

The instrumentation for the LCF analysis is included in the most popular software for the XAS data analysis: Athena[26] and Larch[27]. It can also be scripted using available tools in Python or other programming languages to apply to large datasets.

2.2.8 Multivariate Curve Resolution – Alternating Least Squares

Multivariate curve resolution (MCR) is a generic denomination for a family of approaches aimed at realizing the decomposition in Eq. (2.4) from the sole information derived from the original data matrix, including the contributions coming from different chemical species. The Alternating

least squares method for MCR (MCR-ALS) allows to resolve datasets blindly, without knowing the pure components (matrix *S*). [31-34]

The MCR-ALS resolving procedure starts by estimating a set of spectra or concentration profiles, the number of which should correspond to the number of pure components *N* defined earlier. For the analysis of XAS data, one of the most widely used methods is the simple-to-use interactive self-modeling mixture analysis (SIMPLISMA) algorithm. [35] SIMPLISMA identifies a set of spectral or concentration profiles equal to the number of the significant components. Each of them must experience a non-zero contribution from one and only one mixture component. To identify the spectral profiles, a series of vectors containing statistical variables are generated and analyzed for each spectrum in the dataset. These statistical variables express the level of purity associated with each spectrum. Then the pure spectral profiles are identified and iteratively verified by calculating the ratio of the standard deviation (σ) to the mean of the XAS dataset calculated over its rows and ensuring that the profiles are independent (orthogonal) to each other. To ensure the retrieved concentration profiles are physically meaningful, non-negativity constraints are imposed on the spectra and concentration values.

A set of spectra obtained are either pure or just the most different spectra possible. They need to be further refined with the ALS approach. Suppose we initialize the set of pure components. The matrix with concentration profiles *C* can be obtained by using a least squares approach, minimizing the square of residuals between the experimental XAS dataset *X* and the approximated one. After that, a set of constraints should be applied to *C*, such as non-negativity and mass balance condition. Then, a new set of pure

spectral components can be calculated from the corrected matrix of concentration profiles, again minimizing the square residuals between the reconstructed dataset and the experimental one. The corrected version *S* and *C* can be employed to generate *X* and calculate the lack of fit parameter (LOF), defined by the division of the error matrix by *X*. The LOF is calculated for each iteration. If this quantity is lower than a user-defined value or threshold (usually 0.1 %), the convergence is achieved, and the ALS routine is stopped.

The resulting set of spectra is considered a set of pure components corresponding to pure chemical species. However, they require an assessment by the user for physico-chemical and spectroscopic reliability. The availability of complementary information on the investigated systems and chemical processes often plays a crucial role in retrieving a meaningful solution.

In this work, MCR-ALS and SIMPLISMA were used to obtain new spectral components and their concentration profiles. The dataset of XAS spectra was processed using the pyMCR python library.[36]

2.2.9 Temperature programmed reduction by NO

The Temperature programmed reduction by NO (NO-TPR) measurement was used to compare the kinetics of the reaction for the fresh and SO_2-exposed catalysts. Briefly, a slow heating of the catalyst in NO flow gives information about the temperature range of the reaction between the Cu-CHA and NO. This information characterizes the kinetics of the reaction.

NO-TPR was carried out in a flow reactor setup on a specific procedure like the XAS experiment. A sample of 10 mg (based on dry matter) of the fresh catalyst was diluted with 150 mg of Silicon Carbide. The experiments were performed in a quartz U-tube reactor with an inner diameter of 4mm and quartz wool to keep the catalysts as a fixed catalytic bed reactor, and outlet gas were measured with a Gasmet CX4000 FTIR analyzer. The pre-treatment protocols included the formation of $[Cu_2^{II}(NH_3)_4O_2]^{2+}$ complex and the exposure of the $[Cu_2^{II}(NH_3)_4O_2]^{2+}$ complex to SO_2. After pre-treatment protocols, the reactor was purged in N_2 and cooled down to 50 °C. An initial NO concentration was measured by bypassing the reactor. Then, the catalyst was exposed to NO and heated in NO flow up to 550 °C with a ramp rate of 1 °C/min. The position of the negative peak of NO consumption as a function of the temperature depends on the kinetics of the reaction between the catalyst and NO.

2.2.10 Temperature programmed desorption of SO_2

Temperature programmed desorption of SO_2 (SO_2-TPD) allows to obtain the temperature profiles of the concentration of SO_2 desorbing from the catalyst. From the shape of the TPD profiles, it is possible to identify the sulfur species present in the sample. Also, it is possible to estimate the SO_2 uptake and calculate the S/Cu ratio in the sample by integrating the SO_2-TPD profiles.

SO_2-TPD was performed after the same procedures as employed in the XAS experiment on the same samples. The SO_2-TPD was carried out with a simultaneous thermal analyzer (STA 449 F3 Jupiter, NETZSCH), which is coupled with an infrared (FTIR) spectrometer (MKS 2030, MKS Instruments) for evolved gas analysis. The sample was first kept in

nitrogen gas flow 100 ml/min at 50°C for 30 mins and then heated up to 1200°C with 10 K/min. The sample mass is typically 25 mg.

2.2.11 Fourier Transform Infrared spectroscopy

Fourier Transform Infrared (FTIR) spectroscopy is an important technique for studying the active sites of catalysts at the molecular level.[37] Molecular vibrations of compounds give rise to absorption bands throughout most of the infrared region of the spectrum. Since the vibrational energies of molecules have unique fingerprints in the IR spectra, FTIR spectroscopy can provide useful insights into many chemical problems.

In the case of Cu-CHA catalyst in the context of NH_3-SCR cycle, FTIR provided very useful results allowing to identify the bands corresponding to the Brønsted sites,[5, 37] physisorbed NH_3, NH_4^+ formed by NH_3 protonation by the Brønsted sites, [38-40] and the formation of particular Cu complexes. [2, 3, 5, 8, 37] In this work, the FTIR spectroscopy was used mostly for monitoring the absorption and desorption or consumption of NH_3 and NH_4^+ during specific steps related to NH_3-SCRreaction and SO_2 poisoning. This information complements the insights obtained from XAS and other techniques.

FTIR experiments were performed at the Chemistry department of the University of Turin using a Bruker FTIR spectrometer and an operando sandwich cell (IR rector-cell) developed for investigating chemical reactions with FTIR. [41-43] The general and detailed views of the IR reactor cell are presented in Figure 2.6. The experimental procedures reproduce the conditions of the XAS experiments and study the monitored reactions from another perspective. The construction of the cell allows to heat the

sample to 400 °C and to use gas compositions as in the XAS in situ experiments.

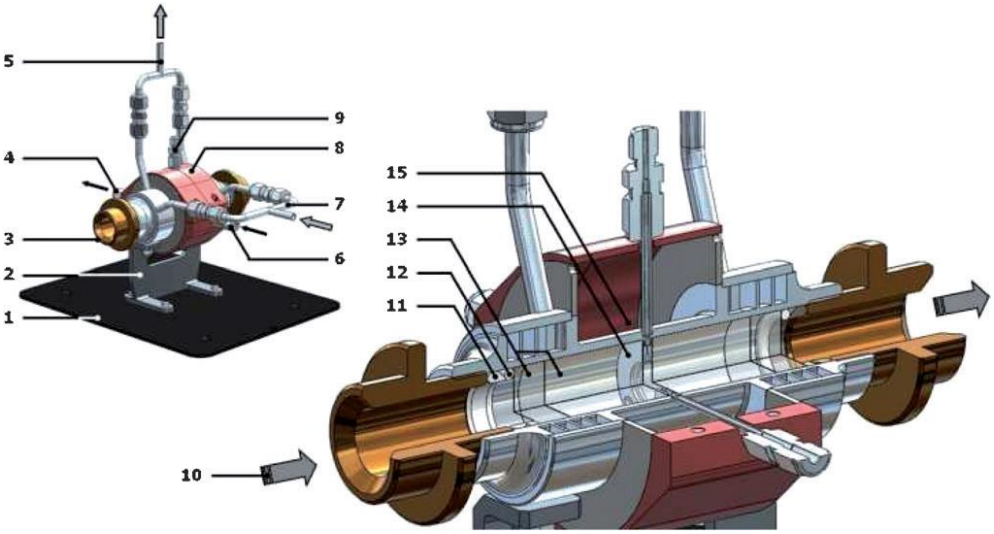

Figure 2.6 General and detailed views of the "sandwich" reactor-cell. 1= Spectrometer base-plate, 2=IR cell support, 3=adjusting nut for air tightness, 4=gas outlet, 5=air cooling outlet, 6=gas inlet, 7=air cooling inlet, 8=external shell, 9=thermocouple location, 10=IR beam, 11= stainless steel ring, 12=Kalrez O-ring, 13=KBr windows, 14=wafer holder, 15=oven location. Reproduced from Lesage et al., 2003 [42]

2.3 New methods

2.3.1 X-ray adsorbate quantification (XAQ)

X-ray adsorbate quantification (XAQ) is a new method developed by our team during the experiments at BM23 in the scope of this project. It proved to be extremely useful for quantification of adsorbates during *in situ* XAS experiments, complementing the mass-spectrometry data. [44]

In Section 2.2.5, a normalization procedure for XAS spectra was described. As already discussed, it aims to remove the effects associated

with the experimental setup and the sample preparation to compare the data from different datasets and samples effectively. However, one of the factors we remove by normalizing a transmission XAS spectrum is the total absorption of the sample. For a quantitative and qualitative analysis of XANES and EXAFS, the total absorption of the sample is only a regulator of the data quality. However, the total absorption may change during an in situ XAS experiment involving the adsorption and desorption of molecules on and from the sample. This change in the total absorption is valuable information that has been ignored and removed from the data before.

In Figure 2.7, (a) and (b) panels explain the abovementioned concept. Panel (a) shows normalized XAS data as we are used to see them in publications. Panel (b) shows raw data as they are usually seen during beamline experiments. In panel (b), there is a clear shift of all the spectra, indicating the change in the total absorption of the sample. The reported spectra were obtained while heating the hydrated Cu-CHA zeolite in O_2. Then the difference in the total absorption is explained by dehydration of the sample, that is H_2O desorption.

Panel (c) shows the XAQ signal during heating and temperature profile in time. Presented this way XAQ technique seems similar to Thermogravimetric analysis (TGA), monitoring the change in mass of the sample during thermal treatment. Indeed, the methods have the same idea behind them. An advantage of XAQ is that it can be monitored directly during transmission XAS experiments and does not require additional preparation and instrumentation. Even old datasets containing in situ XAS

spectra measured in transmission can be analyzed to extract the XAQ signal.

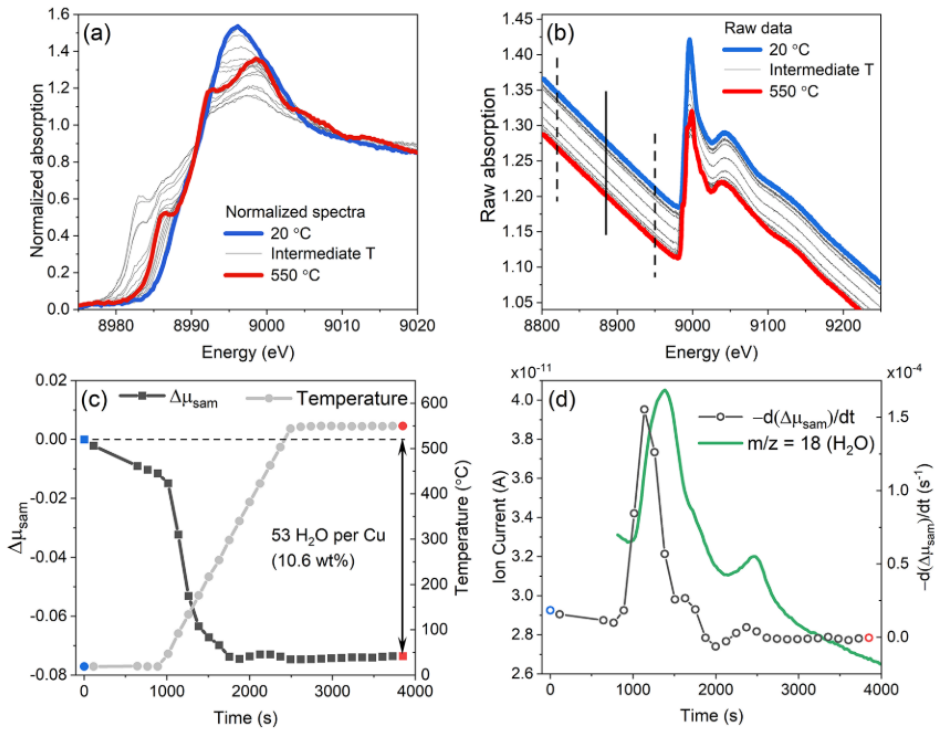

Figure 2.7 (a) Normalized Cu K-edge XANES spectra collected during heating of Cu-CHA zeolite from RT to 550 °C in 10 % O2/He flow. (b) Same data without normalization. Dashed lines indicate the XAQ fitting region and solid line shows its center where the total absorption is evaluated. (c) XAQ signal during heating (left) and temperature profile (right). (d) Time derivative of the XAQ signal (left axis) and water mass spectrometer signal collected simultaneously with the XAS measurements. Reproduced from Lomachenko et al., 2022[44]

Panel (d) in In Figure 2.7 shows a time derivative of the XAQ signal and water mass spectrometer signal collected simultaneously with the XAS measurements. The signals are very similar, which shows the reliability of

XAQ. This work shows more examples of XAQ results compared with other methods that show good reproducibility.

Experimentally, some points must be considered for obtaining a good and reliable XAQ. First, the experimentalists need to know the composition of species adsorbing on or desorbing from the sample. If there are parallel processes involving different species, distinguishing their XAQ signals will be a very challenging task. The same limitation applies to TGA as well. Second, the spot of the sample under the X-ray beam should always be the same. If the beam moves on the sample (or the sample moves under the beam), and the sample is not homogeneous, the total absorption of the sample will change because a different part of the sample with different absorption is probed. Third, the XAQ signal takes into account the change in total absorption of everything between the two ionization chambers used for the detection. This is important if the sample is exposed to a gas and the cell has some dead volume. In this case, the change in the total absorption is expressed in the following way:

$$\Delta\mu_{tot} = \Delta(ln\frac{I_0}{I_1}) = \Delta\mu_{sam} + \Delta\mu_{gas} \quad (2.5)$$

where μ_{sam} and μ_{gas} are the total absorption of the sample and the gas inside the experimental cell, respectively; I_0 and I_1 are the counts of the ionization chambers measuring the intensity of the incident and transmitted radiation, respectively.

Practically, the $\Delta\mu_{gas}$ can be measured separately in an empty in situ cell and subtracted from the $\Delta\mu_{tot}$ measured during the experimental procedure. So, carefully considered, it does not cause errors in the XAQ calculations.

When $\Delta\mu_{sam}$ is correctly identified, it can be recalculated to the molar surface density of the adsorbed or desorbed species Θ_{ads} (that is, the number of moles of the adsorbate per unit area of the sample surface exposed to the X-ray beam) by the following expression:

$$\Theta_{ads} = \Delta\mu_{sam}\left(2r_e\lambda N_A\sum_j Nj\, f"_j\right)^{-1} \quad (2.6)$$

where r_e is the electron radius, λ is the X-ray wavelength, N_A is the Avogadro number, N_j and f_j'' are the number of atoms and imaginary part of the atomic scattering factor of j_{th} atomic species constituting the molecule of adsorbates. This calculation can be performed using existing codes to optimize the mass or thickness of the samples for XAS measurements, such as XAFSmass. [45]

Another important point to note is that Eq. (2.6) is expressed as (2.7) in case if orientation of the pellet to the X-ray beam is not 90°:

$$\Theta_{ads} = \Delta\mu_{sam}\left(\frac{2r_e\lambda N_A}{sin\theta}\sum_j Nj\, f"_j\right)^{-1} \quad (2.7)$$

Where θ – is X-ray incidence angle (Figure 2.8). In most cases $sin\theta = 1$, since for the XAS transmission mode θ is usually equal to 90°. However, if the measurements are conducted in the fluorescence mode, where the orientation of the sample is usually 45°, the X-ray incidence angle has to be taken into account.

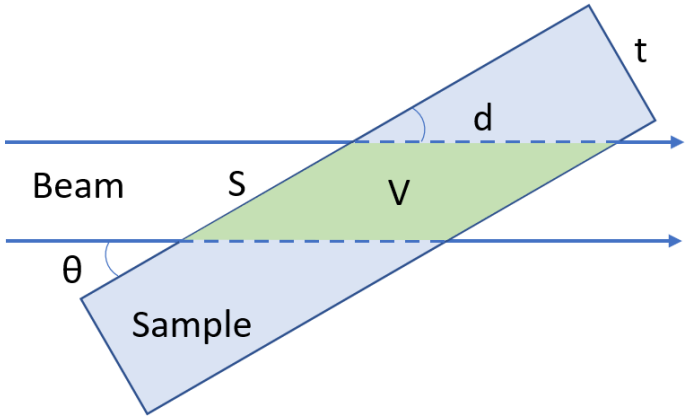

Figure 2.8 Cut of the sample interacting with the X-ray beam. S is the area of the sample surface interacting with the beam, V is the interaction volume, d is the path of the beam through the sample, t – sample thickness, θ – X-ray incidence angle. Reproduced from Lomachenko et al., 2022 [44]

In this work, XAQ was used to calculate the sulfur uptake by the catalyst during its exposure to SO_2. The XAQ data were obtained by monitoring the change of the total absorption coefficient before the Cu K edge (at 8885 eV, averaging the region of 8820-8950 eV) during the interaction with SO_2. The change in the absorption coefficient was attributed to the adsorption of SO_2. The corresponding number of moles of SO_2 per unit area of the pellet was calculated by XAFS mass code[45] and, knowing the parameters of the sample pellet (mass, surface density, and Cu content), converted into Cu/S ratio.

2.4 References

1. Philip, W., *An Introduction to Synchrotron Radiation: Techniques and Applications*. John Wiley & Sons, Ltd: 2011.
2. Borfecchia, E.; Beato, P.; Svelle, S.; Olsbye, U.; Lamberti, C.; Bordiga, S., Cu-CHA - a model system for applied selective redox catalysis. *Chem. Soc. Rev.* **2018,** *47* (22), 8097-8133.

3. Borfecchia, E.; Lomachenko, K. A.; Giordanino, F.; Falsig, H.; Beato, P.; Soldatov, A. V.; Bordiga, S.; Lamberti, C., Revisiting the nature of Cu-sites in activated Cu-SSZ-13 catalyst for SCR reaction. *Chem. Sci.* **2015,** *6*, 548-563.
4. Lomachenko, K. A.; Borfecchia, E.; Negri, C.; Berlier, G.; Lamberti, C.; Beato, P.; Falsig, H.; Bordiga, S., The Cu-CHA deNO_x catalyst in action: temperature-dependent NH_3-assisted selective catalytic reduction monitored by operando XAS and XES. *J. Am. Chem. Soc.* **2016,** *138* (37), 12025−12028.
5. Negri, C.; Borfecchia, E.; Cutini, M.; Lomachenko, K. A.; Janssens, T. V. W.; Berlier, G.; Bordiga, S., Evidence of Mixed-Ligand Complexes in Cu−CHA by Reaction of Cu Nitrates with NO/NH3 at Low Temperature. *ChemCatChem* **2019,** *11* (16), 3828-3838.
6. Negri, C.; Borfecchia, E.; Martini, A.; Deplano, G.; Lomachenko, K. A.; Janssens, T. V. W.; Berlier, G.; Bordiga, S., In situ X-ray absorption study of Cu species in Cu-CHA catalysts for NH3-SCR during temperature-programmed reduction in NO/NH3. *Research on Chemical Intermediates* **2021,** *47* (1), 357-375.
7. Negri, C.; Martini, A.; Deplano, G.; Lomachenko, K. A.; Janssens, T. V. W.; Borfecchia, E.; Berlier, G.; Bordiga, S., Investigating the role of Cu-oxo species in Cu-nitrate formation over Cu-CHA catalysts. *Phys Chem Chem Phys* **2021,** *23* (34), 18322-18337.
8. Negri, C.; Selleri, T.; Borfecchia, E.; Martini, A.; Lomachenko, K. A.; Janssens, T. V. W.; Cutini, M.; Bordiga, S.; Berlier, G., Structure and Reactivity of Oxygen-Bridged Diamino Dicopper(II) Complexes in Cu-Ion-Exchanged Chabazite Catalyst for NH3-Mediated Selective Catalytic Reduction. *J. Am. Chem. Soc.* **2020,** *142* (37), 15884-15896.
9. Vitaly Mesilov, S. D., Susanna L. Bergman, Shibo Xi, Joonsoo Han, Louise Olsson, Lars J. Pettersson, Steven L. Bernasek, Regeneration of sulfur-poisoned Cu-SSZ-13 catalysts: Copper speciation and catalytic performance evaluation. *Applied Catalysis B: Environmental* **2021,** *299*.
10. Borfecchia, E.; Negri, C.; Lomachenko, K. A.; Lamberti, C.; Janssens, T. V. W.; Berlier, G., Temperature-dependent dynamics of NH3-derived Cu species in the Cu-CHA SCR catalyst. *React Chem Eng* **2019,** *4* (6), 1067-1080.
11. Martini, A.; Borfecchia, E.; Lomachenko, K. A.; Pankin, I. A.; Negri, C.; Berlier, G.; Beato, P.; Falsig, H.; Bordiga, S.; Lamberti, C., Composition-driven Cu-speciation and reducibility in Cu-CHA zeolite catalysts: a multivariate XAS/FTIR approach to complexity. *Chem Sci* **2017,** *8* (10), 6836-6851.
12. Mesilov, V.; Dahlin, S.; Bergman, S. L.; Hammershøi, P. S.; Xi, S.; Pettersson, L. J.; Bernasek, S. L., Insights into sulfur poisoning and regeneration of Cu-SSZ-13 catalysts: in situ Cu and S K-edge XAS studies. *Catal. Sci. Technol.* **2021,** *11* (16), 5619-5632.
13. Jeroen A. van Bokhoven, C. L., *X-Ray Absorption and X-Ray Emission Spectroscopy: Theory and Applications*. John Wiley & Sons: 2016.

14. Bergmann, U.; Glatzel, P., X-ray emission spectroscopy. *Photosynth Res* **2009,** *102* (2-3), 255-66.
15. Vegelius, J. R.; Kvashnina, K. O.; Klintenberg, M.; Soroka, I. L.; Butorin, S. M., Cu K beta(2,5) X-ray emission spectroscopy as a tool for characterization of monovalent copper compounds. *Journal of Analytical Atomic Spectrometry* **2012,** *27* (11), 1882-1888.
16. Mathon, O.; Beteva, A.; Borrel, J.; Bugnazet, D.; Gatla, S.; Hino, R.; Kantor, I.; Mairs, T.; Munoz, M.; Pasternak, S.; Perrin, F.; Pascarelli, S., The time-resolved and extreme conditions XAS (TEXAS) facility at the European Synchrotron Radiation Facility: the general-purpose EXAFS bending-magnet beamline BM23. *J. Synchrot. Radiat.* **2015,** *22* (6), 1548-1554.
17. Rovezzi, M.; Harris, A.; Detlefs, B.; Bohdan, T.; Svyazhin, A.; Santambrogio, A.; Degler, D.; Baran, R.; Reynier, B.; Crespo, P. N.; Heyman, C.; Van Der Kleij, H. P.; Van Vaerenbergh, P.; Marion, P.; Vitoux, H.; Lapras, C.; Verbeni, R.; Kocsis, M. M.; Manceau, A.; Glatzel, P., TEXS: in-vacuum tender X-ray emission spectrometer with 11 Johansson crystal analyzers. *J. Synchrot. Radiat.* **2020,** *27*, 813-826.
18. Glatzel, P.; Harris, A.; Marion, P.; Sikora, M.; Weng, T. C.; Guilloud, C.; Lafuerza, S.; Rovezzi, M.; Detlefs, B.; Ducotte, L., The five-analyzer point-to-point scanning crystal spectrometer at ESRF ID26. *J. Synchrot. Radiat.* **2021,** *28*, 362-371.
19. Rehr, J. J.; Albers, R. C., Theoretical approaches to x-ray absorption fine structure. *Reviews of Modern Physics* **2000,** *72* (3), 621-654.
20. Rehr, J. J.; Ankudinov, A. L., Progress in the theory and interpretation of XANES. *Coordination Chemistry Reviews* **2005,** *249* (1), 131-140.
21. Guda, S. A.; Guda, A. A.; Soldatov, M. A.; Lomachenko, K. A.; Bugaev, A. L.; Lamberti, C.; Gawelda, W.; Bressler, C.; Smolentsev, G.; Soldatov, A. V.; Joly, Y., Optimized Finite Difference Method for the Full-Potential XANES Simulations: Application to Molecular Adsorption Geometries in MOFs and Metal-Ligand Intersystem Crossing Transients. *J Chem Theory Comput* **2015,** *11* (9), 4512-21.
22. Bunau, O.; Joly, Y., Self-consistent aspects of x-ray absorption calculations. *J Phys Condens Matter* **2009,** *21* (34), 345501.
23. Sayers, D. E.; Stern, E. A.; Lytle, F. W., New Technique for Investigating Noncrystalline Structures: Fourier Analysis of the Extended X-Ray—Absorption Fine Structure. *Physical Review Letters* **1971,** *27* (18), 1204-1207.
24. Teo, B.-K.; Lee, P. A., Ab initio calculations of amplitude and phase functions for extended x-ray absorption fine structure spectroscopy. *J. Am. Chem. Soc.* **1979,** *101* (11), 2815-2832.
25. Lee, P. A.; Citrin, P. H.; Eisenberger, P.; Kincaid, B. M., Extended x-ray absorption fine structure---its strengths and limitations as a structural tool. *Reviews of Modern Physics* **1981,** *53* (4), 769-806.

26. Ravel, B.; Newville, M., ATHENA and ARTEMIS Interactive Graphical Data Analysisusing IFEFFIT. *Physica Scripta* **2005,** *T115*, 1007–1010.
27. Newville, M. In *Larch: An Analysis Package for XAFS and Related Spectroscopies*, 15th International Conference on X-Ray Absorption Fine Structure (XAFS), Beijing, PEOPLES R CHINA, Jul 22-28; Beijing, PEOPLES R CHINA, 2012.
28. Martini, A.; Borfecchia, E., Spectral Decomposition of X-ray Absorption Spectroscopy Datasets: Methods and Applications. *Crystals* **2020,** *10* (8), 46.
29. Demmel, J.; Gu, M.; Eisenstat, S.; Slapničar, I.; Veselić, K.; Drmač, Z., Computing the singular value decomposition with high relative accuracy. *Linear Algebra and its Applications* **1999,** *299* (1), 21-80.
30. Martini, A.; Guda, S. A.; Guda, A. A.; Smolentsev, G.; Algasov, A.; Usoltsev, O.; Soldatov, M. A.; Bugaev, A.; Rusalev, Y.; Lamberti, C.; Soldatov, A. V., PyFitit: The software for quantitative analysis of XANES spectra using machine-learning algorithms. *Comput Phys Commun* **2020,** *250*.
31. Conti, P.; Zamponi, S.; Giorgetti, M.; Berrettoni, M.; Smyrl, W. H., Multivariate Curve Resolution Analysis for Interpretation of Dynamic Cu K-Edge X-ray Absorption Spectroscopy Spectra for a Cu Doped V2O5 Lithium Battery. *Analytical Chemistry* **2010,** *82* (9), 3629-3635.
32. de Juan, A.; Tauler, R., Chemometrics applied to unravel multicomponent processes and mixtures: Revisiting latest trends in multivariate resolution. *Analytica Chimica Acta* **2003,** *500* (1), 195-210.
33. de Juan, A.; Tauler, R., Multivariate Curve Resolution (MCR) from 2000: Progress in Concepts and Applications. *Critical Reviews in Analytical Chemistry* **2006,** *36* (3-4), 163-176.
34. Tauler, R., Multivariate curve resolution applied to second order data. *Chemometrics and Intelligent Laboratory Systems* **1995,** *30* (1), 133-146.
35. Windig, W.; Guilment, J., Interactive self-modeling mixture analysis. *Analytical Chemistry* **1991,** *63* (14), 1425-1432.
36. Camp, C. H., Jr., pyMCR: A Python Library for MultivariateCurve Resolution Analysis with Alternating Regression (MCR-AR). *J Res Natl Inst Stand Technol* **2019,** *124*, 1-10.
37. Vimont, A.; Thibault-Starzyk, F.; Daturi, M., Analysing and understanding the active site by IR spectroscopy. *Chem Soc Rev* **2010,** *39* (12), 4928-50.
38. Janssens, T. V. W.; Falsig, H.; Lundegaard, L. F.; Vennestrom, P. N. R.; Rasmussen, S. B.; Moses, P. G.; Giordanino, F.; Borfecchia, E.; Lomachenko, K. A.; Lamberti, C.; Bordiga, S.; Godiksen, A.; Mossin, S.; Beato, P., A Consistent Reaction Scheme for the Selective Catalytic Reduction of Nitrogen Oxides with Ammonia. *ACS Catal.* **2015,** *5* (5), 2832-2845.
39. Giordanino, F.; Borfecchia, E.; Lomachenko, K. A.; Lazzarini, A.; Agostini, G.; Gallo, E.; Soldatov, A. V.; Beato, P.; Bordiga, S.; Lamberti, C.,

Interaction of NH3 with Cu-SSZ-13 Catalyst: A Complementary FTIR, XANES, and XES Study. *J. Phys. Chem. Lett.* **2014,** *5* (9), 1552-1559.
40. Colombo, M.; Nova, I.; Tronconi, E., Detailed kinetic modeling of the NH3–NO/NO2 SCR reactions over a commercial Cu-zeolite catalyst for Diesel exhausts after treatment. *Catal. Today* **2012,** *197* (1), 243-255.
41. Thomas, S.; Marie, O.; Bazin, P.; Lietti, L.; Visconti, C. G.; Corbetta, M.; Manenti, F.; Daturi, M., Modelling a reactor cell for operando IR studies: From qualitative to fully quantitative kinetic investigations. *Catal. Today* **2017,** *283*, 176-184.
42. Wuttke, S.; Bazin, P.; Vimont, A.; Serre, C.; Seo, Y. K.; Hwang, Y. K.; Chang, J. S.; Ferey, G.; Daturi, M., Discovering the active sites for C3 separation in MIL-100(Fe) by using operando IR spectroscopy. *Chemistry* **2012,** *18* (38), 11959-67.
43. Lesage, T.; Verrier, C.; Bazin, P.; Saussey, J.; Daturi, M., Studying the NOx-trap mechanism over a Pt-Rh/Ba/Al2O3catalyst by operando FT-IR spectroscopy. *Phys. Chem. Chem. Phys.* **2003,** *5* (20), 4435-4440.
44. Lomachenko, K.; Molokova, A.; Atzori, C.; Mathon, O., Quantification of adsorbates by X-ray absorption spectroscopy: getting TGA-like information for free. *J. Phys. Chem. C* **2021,** *126* (11), 5175–5179.
45. Klementiev, K.; Chernikov, R., XAFSmass: a program for calculating the optimal mass of XAFS samples. *Journal of Physics: Conference Series* **2016,** *712*, 012008.

3 SO_2 Poisoning of Cu-CHA deNO_x Catalyst: The Most Vulnerable Cu Species Identified by X-ray Absorption Spectroscopy

The results are published in JACS Au in 2022:

SO_2 Poisoning of Cu-CHA deNO_x Catalyst: The Most Vulnerable Cu Species Identified by X-ray Absorption Spectroscopy. *Anastasia Yu. Molokova, Elisa Borfecchia, Andrea Martini, Ilia A. Pankin, Cesare Atzori, Olivier Mathon, Silvia Bordiga, Fei Wen, Peter N. R. Vennestrøm, Gloria Berlier, Ton V. W. Janssens, and Kirill A. Lomachenko. JACS Au* ***2022*** *2 (4), 787-792. DOI: 10.1021/jacsau.2c00053*

3.1 Samples

This Chapter investigates Cu-CHA samples with 0.8 wt% Cu/CHA and 3.2 wt% Cu/CHA. The designation of the samples in this and the following Chapters: low-Cu (0.8 wt% Cu/CHA) and high-Cu (3.2 wt% Cu-CHA).

The results for high-Cu catalyst were published in *JACS Au*, the results for low-Cu catalyst were previously unpublished.

3.2 Experimental methods

In this chapter, we used in situ XAS (XANES and EXAFS) for monitoring the oxidation state of the Cu during the experiment; in situ XAQ for estimating the SO_2 uptake by the catalyst during the experiment; SO_2-TPD on the saturated sample for estimating the SO_2 uptake by the catalyst after the experiment; XES for identification of the ligands coordinated to Cu;

EXAFS fitting, Linear Combination fitting (LCF) and wavelet analysis for identification of the Cu intermediates forming during the experiment.

3.3 Experimental protocol

This Chapter investigates the individual reactivity of different Cu species forming in the NH_3-SCR cycle towards SO_2.

The protocol for preparing Cu species in Cu-CHA where Cu is in different oxidation states and coordination is well known from previous works. [1-3] First step is to bring the Cu-CHA catalyst into a well-defined state by heating it to 550 °C. This state can be followed by various pre-treatment protocols ensuring the formation of one of the Cu intermediates. The protocols are described in Table 3.1 and shown in Figures 3.1-3.6.

The first three procedures aim to obtain a Cu^I state. In Procedure 1, the oxidized state is followed by a reduction protocol at 400 °C in H_2. After cooling to 200 °C in He, the resulting state is Cu^I attached to the framework (fw-Cu^I). [1] In Procedure 2, the reduction is performed by exposure to a mixture of NO and NH_3 at 200 °C, forming the mobile $[Cu^I(NH_3)_2]^+$ complexes. [1] In Procedure 3, this state is followed by heating to 550 °C in He, which results in the release of NH_3 ligands and formation of fw-Cu^I again.

In Procedures 4-6, the goal is to obtain Cu^{II} intermediates. Procedure 4 includes only cooling down from 550°C to 200 °C in O_2. This state is proposed to be Cu^{II} bound to the framework (fw-Cu^{II}). [2] Procedure 5 aims to form the peroxo $[Cu_2^{II}(NH_3)_4O_2]^{2+}$ complexes. To form them, the mobile $[Cu^I(NH_3)_2]^+$ complexes obtained in Procedure 2 have to be exposed to O_2 at 200 °C. [3] Finally, in Procedure 6, fw-Cu^{II} species were exposed to NH_3

at 200 °C. As we show in this work, this procedure results in a mixture of Cu^{I} and Cu^{II} intermediates. [4] This state was assigned as Cu^{II}+NH_3 in the text, figures and tables.

Table 3.1 Pre-treatment procedures and resulting Cu species.

Procedure	**Conditions**	**Dominant Cu state**	**Designation in the text and figures**	**Ref.**
1	1 % H_2 at 400 °C; cooling to 200 °C in He	fw-Cu^{I}	fw-Cu^{I}	[1]
2	500 ppm NO + 600 ppm NH_3 at 200 °C	mobile $[Cu^{I}(NH_3)_2]^{+}$	$[Cu^{I}(NH_3)_2]^{+}$	[1]
3	500 ppm NO + 600 ppm NH_3 at 200 °C; heating to 550 °C in He; cooling back to 200 °C in He	fw-Cu^{I} (after thermal treatment of $[Cu^{I}(NH_3)_2]^{+}$)	$[Cu^{I}(NH_3)_2]^{+}$ + T	[1]
4	10 % O_2 at 200 °C	fw-Cu^{II}	fw-Cu^{II}	[2]
5	500 ppm NO + 600 ppm NH_3 at 200 °C; He purge; 10 % O_2 at 200 °C	mobile $[Cu^{II}_2(NH_3)_4O_2]^{2+}$ dimer	$[Cu^{II}_2(NH_3)_4O_2]^{2+}$	[3]
6	600 ppm NH_3 at 200 °C	mixed*	Cu^{II} + NH_3	[4]

* The mixed Cu^{I}/Cu^{II} composition of the species is discussed further in the chapter.

After the described pre-treatment protocols, the obtained Cu intermediates were exposed to 400 ppm SO_2 at 200 °C for 3 hours

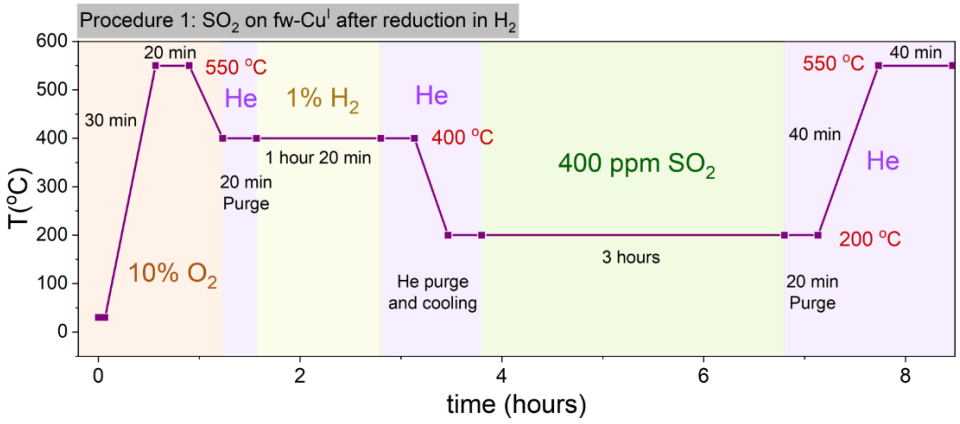

Figure 3.1 Scheme of the followed experimental protocol comprising the pre-treatment Procedure 1 leading to the formation of fw-Cu^I species prior to exposure to SO_2. Reproduced from Molokova et al., 2022. [4]

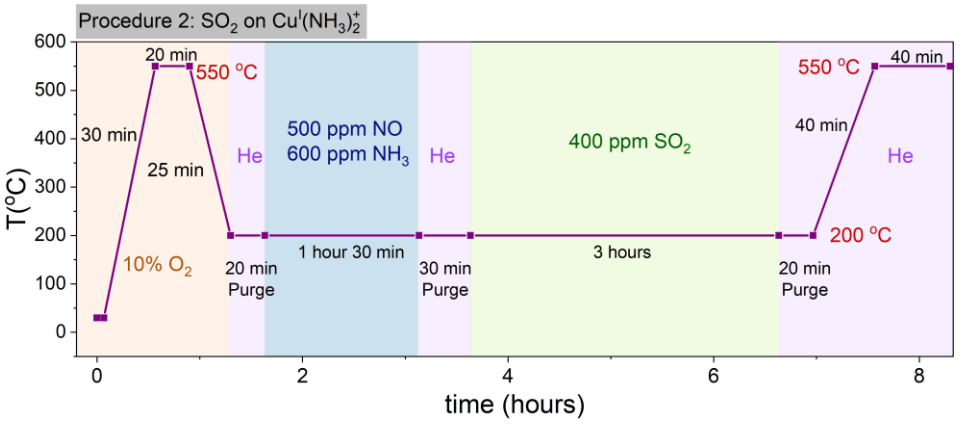

Figure 3.2 Scheme of the experimental protocol comprising the pre-treatment Procedure 2, leading to the formation of mobile $[Cu^I(NH_3)_2]^+$ complexes prior to exposure to SO_2. Reproduced from Molokova et al., 2022. [4]

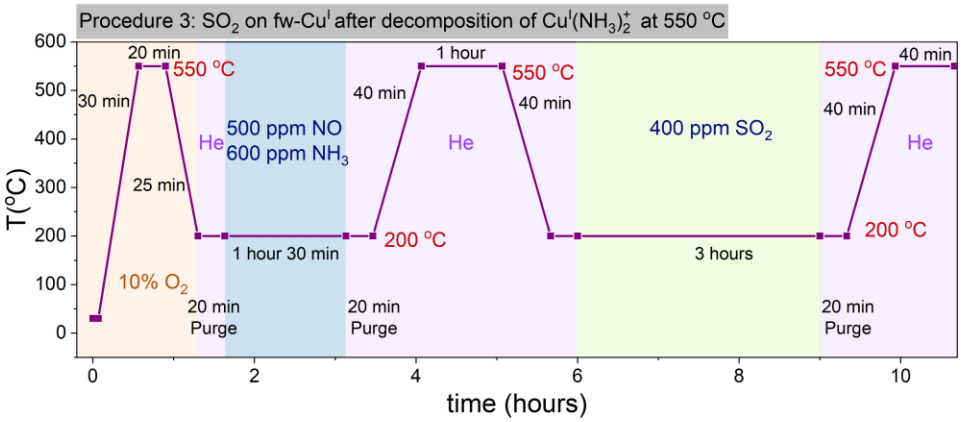

Figure 3.3 Scheme of the experimental protocol comprising the pre-treatment Procedure 3 leading to the formation of fw-Cu^{I} species prior to exposure to SO_2. Reproduced from Molokova et al., 2022. [4]

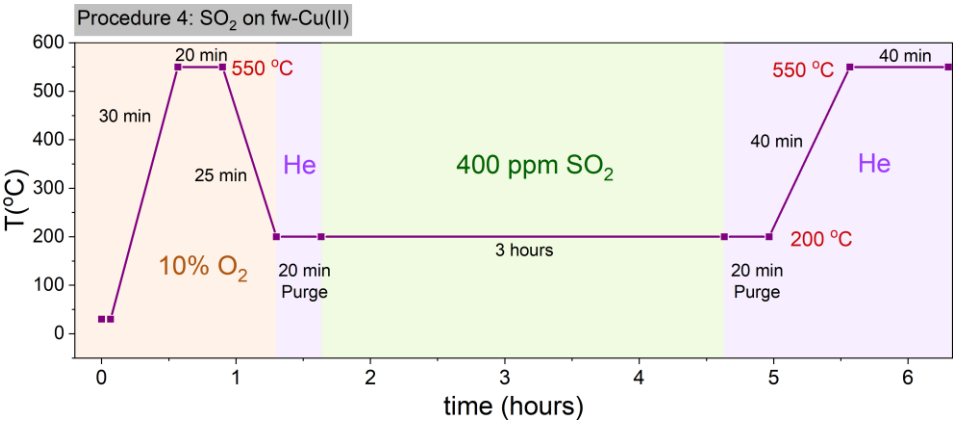

Figure 3.4 Scheme of the experimental protocol comprising the pre-treatment Procedure 4 leading to the formation of fw-Cu^{II} species prior to exposure to SO_2. Reproduced from Molokova et al., 2022. [4]

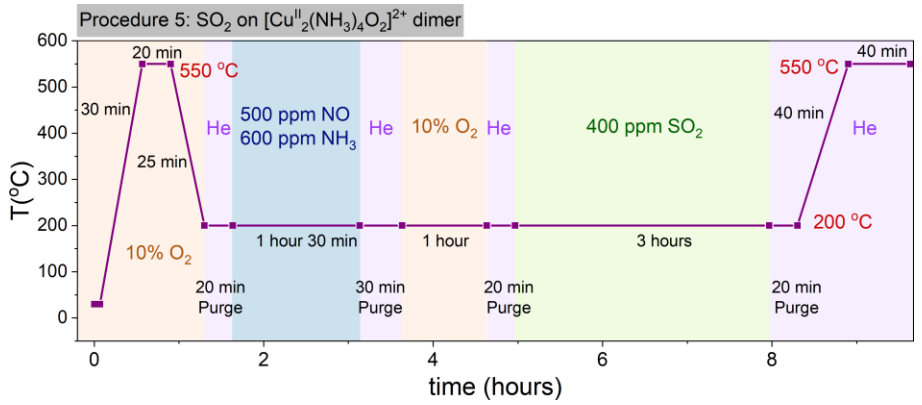

Figure 3.5 Scheme of the experimental protocol comprising the pre-treatment Procedure 5 leading to the formation of mobile $[Cu^{II}_2(NH_3)_4O_2]^{2+}$ dimers prior to exposure to SO_2. Reproduced from Molokova et al., 2022. [4]

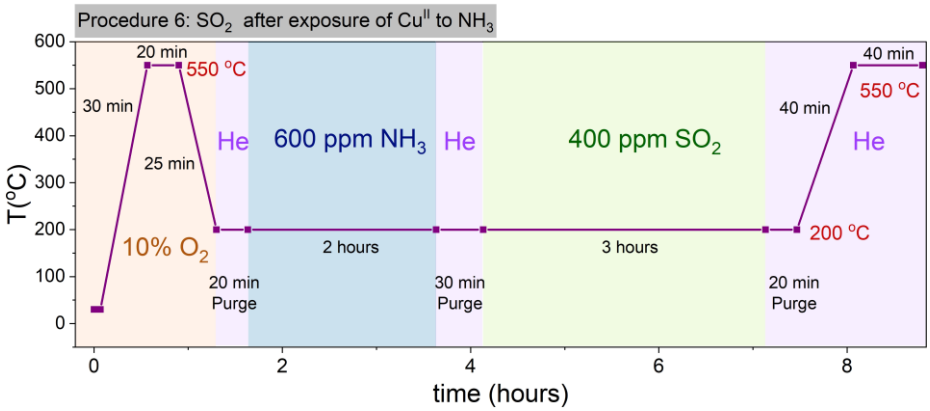

Figure 3.6 Scheme of the experimental protocol comprising the pre-treatment Procedure 6 leading to the formation of mixture of NH_3-coordinated Cu^I/Cu^{II} species prior to exposure to SO_2. Reproduced from Molokova et al., 2022. [4]

3.4 XANES and EXAFS results

We followed the exposure of Cu intermediates to 400 ppm SO_2/He flow by measuring Cu K-edge XAS (XANES and EXAFS) *in situ*. Figure 3.7

and Figure 3.8 show the evolution of XANES and EXAFS spectra during the exposure to SO_2 of the Cu-CHA catalyst with 0.8 wt% Cu/CHA and 3.2 wt% Cu/CHA.

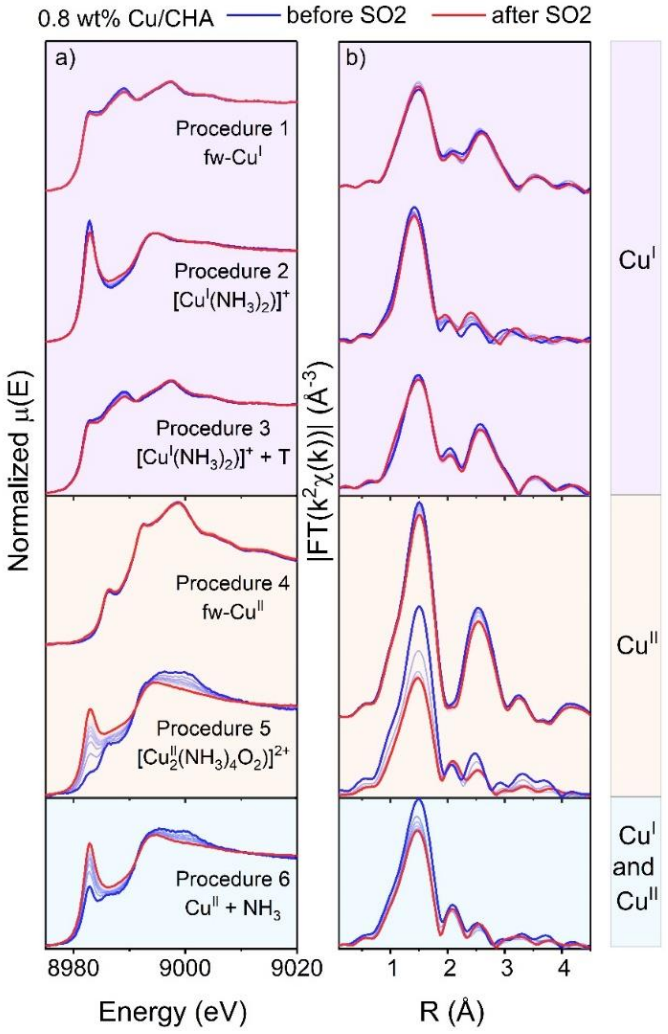

Figure 3.7. Cu K-edge XANES (a) and FT-EXAFS spectra (b) collected *in situ* during the exposure of Cu species obtained in Procedures 1-6 to SO_2 at 200 °C for the low Cu/CHA catalyst.

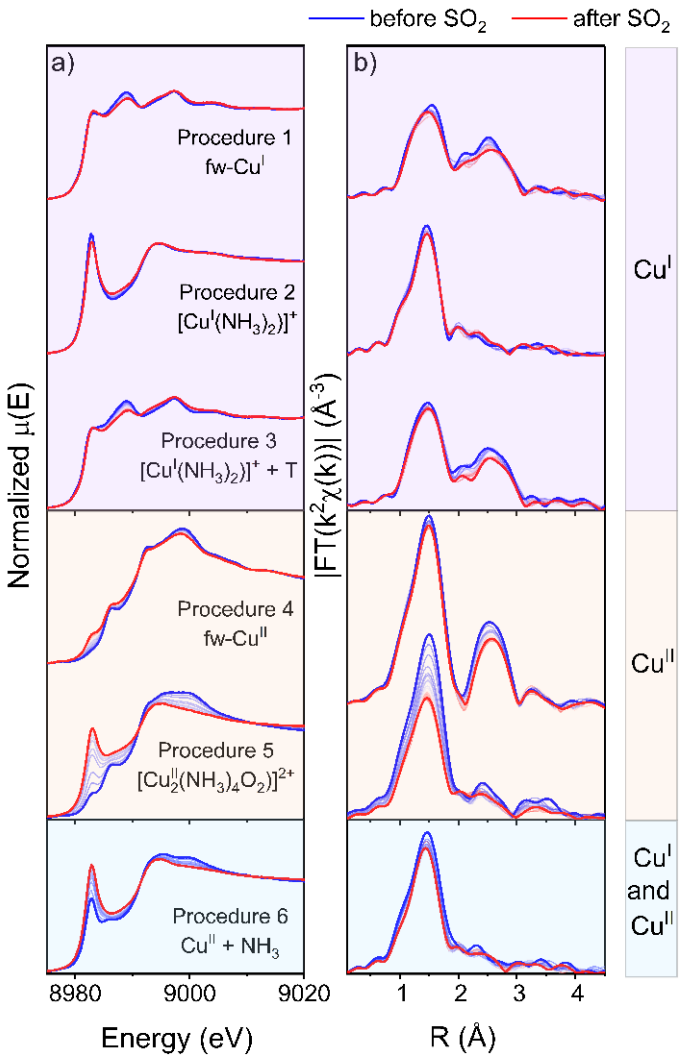

Figure 3.8. Cu K-edge XANES (a) and FT-EXAFS spectra (b) collected in situ during the exposure of Cu species obtained in Procedures 1-6 to SO2 at 200 °C for the high Cu/CHA catalyst. Reproduced from Molokova et al., 2022. [4]

For both catalysts, when Cu is in a Cu^{I} state, the spectra show minor changes during the exposure to SO_2, indicating that the interaction between SO_2 the Cu^{I} is insignificant (Procedures 1-3). Consequently, these Cu species are not likely to react with SO_2 alone during the NH_3-SCR cycle.

A similar result is observed if the sample is only exposed to O_2 (Procedure 4), indicating the limited reactivity of the fw-Cu^{II} species towards SO_2. However, the result is different when the sample with Cu^{II} coordinated to NH_3 is exposed to SO_2. We can see it in the case of Procedures 5 and 6. Cu species obtained after interaction with NH_3 demonstrate significant rearrangement in the local structure and changes in the Cu oxidation state upon interaction with SO_2. In both cases, the exposure to SO_2 causes a pronounced increase of the XANES peak at 8983 eV, characteristic for linear Cu^{I} complexes,[5-7] and a drop of the first shell intensity in the EXAFS FT, indicating the decrease in the coordination number of Cu and consequently, the decomposition of the complex. After the exposure to SO_2, the final state does not depend on the Cu content in both XANES and EXAFS results.

3.5 The most SO_2 sensitive Cu species: $[Cu_2^{II}(NH_3)_4O_2]^{2+}$

From the results of XANES and EXAFS, we found the Cu species most sensitive to SO_2 poisoning being $[Cu_2^{II}(NH_3)_4O_2]^{2+}$ complex and Cu^{II} + NH_3 species.

The $[Cu_2^{II}(NH_3)_4O_2]^{2+}$ complexes were shown to be key intermediates of the low-temperature SCR.[3, 8, 9] Their structure and properties were actively studied. Low-Cu and high-Cu catalysts demonstrate similar shapes of XANES and EXAFS spectra (Figure 3.9 a,b). The structure of the complex is shown in Figure 3.9c. We fitted the EXAFS spectrum of the high-Cu sample to confirm the assignment of the spectra to the complex. We chose the high-Cu sample for the EXAFS fitting due to the lower noise level. The resulting fit is presented in Figure 3.10 and shows perfect agreement with

the experimental spectrum. The resulting parameters in Table 3.2 agree with the ones of the $[Cu_2^{II}(NH_3)_4O_2]^{2+}$ complex.

Since, as already mentioned before, the $[Cu_2^{II}(NH_3)_4O_2]^{2+}$ complex is an essential intermediate in the NH_3-SCR cycle, its sensitivity to SO_2 is likely responsible for the decrease of the catalyst's activity at low temperatures when exposed to SO_2. When SO_2 is present in the gas feed, it may decompose the $[Cu_2^{II}(NH_3)_4O_2]^{2+}$ complex and interrupt the catalytic cycle, causing the NO conversion drop.

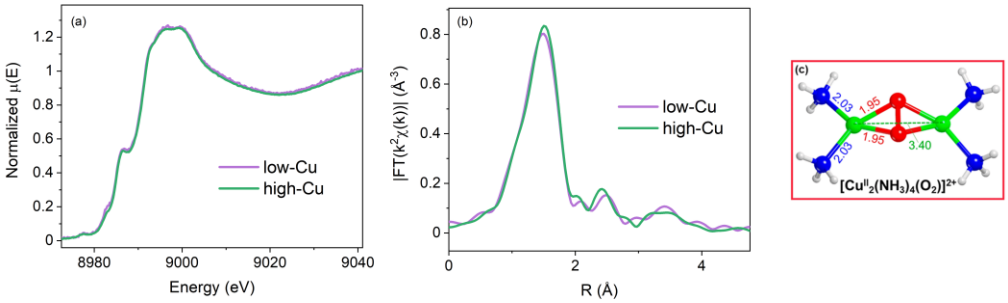

Figure 3.9 XANES (a), EXAFS (b) and structure (c)[3] of the $[Cu_2^{II}(NH_3)_4O_2]^{2+}$ complex for low-Cu and high-Cu catalysts. Panel (c) reproduced from Negri et al., 2020 [3]

Table 3.2 The results of EXAFS fitting of the $[Cu^{II}_2(NH_3)_4O_2]^{2+}$ complex. Fitting ranges: k-range = 3-13 $Å^{-1}$, R-range = 1.15-3 Å.

Cu-species	*Path*	*Parameters*	*R-factor, %*
$[Cu^{II}_2(NH_3)_4O_2]^{2+}$ *(Procedure 5)*	*Cu-O*	*N = 2, σ^2 = 0.008(1) $Å^2$, R = 1.921(1) Å*	*0.2*
	Cu-N	*N = 2, σ^2 = 0.006(1) $Å^2$, R = 2.016(1) Å*	

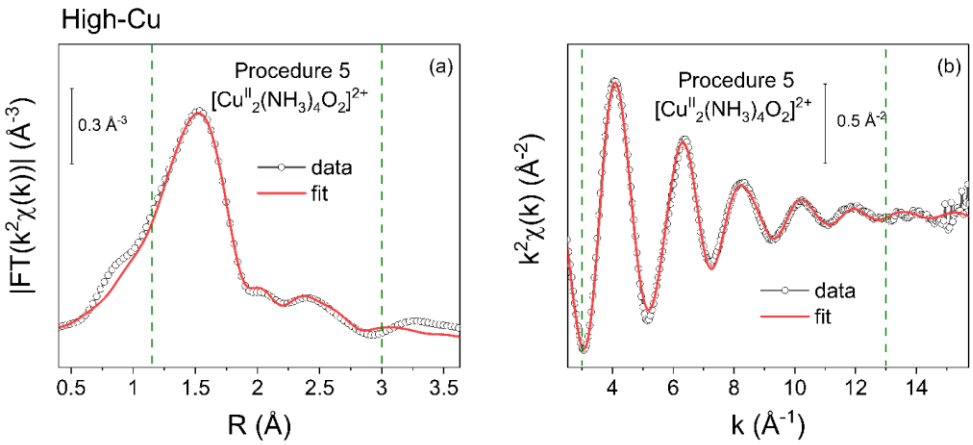

Figure 3.10 EXAFS fitting results for the $[Cu_2^{II}(NH_3)_4O_2]^{2+}$ (Procedure 5) after pre-treatment procedures in R- (left panel) and k-space (right panel) for the high-Cu catalyst. Green dashed lines show the fitting ranges.

The presence of mixed oxygen-ammonia Cu-ligation in the dimeric complexes found crucial for the reaction with SO_2, was independently confirmed by valence-to-core XES. [7, 10, 11]. Figure 3.11 presents XES spectra at different pre-treatment stages leading to $[Cu^{II}_2(NH_3)_4O_2]^{2+}$ complexes forming. The Kβ'' satellite peak in the XES spectra originates from the transition between the ligand ns orbitals and the Cu 1s orbital. This peak's position depends on the species directly coordinated to Cu, allowing discrimination between oxygen (O), nitrogen (N), and sulfur (S) ligands.[12-14] Figure 3.11 shows that after heating in O_2, Cu is predominantly coordinated by oxygens (as expected for the fw-Cu^{II} species), while after exposure to NO+NH_3 N-ligands are dominating, as expected for $[Cu^{I}(NH_3)_2]^{+}$ linear complex. After exposure to O_2 and the formation of $[Cu^{II}_2(NH_3)_4O_2]^{2+}$ complexes, the peak broadens, confirming the presence of both N- and O-ligation. Furthermore, even after exposure to SO_2, the mixed ligation is maintained, indicating the co-existence of

both nitrogen- and oxygen-coordinated Cu species. Notably, the XES spectrum collected after exposure to SO_2 does not show a significant contribution from sulfur ligands, which rules out the formation of a substantial amount of species where sulfur directly coordinates with Cu. However, the shape of the $K\beta_{2,5}$-line changes upon exposure to SO_2, indicating the decomposition of the $[Cu^{II}_2(NH_3)_4O_2]^{2+}$ complexes.

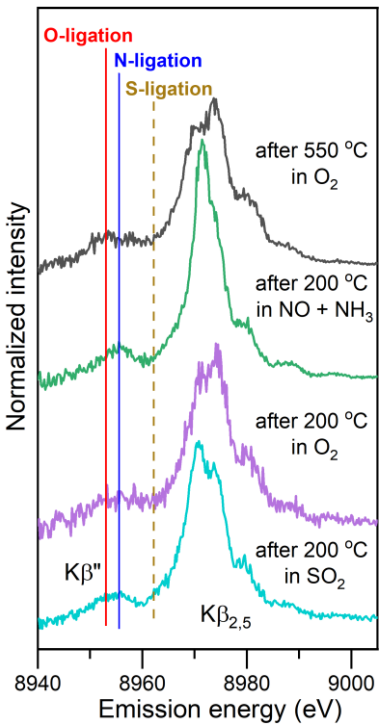

Figure 3.11 Background-subtracted Cu Kβ vtc-XES spectra for different stages of the Procedure 5 leading to the formation of $[Cu^{II}_2(NH_3)_4O_2]^{2+}$ complex. High-Cu catalyst (3.2 wt% Cu/CHA). Reproduced from Molokova et al., 2022 [4]

3.6 The most SO_2 sensitive species: Cu^{II} + NH_3

The structure of the second reactive species obtained by the exposure of fw-Cu^{II} to NH_3 is not certain. Previous studies have reported that similar pre-treatment results in the mixture of linear $[Cu^{I}(NH_3)_2]^{+}$ and either

square-planar $[Cu^{II}(NH_3)_4]^{2+}$ complexes or mixed-ligand $[Cu^{II}O_x(NH_3)_y]^{2+}$ moieties. [1, 6]

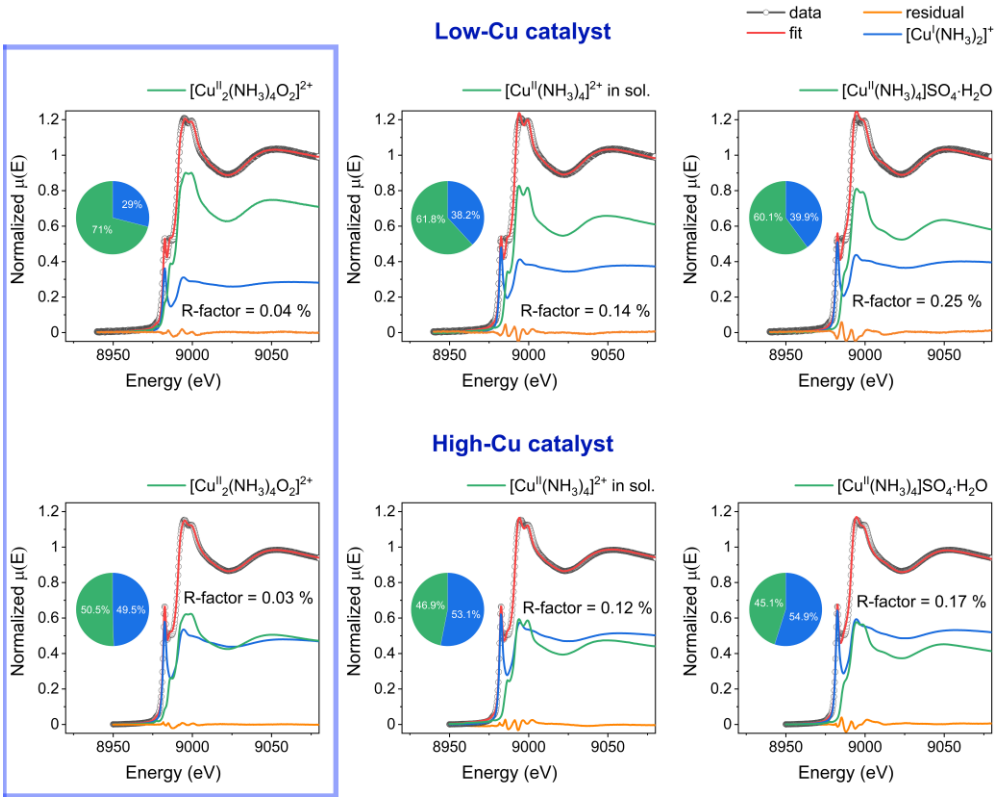

Figure 3.12 Comparison between LCF results with different references for the XANES spectrum collected after pre-treatment in Procedure 6; the reference spectra are the spectrum of linear diamine complex $[Cu^{I}(NH_3)_2]^{+}$ (the same for all fits) and oxygen-bridged diamine dicopper complex $[Cu^{II}_2(NH_3)_4O_2]^{2+}$ (left panels), tetraamine copper complex in solution $[Cu^{II}(NH_3)_4]^{2+}$ (middle panels), tetraamine copper sulfate monohydrate $[Cu^{II}(NH_3)_4]SO_4{\cdot}H_2O$ (right panels). Low-Cu (0.8 wt% Cu/CHA) and high-Cu (3.2 wt% Cu/CHA) catalysts. Adapted from Molokova et al., 2022 [4]

In our investigation, we try to resolve its structure by applying linear combination fit (LCF) with known references of $[Cu_2^{II}(NH_3)_4O_2]^{2+}$ complexes and with pure $Cu^{II}(NH_3)_4$ groups (either aqueous $[Cu^{II}(NH_3)_4]^{2+}$

or solid-state $[Cu^{II}(NH_3)_4]SO_4 \cdot H_2O$) in addition to linear $[Cu^{I}(NH_3)_2]^+$. The best agreement was obtained for a mixture of $[Cu_2^{II}(NH_3)_4O_2]^{2+}$ and $[Cu^{I}(NH_3)_2]^+$ complexes (Figure 3.12). The ratio between the two spectral components for the high-Cu catalyst was nearly 50 % / 50 %. For the low-Cu catalyst, we observed 71 % of $[Cu_2^{II}(NH_3)_4O_2]^{2+}$ and 29 % of $[Cu^{I}(NH_3)_2]^+$. The fits with tetraamino groups exhibited visible discrepancies with the data for both catalysts.

To form $[Cu_2^{II}(NH_3)_4O_2]^{2+}$ complexes, the catalyst has to be exposed to oxygen. This raises the question of the possibility of forming $[Cu_2^{II}(NH_3)_4O_2]^{2+}$ complexes after the exposure of the activated catalyst only to NH_3 without providing a source of oxygen. However, in Procedure 6, we expect that some oxygen is stored in the sample after the initial heating to 550 °C in O_2.

We applied wavelet transform (WT) analysis to EXAFS data of the high-Cu catalyst to confirm this. WT is used for distinguishing the contributions of light and heavy atoms in the EXAFS signal. [15, 16] The distinction comes from the dependence of backscattering amplitude factors on the atomic number Z. As a result, the contributions of heavier atoms are localized at higher k. With WT, it is possible to represent the signal in both R- and k-space making it possible to assign it to the scattering paths with better precision. The high-Cu catalyst was chosen due to the lower level of noise in the spectra.

Following the analogous procedure showed in works, [16, 17] we used WT to identify the presence of Cu-Cu bonds in Cu-CHA after initial heating in O_2 to 550 °C and subsequent cooling to 200 °C. The Cu-Cu contribution

is expected to be localized at ca. 6-7 $Å^{-1}$, according to the calculations of the backscattering amplitude factors[2]. Such contribution is visible in WT map of the Cu-CHA sample (Figure 3.13). Together with Z-Cu^{II}(OH) species, the dimers, that are usually oxygen-bridged, may constitute a necessary stock of oxygen needed for the formation of mixed-ligand $Cu^{II}(NH_3)_xO_y$ complexes after the subsequent treatment in NH_3 at 200 °C in Procedure 6.

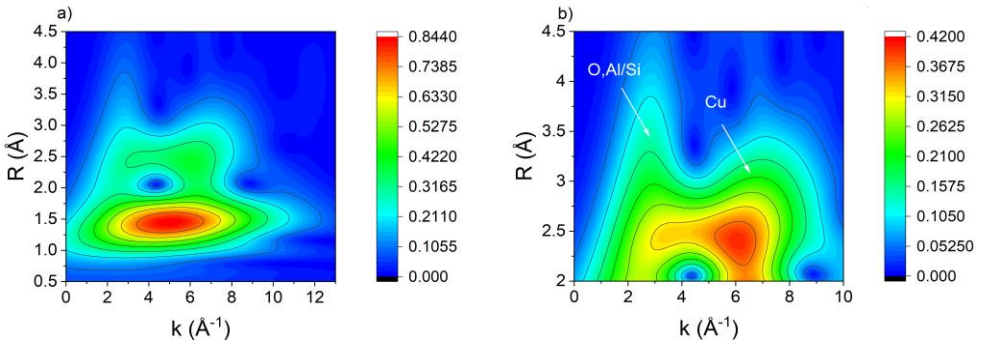

Figure 3.13 Full-range WT representation of the EXAFS signal for the high-Cu sample measured at 200 °C after heating to 550 °C in 10 % O_2/He and cooling to 200 °C; b) Magnification of the high-R WT region in ranges Δk (0-10) $Å^{-1}$ and ΔR (2-4.5) Å. WT sub-lobes stemming from O, Al/Si and Cu atomic neighbours are indicated by white arrows and labels. Reproduced from Molokova et al., 2022 [4]

To further support the proposed composition of the Cu species obtained from the linear combination fit (LCF), EXAFS fitting was performed using the Athena and Artemis software from Demeter package. [18] The EXAFS fitting results are presented in Table 3.3.

For the mixed species obtained after (Cu^{II} + NH_3) treatment in Procedure 6, the parameters of the fit (coordination numbers, Debye-Waller factors and path lengths) were taken from the fits of the corresponding

components: $[Cu_2^{II}(NH_3)_4O_2]^{2+}$ and $[Cu^{I}(NH_3)_2]^{+}$ complexes. Coordination numbers were multiplied by the N_{EXAFS} coefficient. This coefficient was defined as N_{EXFAS} = N for $[Cu_2^{II}(NH_3)_4O_2]^{2+}$ component and N_{EXAFS} = 1-N for $[Cu^{I}(NH_3)_2]^{+}$ component, where N was fitted.

Table 3.3 The results of EXAFS fitting. Fitting ranges: k-range = 3-13 $Å^{-1}$, R-range = 1.15-3 Å. Color codes of the paths correspond to the following species: green: $[Cu^{II}_2(NH_3)_4O_2]^{2+}$, light-blue: $[Cu^{I}(NH_3)_2]^{+}$. Parameters without errors in parentheses were taken from the fit of the corresponding component and fixed in the fit here

Cu-species	*N_{EXAFS}*	*Path*	*Parameters*	*R-factor, %*
Low-Cu	*0.28(2)*	*Cu-N*	*$N = 2 \cdot 0.28$, $\sigma^2 = 0.008$ Å^2, R = 1.91 Å*	0.4
(Cu^{II} + NH_3)	*0.72(2)*	*Cu-N*	*$N = 2 \cdot 0.72$, $\sigma^2 = 0.003$ Å^2, R = 2.03 Å*	
(Procedure 6)		*Cu-O*	*$N = 2 \cdot 0.72$, $\sigma^2 = 0.004$ Å^2, R = 1.92 Å*	
High-Cu	*0.50(3)*	*Cu-N*	*$N = 2 \cdot 0.5$, $\sigma^2 = 0.008$ Å^2, R = 1.91 Å*	*0.7*
(Cu^{II} + NH_3)	*0.50(3)*	*Cu-N*	*$N = 2 \cdot 0.5$, $\sigma^2 = 0.003$ Å^2, R = 2.03 Å*	
(Procedure 6)		*Cu-O*	*$N = 2 \cdot 0.5$, $\sigma^2 = 0.004$ Å^2, R = 1.92 Å*	

The resulting values of N_{EXAFS} are close to those obtained from LCF: 0.29/0.71 (LCF) and 0.28/0.72 (EXAFS fit) for low-Cu catalyst, and 0.51/0.49 (LCF) and 0.50/0.50 (EXAFS fit) for high-Cu catalyst.

Figure 3.14 shows the resulting fits in k- and R-space. For low-Cu and high-Cu catalysts the agreement is sufficiently good.

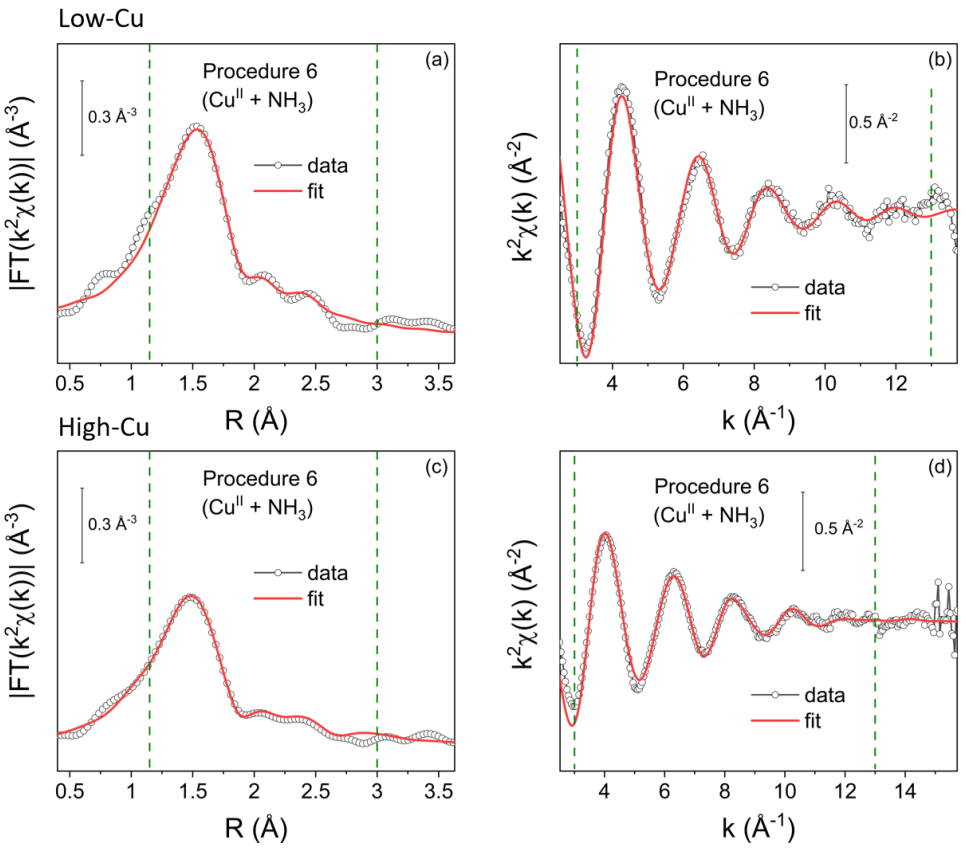

Figure 3.14 EXAFS fitting results for the outcome of (Cu^{II}+NH_3) treatment (Procedure 6) after pre-treatment procedures in R- (left panels) and k-space (right panels). Green dashed lines show the fitting ranges. a,b) Low-Cu catalyst (0.8 wt% Cu/CHA); c,d) High-Cu catalyst (3.2 wt% Cu/CHA). Adapted from Molokova et al., 2022 [4]

3.7 SO_2 uptake

To verify our findings from XANES and EXAFS results, we estimate the uptake of SO_2 by the catalysts for each of the 6 Procedures. We use two different methods for that. The first is XAQ,[19] described in detail in the Experimental, Section 2.3.1. It was measured in situ together with XAS. The S/Cu ratio, in this case, is calculated from the change in the total absorption of the sample due to the accumulation of SO_2 in the sample.

The second method is Temperature Programmed Desorption of SO_2 (SO_2-TPD). The desorption of SO_2 is monitored as a function of temperature while heating the sample. In this case, the amount of SO_2 was measured on the saturated sample after the in situ experiment. The SO_2-TPD curves for low-Cu and high-Cu catalysts are presented in Figure 3.15.

First, by comparing the obtained TPD curves with references, we can exclude the formation of $(NH_4)_2SO_4$ as a main reason for deactivation. $(NH_4)_2SO_4$ can be formed in a reaction of SO_2 with NH_3 and NH_4^+ groups stored in the zeolite framework. However, for the adsorbed $(NH_4)_2SO_4$ (reference sample composed by a Cu free CHA impregnated with $(NH_4)_2SO_4$)we observe SO_2 desorption at around 380 °C, 530 °C, and 1000 °C (grey curve in Figure 3.15). The desorption at 380 °C matches the known thermal decomposition of $(NH_4)_2SO_4$;[20] the other two peaks are probably due to the interaction of either $(NH_4)_2SO_4$ or products of its decomposition with the zeolite, their precise interpretation being beyond the scope of the present argument. For both catalysts and all three Cu-CHA samples containing NH_3 before exposure to SO_2 ($[Cu^{I}(NH_3)_2]^+$, $[Cu^{II}_2(NH_3)_4O_2]^{2+}$ and (Cu^{II} + NH_3) procedures), we observe SO_2 desorption around 420 °C (Figure 3.15). As this does not match any of the observed desorption characteristics of $(NH_4)_2SO_4$ in Cu-free Cu-CHA, the SO_2-TPD feature at 420 °C reflects an interaction of Cu with SO_2. Finally, integrating the SO_2-TPD curves allows us to calculate the S/Cu ratio in the catalyst independently on the SO_2-saturated sample.

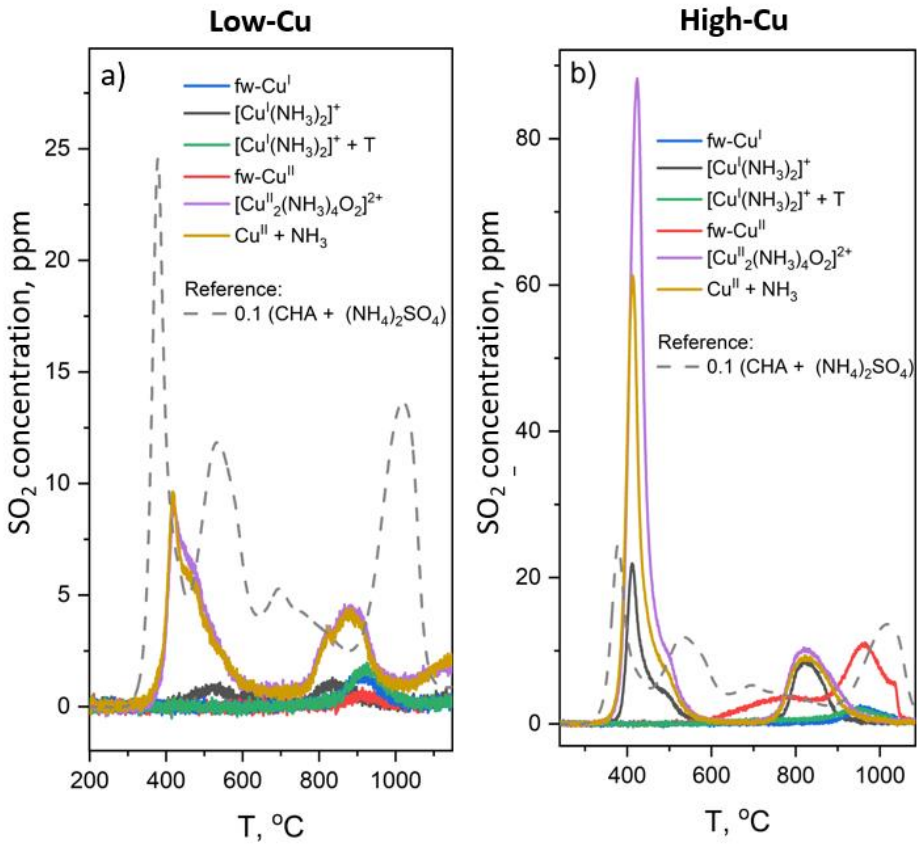

Figure 3.15 SO_2-TPD profiles collected after exposing the species obtained in Procedures 1-6 to SO_2 compared to reference SO_2-TPD curve of a CHA zeolite without Cu impregnated with 20 wt% $(NH_4)_2SO_4$, downscaled x10. a) Low-Cu catalyst (0.8 wt% Cu/CHA); b) High-Cu catalyst (3.2 wt% Cu/CHA). Adapted from Molokova et al., 2022 [4].

We calculated the S/Cu ratio using the two methods and compared them for the low-Cu and high-Cu catalysts for all six procedures. The results are presented in Figure 3.16. For both catalysts, we find the highest sulfur content (S/Cu ratio) for the $[Cu^{II}_2(NH_3)_4O_2]^{2+}$ and $Cu^{II} + NH_3$ procedures. The sulfur uptake of the $[Cu^{I}(NH_3)_2]^+$ and fw-Cu^{II} moieties was ca. 3 times lower, and for the bare fw-Cu^{I} species, it was ca. 6 times lower. These results show that the reaction between the $[Cu^{II}_2(NH_3)_4O_2]^{2+}$ species and

SO_2 contributes most to the accumulation of SO_2 in the Cu-CHA catalyst. This agrees with the XANES and EXAFS results discussed earlier. Namely, complexes containing Cu^{II} coordinated to NH_3 are the most reactive to SO_2.

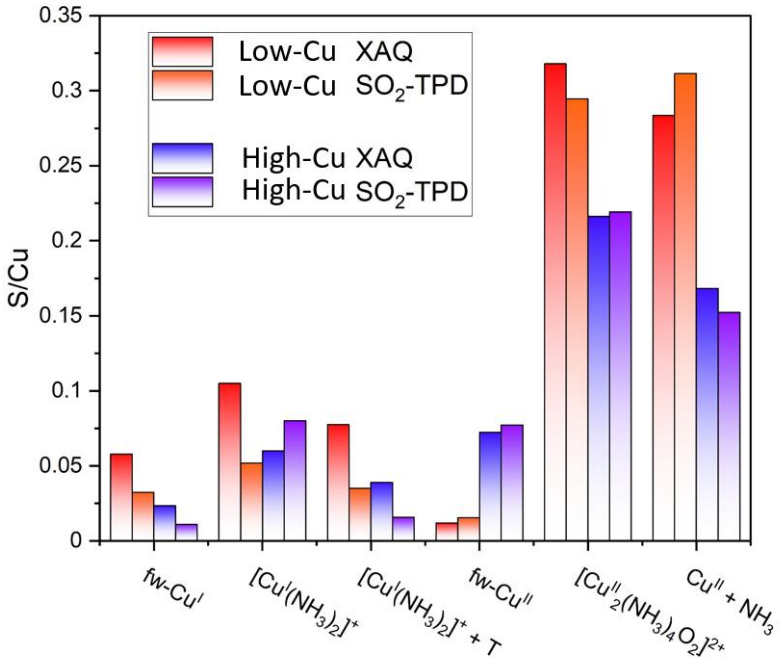

Figure 3.16 The S/Cu ratio in the samples after exposure to SO_2 obtained from SO_2-TPD and XAQ. Low-Cu catalyst (0.8 wt% Cu/CHA) and High-Cu catalyst (3.2 wt% Cu/CHA). Adapted from Molokova et al., 2022 [4]

The obtained maximum level of S/Cu ratio does not exceed 0.3-0.35 after 3 hours of exposure of the reactive complexes to SO_2. During the experiment, we monitored the shape of XANES to ensure that the spectra did not change anymore at the end of the exposure of the catalyst to SO_2, indicating that the reaction was finished. To verify that the SO_2 uptake by the sample also reached saturation, we plot the evolution of the S/Cu ratio

extracted from the XAQ signal during the in situ exposure to SO_2 of the two reactive complexes in low-Cu and high-Cu catalysts (Figure 3.17). It is possible to distinguish two regions: the fast growth of the S/Cu ratio during the first 20-30 minutes and the saturation region. We can see that by the end of the 3 hours of exposure to SO_2, the changes in the XAQ signal become small, indicating the stabilization of the system. With the time evolution of the XAQ signal, we can monitor the saturation of the S/Cu signal together with the shape of XANES spectra.

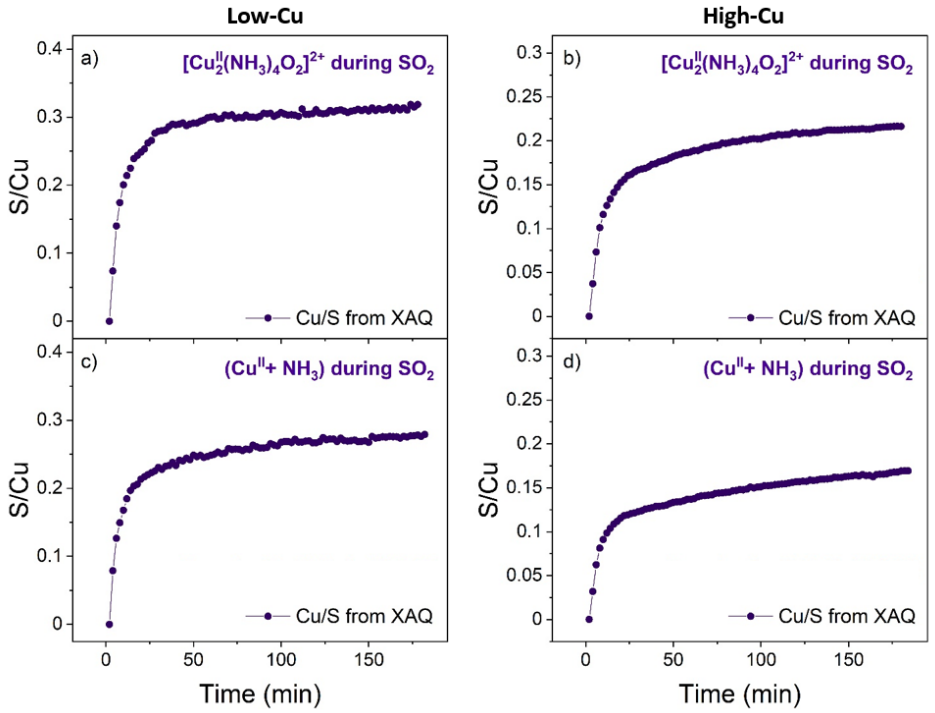

Figure 3.17 Evolution of S/Cu ratio extracted from XAQ signal during the exposure to SO_2 of (a,b) $[Cu_2^{II}(NH_3)_4O_2]^{2+}$ obtained in Procedure 5 and (c,d) (Cu^{II} + NH_3) species obtained in Procedure 6. Left panels: low-Cu catalyst (0.8 wt% Cu/CHA), and right panels: high-Cu catalyst (3.2 wt% Cu/CHA).

3.8 Conclusions

This Chapter is dedicated to different Cu species forming in the Cu-CHA catalyst during the NH_3-SCR cycle and their interaction with SO_2. Two samples with different Cu content were investigated: low-Cu (0.8 wt% Cu/CHA) and high-Cu (3.2 wt% Cu/CHA). The *in situ* XAS and XES measurements of different Cu intermediates formed in Cu-CHA catalyst exposed to SO_2 demonstrate that Cu^{II} species with mixed NH_3 and O-ligation of Cu are susceptible to SO_2 poisoning. In contrast, Cu^{I} and Cu^{II} without NH_3 are much less affected by it.

These results are confirmed by estimating the SO_2 uptake by the catalyst from in situ XAQ and SO_2-TPD on the SO_2-saturated samples. In the case of the two SO_2 reactive species ($[Cu_2^{II}(NH_3)_4O_2]^{2+}$ and (Cu^{II}+NH_3)), the low-Cu catalyst shows slightly higher S/Cu saturation levels, probably because not all of the S in the catalyst is associated with Cu.

One of the most vulnerable species is $[Cu_2^{II}(NH_3)_4O_2]^{2+}$ complex, the key intermediate of the low-temperature SCR reaction. Reaction with SO_2 leads to its decomposition and accumulation of sulfur in the zeolite, which explains the loss of the low-temperature activity of the material in NH_3-SCR upon SO_2 poisoning.

3.9 References

1. Borfecchia, E.; Negri, C.; Lomachenko, K. A.; Lamberti, C.; Janssens, T. V. W.; Berlier, G., Temperature-dependent dynamics of NH3-derived Cu species in the Cu-CHA SCR catalyst. *React Chem Eng* **2019,** *4* (6), 1067-1080.
2. Martini, A.; Borfecchia, E.; Lomachenko, K. A.; Pankin, I. A.; Negri, C.; Berlier, G.; Beato, P.; Falsig, H.; Bordiga, S.; Lamberti, C., Composition-driven Cu-speciation and reducibility in Cu-CHA zeolite catalysts: a multivariate XAS/FTIR approach to complexity. *Chem Sci* **2017,** *8* (10), 6836-6851.

3. Negri, C.; Selleri, T.; Borfecchia, E.; Martini, A.; Lomachenko, K. A.; Janssens, T. V. W.; Cutini, M.; Bordiga, S.; Berlier, G., Structure and Reactivity of Oxygen-Bridged Diamino Dicopper(II) Complexes in Cu-Ion-Exchanged Chabazite Catalyst for NH3-Mediated Selective Catalytic Reduction. *J. Am. Chem. Soc.* **2020,** *142* (37), 15884-15896.
4. Molokova, A. Y.; Borfecchia, E.; Martini, A.; Pankin, I. A.; Atzori, C.; Mathon, O.; Bordiga, S.; Wen, F.; Vennestrøm, P. N. R.; Berlier, G.; Janssens, T. V. W.; Lomachenko, K. A., SO2 Poisoning of Cu-CHA deNOx Catalyst: The Most Vulnerable Cu Species Identified by X-ray Absorption Spectroscopy. *JACS Au* **2022,** *2* (4), 787–792.
5. Kau, L. S.; Spira-Solomon, D. J.; Penner-Hahn, J. E.; Hodgson, K. O.; Solomon, E. I., X-ray absorption edge determination of the oxidation state and coordination number of copper. Application to the type 3 site in Rhus vernicifera laccase and its reaction with oxygen. *J. Am. Chem. Soc.* **1987,** *109* (21), 6433-6442.
6. Janssens, T. V. W.; Falsig, H.; Lundegaard, L. F.; Vennestrom, P. N. R.; Rasmussen, S. B.; Moses, P. G.; Giordanino, F.; Borfecchia, E.; Lomachenko, K. A.; Lamberti, C.; Bordiga, S.; Godiksen, A.; Mossin, S.; Beato, P., A Consistent Reaction Scheme for the Selective Catalytic Reduction of Nitrogen Oxides with Ammonia. *ACS Catal.* **2015,** *5* (5), 2832-2845.
7. Giordanino, F.; Borfecchia, E.; Lomachenko, K. A.; Lazzarini, A.; Agostini, G.; Gallo, E.; Soldatov, A. V.; Beato, P.; Bordiga, S.; Lamberti, C., Interaction of NH3 with Cu-SSZ-13 Catalyst: A Complementary FTIR, XANES, and XES Study. *J. Phys. Chem. Lett.* **2014,** *5* (9), 1552-1559.
8. Paolucci, C.; Khurana, I.; Parekh, A. A.; Li, S. C.; Shih, A. J.; Li, H.; Di Iorio, J. R.; Albarracin-Caballero, J. D.; Yezerets, A.; Miller, J. T.; Delgass, W. N.; Ribeiro, F. H.; Schneider, W. F.; Gounder, R., Dynamic multinuclear sites formed by mobilized copper ions in NOx selective catalytic reduction. *Science* **2017,** *357* (6354), 898-903.
9. Chen, L.; Janssens, T. V. W.; Vennestrom, P. N. R.; Jansson, J.; Skoglundh, M.; Gronbeck, H., A Complete Multisite Reaction Mechanism for Low-Temperature NH3-SCR over Cu-CHA. *ACS Catal.* **2020,** *10* (10), 5646-5656.
10. Gunter, T.; Carvalho, H. W. P.; Doronkin, D. E.; Sheppard, T.; Glatzel, P.; Atkins, A. J.; Rudolph, J.; Jacob, C. R.; Casapu, M.; Grunwaldt, J. D., Structural snapshots of the SCR reaction mechanism on Cu-SSZ-13. *Chemical Communications* **2015,** *51* (44), 9227-9230.
11. Gunter, T.; Doronkin, D. E.; Boubnov, A.; Carvalho, H. W. P.; Casapu, M.; Grunwaldt, J. D., The SCR of NOx with NH3 Examined by Novel X-ray Emission and X-ray Absorption Methods. *Topics in Catalysis* **2016,** *59* (10-12), 866-874.
12. Lomachenko, K. A.; Borfecchia, E.; Negri, C.; Berlier, G.; Lamberti, C.; Beato, P.; Falsig, H.; Bordiga, S., The Cu-CHA deNO$_x$ catalyst in action:

temperature-dependent NH_3-assisted selective catalytic reduction monitored by operando XAS and XES. *J. Am. Chem. Soc.* **2016,** *138* (37), 12025−12028.
13. Glatzel, P.; Bergmann, U., High resolution 1s core hole X-ray spectroscopy in 3d transition metal complexes - electronic and structural information. *Coordination Chemistry Reviews* **2005,** *249* (1-2), 65-95.
14. Vegelius, J. R.; Kvashnina, K. O.; Klintenberg, M.; Soroka, I. L.; Butorin, S. M., Cu K beta(2,5) X-ray emission spectroscopy as a tool for characterization of monovalent copper compounds. *Journal of Analytical Atomic Spectrometry* **2012,** *27* (11), 1882-1888.
15. Timoshenko, J.; Kuzmin, A., Wavelet data analysis of EXAFS spectra. *Comput Phys Commun* **2009,** *180* (6), 920-925.
16. Martini, A.; Signorile, M.; Negri, C.; Kvande, K.; Lomachenko, K. A.; Svelle, S.; Beato, P.; Berlier, G.; Borfecchia, E.; Bordiga, S., EXAFS wavelet transform analysis of Cu-MOR zeolites for the direct methane to methanol conversion. *Phys Chem Chem Phys* **2020,** *22* (34), 18950-18963.
17. Martini, A.; Bugaev, A. L.; Guda, S. A.; Guda, A. A.; Priola, E.; Borfecchia, E.; Smolders, S.; Janssens, K.; De Vos, D.; Soldatov, A. V., Revisiting the Extended X-ray Absorption Fine Structure Fitting Procedure through a Machine Learning-Based Approach. *Journal of Physical Chemistry A* **2021,** *125* (32), 7080-7091.
18. Ravel, B.; Newville, M., ATHENA and ARTEMIS Interactive Graphical Data Analysisusing IFEFFIT. *Physica Scripta* **2005,** *T115*, 1007–1010.
19. Lomachenko, K. A.; Molokova, A. Y.; Atzori, C.; Mathon, O., Quantification of Adsorbates by X-ray Absorption Spectroscopy: Getting TGA-like Information for Free. *The Journal of Physical Chemistry C* **2022,** *126* (11), 5175–5179.
20. Kiyoura, R.; Urano, K., Mechanism, Kinetics, and Equilibrium of Thermal Decomposition of Ammonium Sulfate. *Industrial & Engineering Chemistry Process Design and Development* **1970,** *9* (4), 489-494.

4 SO_2 poisoning mechanism and identification of sulfated species

The results are accepted for publication in Chemical Science in 2023:

Elucidating the reaction mechanism of SO_2 with Cu-CHA catalysts for NH_3-SCR by X-ray absorption spectroscopy. *Anastasia Yu. Molokova, Reza K. Abasabadi, Elisa Borfecchia, Olivier Mathon, Silvia Bordiga, Fei Wen, Gloria Berlier, Ton V.W. Janssens and Kirill A. Lomachenko Chemical Science* ***2023***

4.1 Introduction

In the previous Chapter, we identified that $[Cu_2^{II}(NH_3)_4O_2]^{2+}$ complexes are the most reactive to SO_2 among Cu intermediates forming in the Cu-CHA catalyst during the NH_3-SCR cycle. From the XANES and EXAFS results, we understood that the interaction with SO_2 leads to the decomposition of the $[Cu_2^{II}(NH_3)_4O_2]^{2+}$ complexes and the reduction of Cu. However, the mechanism of their interaction with SO_2 and the nature of the formed species still need to be understood.

This Chapter provides a more detailed analysis of the interaction between $[Cu_2^{II}(NH_3)_4O_2]^{2+}$ complexes and SO_2, including the identification of the reaction intermediates by applying XAS spectra decomposition techniques and identification of the structure of the sulfated Cu species by measuring S K-edge XAS and S K_α XES.

The reduction of Cu observed upon exposure of the $[Cu_2^{II}(NH_3)_4O_2]^{2+}$ complexes to SO_2 inspired an experiment where SO_2 was mixed with O_2 to oxidize Cu^I and increase the SO_2 uptake. Another experiment included

a series of subsequent exposures of $[Cu_2^{II}(NH_3)_4O_2]^{2+}$ complexes to SO_2 and O_2 separately to investigate their individual effects.

Finally, this Chapter proposes a reaction mechanism for the $[Cu_2^{II}(NH_3)_4O_2]^{2+}$ complexes and SO_2 based on the discussed results.

4.2 Samples

This Chapter investigates Cu-CHA samples with 0.8 wt% Cu/CHA and 3.2 wt% Cu/CHA. The designation of the samples is low-Cu (0.8 wt% Cu/CHA) and high-Cu (3.2 wt% Cu-CHA).

4.3 Experimental methods

In this chapter, we used in situ Cu K-edge XAS (XANES and EXAFS) for monitoring the oxidation state of the Cu during the experiment; in situ S K-edge XANES for monitoring the oxidation state and local environment of S accumulated in the catalyst; XAQ calculations for estimating the SO_2 uptake by the catalyst during the experiment; SO_2-TPD measurements on the saturated sample for estimating the SO_2 uptake by the catalyst after the experiment; S Kα XES for identification of the local environment of S accumulated in the sample; EXAFS fitting, Linear Combination fitting (LCF) and Multivariate Curve Resolution Alternating least squares (MCR-ALS) analysis for the identification of the Cu intermediates and the sulfated species forming during the experiment.

4.4 Experimental protocol

Experimental procedures aimed to expose the $[Cu_2^{II}(NH_3)_4O_2]^{2+}$ complex to SO_2, a mixture to $SO_2/O_2/He$, and cycles of SO_2 and O_2. The detailed schemes containing the information on the temperatures, gas

compositions, and timing are presented in Figure 4.1, Figure 4.2 and Figure 4.3.

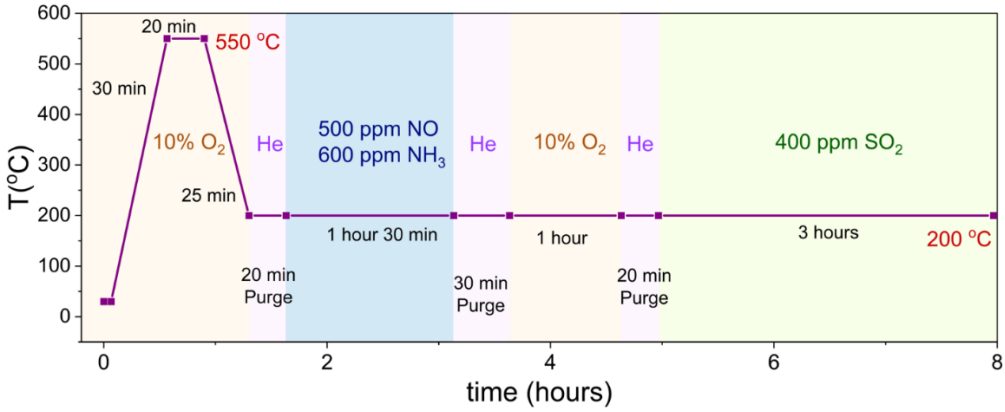

Figure 4.1. Scheme of the experimental protocol of the exposure of the $[Cu^{II}_2(NH_3)_4O_2]^{2+}$ to SO_2. Same as Protocol 5 in Section 3.

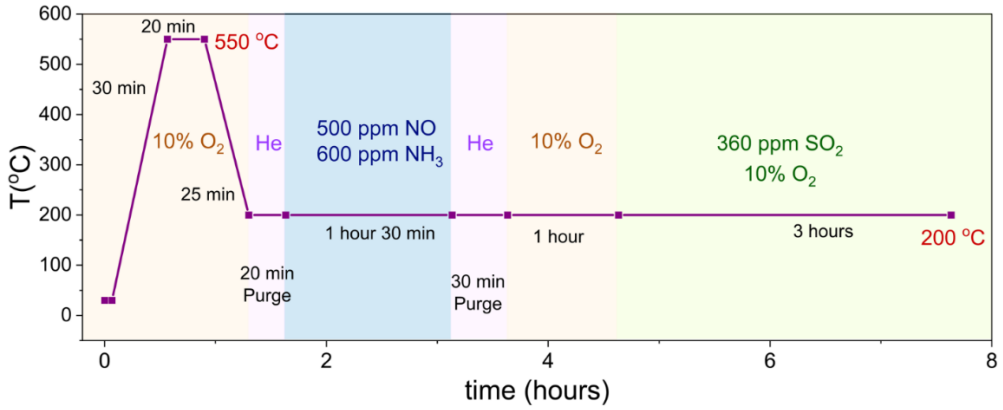

Figure 4.2. Scheme of the experimental protocol of the exposure of the $[Cu^{II}_2(NH_3)_4O_2]^{2+}$ to a mixture of SO_2/O_2/He.

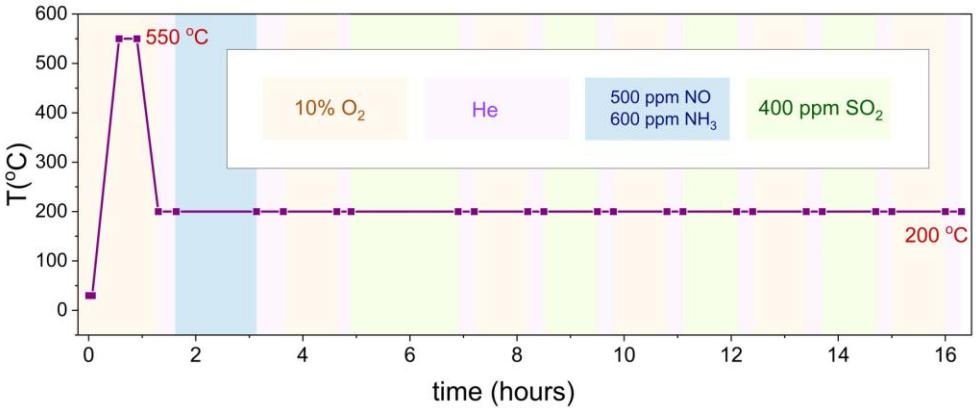

Figure 4.3. Scheme of the experimental protocol of the exposure of the $[Cu^{II}_2(NH_3)_4O_2]^{2+}$ to the cycles of SO_2 and O_2.

4.5 Exposure to SO_2 without O_2

The exposure of the $[Cu_2^{II}(NH_3)_4O_2]^{2+}$ complexes to SO_2 is already described in the previous Chapter. Here, the changes in XANES and EXAFS spectra are investigated in more detail.

Figure 4.4 shows the Cu-K edge XANES and EXAFS FT data collected during the exposure of $[Cu_2^{II}(NH_3)_4O_2]^{2+}$ complex to SO_2 at 200 °C for the low-Cu/CHA and high-Cu/CHA catalysts. The observed trends in the XANES and EXAFS spectra in these measurements are similar, indicating that the reaction of SO_2 proceeds similarly for both catalysts. There is an apparent increase of the XANES peak at 8983 eV, indicating the partial reduction of Cu^{II} to Cu^{I}, and a decrease in the intensity of the first shell in the EXAFS FT, indicating a reduction of the coordination number, which indicates the decomposition of the $[Cu_2^{II}(NH_3)_4O_2]^{2+}$ complex. [1]

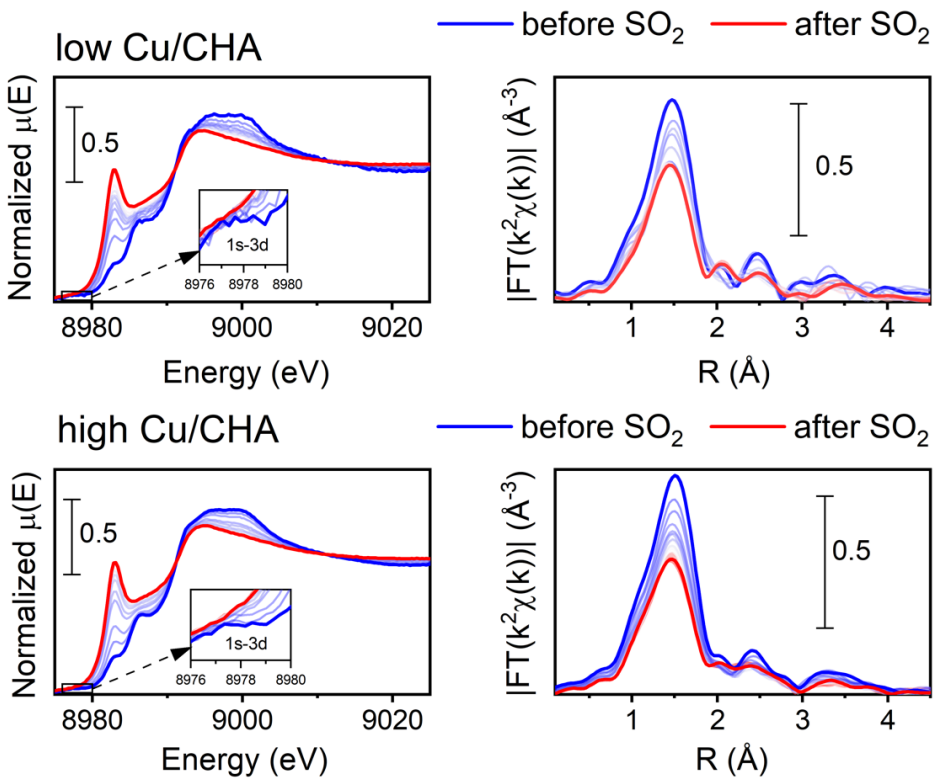

Figure 4.4. Cu K-edge XANES (a) and FT-EXAFS spectra (b) collected in situ during the exposure of $[Cu_2^{II}(NH_3)_4O_2]^{2+}$ species to SO_2 at 200 °C of low Cu/CHA (0.8 wt% Cu/CHA) and high Cu/CHA(3.2 wt% Cu/CHA) catalysts. Reproduced from Molokova et al., 2023. [1]

A better understanding of the reaction of SO_2 with the $[Cu_2^{II}(NH_3)_4O_2]^{2+}$ complex is needed. To extract more information from XANES, we apply a combination of XAS spectra decomposition techniques to our dataset.

As already mentioned in the Introduction, this Chapter discusses three in situ experiments at Cu K-edge: $[Cu_2^{II}(NH_3)_4O_2]^{2+}$ complexes exposed to SO_2, $[Cu_2^{II}(NH_3)_4O_2]^{2+}$ complexes exposed to SO_2+O_2, and $[Cu_2^{II}(NH_3)_4O_2]^{2+}$ complexes exposed to cycles of SO_2 and O_2. For

applying the XAS spectra decomposition techniques, it is convenient to consider these three experiments in one dataset.

We apply a combination of Multivariate Curve Resolution alternating least squares method (MCR-ALS) [2, 3] and Linear combination fitting (LCF). Usually, experimental spectra are used as references for the LCF of the data. However, because the species formed after the exposure to SO_2 are unknown, it is impossible to identify proper reference spectra for the reaction with SO_2. Therefore, we combined the LCF procedure with MCR-ALS to resolve the shape of XANES spectra of the unknown components. [1]

The MCR analysis utilized a dataset of six sets of spectra: two sets for the procedure involving SO_2 only, two for the procedure involving SO_2+O_2, and two for SO_2/O_2-cycles. The two sets for each procedure included data for low-Cu and high-Cu catalysts. By resolving these six datasets together, we were able to obtain the known spectra of fw-Cu^{II}, $[Cu^{I}(NH_3)_2]^+$, fw-Cu^{I}, and $[Cu_2^{II}(NH_3)_4O_2]^{2+}$ and a new spectrum which we assigned as "sulfated component". Some spectra generated by MCR have artefacts, so we took experimental spectra as references instead. The choice of references is explained in detail below.

We chose one set of references for all datasets for LCF. The first reference is fw-Cu^{II}. The spectrum obtained with MCR has some artefacts in the pre-edge region, so we took an experimental spectrum (Figure 4.5a). We chose the spectrum of the low-Cu sample because it was closer in shape to the MCR-generated spectrum and, therefore, can be considered a purer reference in this case.

The experimental spectra of $[Cu^{I}(NH_3)_2]^+$ were very similar to the spectrum generated by MCR, so we took the experimental spectrum of $[Cu^{I}(NH_3)_2]^+$ for the sample with higher Cu content due to a lower level of noise. The spectra of $[Cu_2^{II}(NH_3)_4O_2]^{2+}$ complex of low-Cu and high-Cu samples were very similar, so we employed the spectrum of the high-Cu catalyst as a reference because of its lower noise. The spectrum corresponding to fw-Cu^{I} was taken from the MCR because the spectra of the two samples collected in the conditions that favored the formation of fw-Cu^{I} species were noticeably different (Figure 4.5b). However, since the spectral features were qualitatively the same, the difference in the experimental spectra is most probably due to the different content of minority species (such as fw-Cu^{II}), whereas the dominant component deduced by MCR and corresponding to pure fw-Cu^{I} species is the same for both samples.

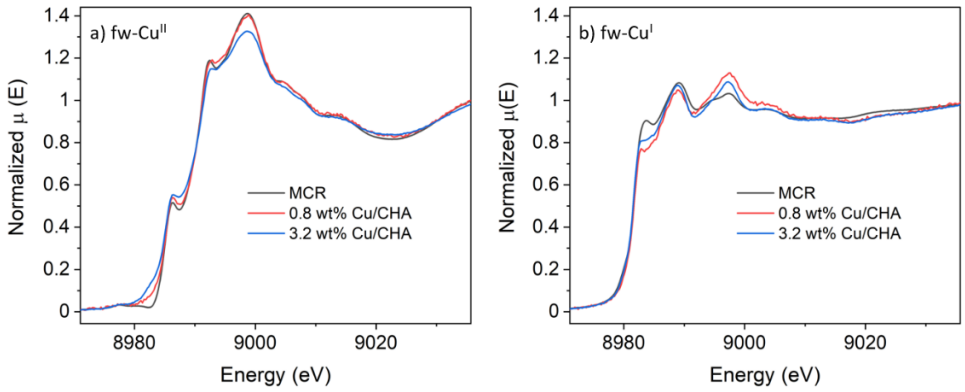

Figure 4.5 Comparison of the spectra of fw-CuII (a) and fw-CuI (b) generated by MCR and experimental spectra of the low-Cu and high-Cu catalysts, for choosing the reference components for LCF. Reproduced from Molokova et al., 2023. [1]

Figure 4.6 shows the reference spectra used in the linear combination fits.

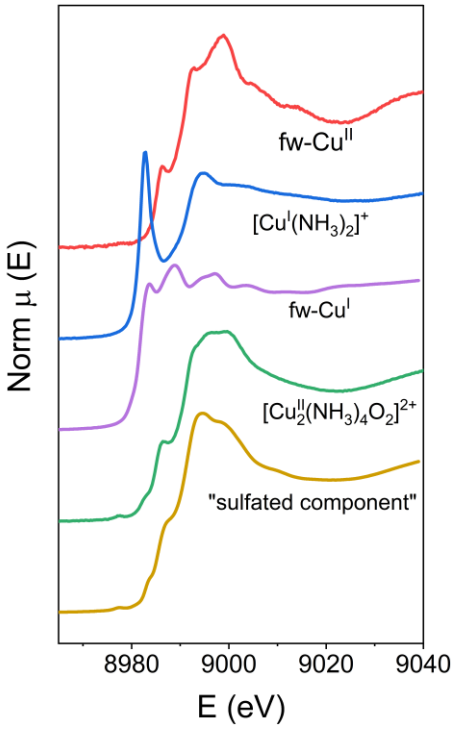

Figure 4.6. Spectra used as references in the linear combination fit. The spectra of fw-Cu^{II}, [Cu^{I}(NH$_3$)$_2$]$^+$ and [Cu$_2^{II}$(NH$_3$)$_4$O$_2$]$^{2+}$ are experimental spectra. The spectra of fw-Cu^{I} and the "sulfated component" was obtained with MCR-ALS. Reproduced from Molokova et al., 2023. [1]

Figure 4.7 presents the resulting concentration profiles for the different Cu compounds obtained from the linear combination for both the low-Cu/CHA and the high-Cu/CHA catalysts. When the [Cu$_2^{II}$(NH$_3$)$_4$O$_2$]$^{2+}$ complex is exposed to SO_2, the sulfated component's concentration increases, confirming this component's assignment to the S-containing species. The final fraction of the sulfated component is 17 % in the high Cu/CHA sample and 22 % in the low Cu/CHA sample. After the exposure to SO_2, we find around 50 % of the Cu present as the linear [Cu^{I}(NH$_3$)$_2$]$^+$ complex, and 25 % as fw-Cu^{I}, confirming that most Cu in the catalyst is reduced to Cu^{I}.

Importantly, the $[Cu_2^{II}(NH_3)_4O_2]^{2+}$ complex is no longer present after exposure to SO_2, consistent with the high reactivity of this complex with SO_2.

The results of LCF indicate that the reaction of the $[Cu_2^{II}(NH_3)_4O_2]^{2+}$ complex with SO_2 is not very much affected by the Cu content, the fractions of different components are very similar for low-Cu and high-Cu catalysts.

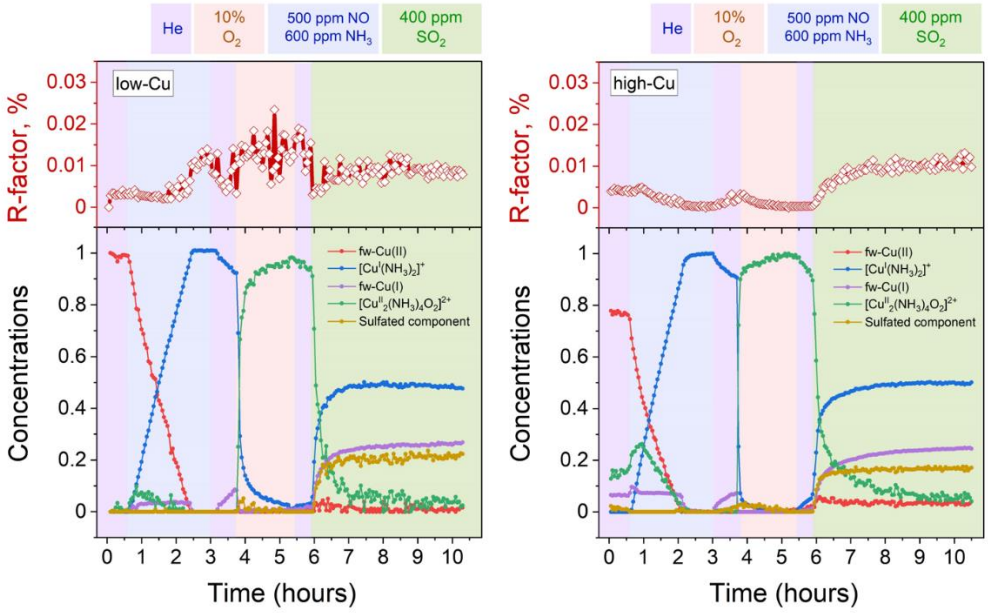

Figure 4.7. Quantification of Cu compounds during the in-situ Cu-K edge XANES measurements from linear combination fits, using the reference spectra shown in Figure 2. Upper panels: R-factors of the linear combination fits. Lower panels: Concentration profiles for the different Cu species during reduction in NH_3+NO, the formation of the $[Cu_2^{II}(NH_3)_4O_2]^{2+}$-complex, and exposure of the $[Cu_2^{II}(NH_3)_4O_2]^{2+}$-complex to SO_2, for the low-Cu/CHA (left) and high-Cu/CHA (right) catalysts. Reproduced from Molokova et al., 2023. [1]

4.6 Exposure to SO_2 in the presence O_2

Following the exposure of $[Cu_2^{II}(NH_3)_4O_2]^{2+}$ dimers to SO_2, around 50 % of the Cu species transform into $[Cu^{I}(NH_3)_2]^{+}$. And the exposure of $[Cu^{I}(NH_3)_2]^{+}$ to O_2 leads to the formation of $[Cu_2^{II}(NH_3)_4O_2]^{2+}$ complexes as it is already well known. [4-6] These complexes subsequently can react with SO_2. Consequently, to enhance the SO_2 uptake, the samples need to be exposed to a mixture of SO_2 + O_2. This exposure facilitates the regeneration of $[Cu_2^{II}(NH_3)_4O_2]^{2+}$ complexes from $[Cu^{I}(NH_3)_2]^{+}$, thus increasing the SO_2 uptake process. [1]

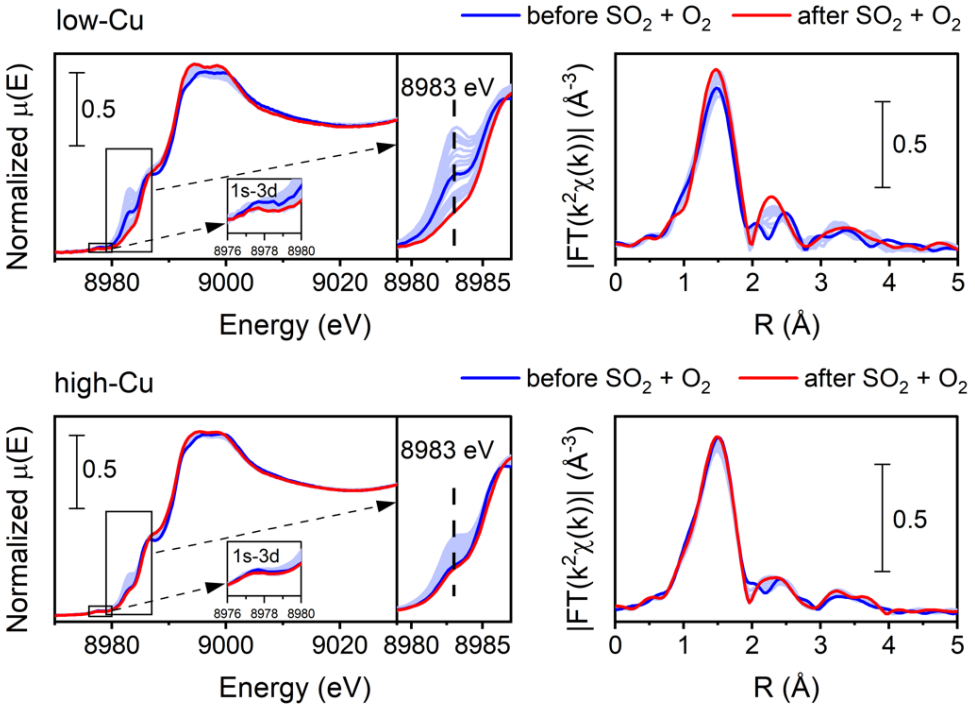

Figure 4.8. Cu K-edge XANES (a) and FT-EXAFS spectra (b) collected in situ during the exposure of $[Cu_2^{II}(NH_3)_4O_2]^{2+}$ species to 360 ppm SO_2 and 10 % O_2 at 200 °C low-Cu (0.8 wt% Cu/CHA) and high-Cu (3.2 wt% Cu/CHA) catalysts. Reproduced from Molokova et al., 2023. [1]

Figure 4.8 shows the evolution of XANES and EXAFS FT when exposing the $[Cu_2^{II}(NH_3)_4O_2]^{2+}$ complex to a mixture of 360 ppm SO_2 and 10 % O_2 at 200 ºC. XANES spectra reveal a slight initial increase and subsequent decrease of the peak at 8983 eV, corresponding to the formation of $[Cu^{I}(NH_3)_2]^{+}$ complexes. This indicates that intermediate Cu^{I} species are formed during this experimental stage. These Cu^{I} species react with O_2 and form Cu^{II} species as predicted. The presence of Cu^{II} species can be seen from the 1s-3d transition at 8978 eV.[1] The presented XANES results suggest a similar interaction mechanism as in the reaction of the $[Cu_2^{II}(NH_3)_4O_2]^{2+}$ complex with SO_2 only.

EXAFS FT results indicate that the average coordination number of the first shell of Cu remains close to four since the intensity of the first peak does not exhibit significant changes. That shows that 4-coordinated Cu species are dominant after exposure to $SO_2 + O_2$. Moreover, the second peak becomes more pronounced, evidencing the presence of a relatively heavy neighbor at a well-defined distance in the second shell of Cu. The possible candidates are Si or Al from the zeolitic framework or S in case of the formation of sulfated species.[1]

Figure 4.9 displays the resulting concentration profiles of Cu species obtained by the combined MCR-ALS and LCF fitting of the XANES spectra collected during the formation of the $[Cu_2^{II}(NH_3)_4O_2]^{2+}$ followed by the exposure to the $SO_2 + O_2$ mixture. The LCF fit used the same set of references as for the procedure involving only SO_2. Compared to the results obtained after exposure to SO_2 in the absence of O_2, the fraction of the sulfated component has become significantly larger, especially for the low-Cu sample. Furthermore, both samples show a transient increase of

fw-Cu^{I} and diamino $[Cu^{I}(NH_3)_2]^+$ components at the beginning of the exposure to SO_2 + O_2, but very rapidly their concentration goes to zero. This confirms that the reaction with SO_2 proceeds similarly with and without O_2 in the gas mixture.

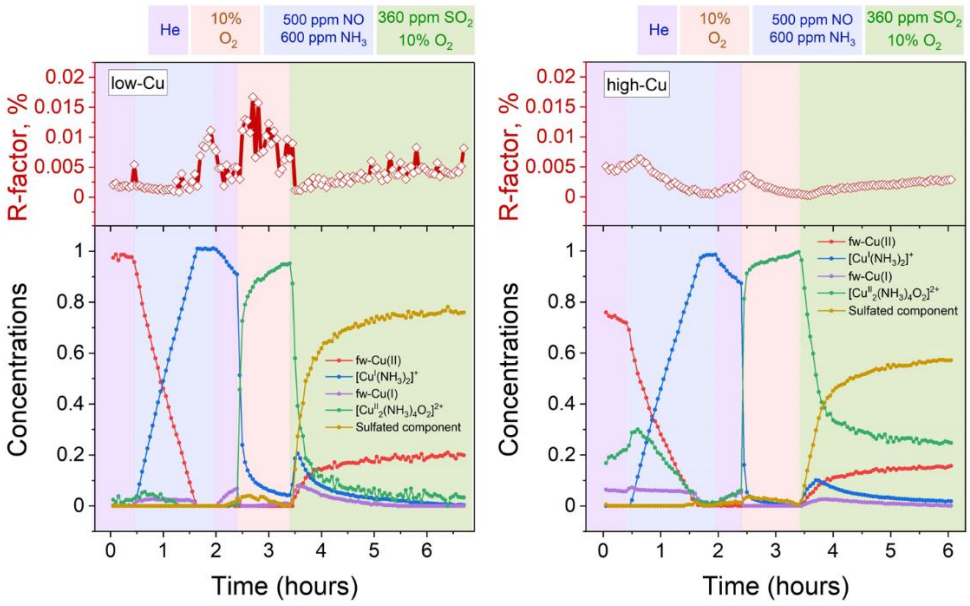

Figure 4.9. Quantification of Cu compounds during the in situ Cu K-edge XANES measurements from LCF, using the reference spectra shown in Figure 2. Upper panels: R-factors of the linear combination fits. Lower panels: Concentration profiles for the different Cu species during reduction in NH_3 + NO, the formation of the $[Cu_2^{II}(NH_3)_4O_2]^{2+}$-complex, and exposure of the $[Cu_2^{II}(NH_3)_4O_2]^{2+}$-complex to SO_2 + O_2, for the low-Cu (left) and high-Cu (right) catalysts. Reproduced from Molokova et al., 2023. [1]

The final state for the low-Cu catalyst consists of around 80 % of the sulfated component and 20 % of fw-Cu^{II}. For the high-Cu sample, there is around 60 % of the sulfated component, 25 % of $[Cu_2^{II}(NH_3)_4O_2]^{2+}$, and 15 % of fw-$Cu^{II}$. In the high-Cu sample, a significant fraction of component assigned to $[Cu_2^{II}(NH_3)_4O_2]^{2+}$ complex remains even after

exposure to SO_2 + O_2. To further investigate this effect and better understand the role of oxygen in the reaction, an experiment with a series of subsequent exposures to SO_2 and O_2 is needed.

4.7 Alternating exposure to SO_2 and O_2

In the procedure SO_2/O_2 cycles, $[Cu_2^{II}(NH_3)_4O_2]^{2+}$ complexes were exposed to alternating switches between SO_2 and O_2; the results of the LCF are shown in Figure 4.10. Upon exposure to SO_2 in the first two cycles, the $[Cu_2^{II}(NH_3)_4O_2]^{2+}$ complexes underwent decomposition, resulting in the formation of fw-Cu^I, $[Cu^I(NH_3)_2]^+$ and the species corresponding to the sulfated component. However, in the subsequent 3rd and 4th cycles, the sulfated component did not exhibit significant growth during the exposure to SO_2. At each subsequent exposure to SO_2, less and less Cu^I is formed, concomitantly with a decreasing amount of the $[Cu_2^{II}(NH_3)_4O_2]^{2+}$ component.

In the case of the low-Cu sample, the conversion of $[Cu_2^{II}(NH_3)_4O_2]^{2+}$ complexes at each step was nearly complete. In contrast, for the high-Cu sample, almost complete conversion was observed only after the initial exposure to SO_2. The effect of the "unreactive" $[Cu_2^{II}(NH_3)_4O_2]^{2+}$ component is observed as after exposure of the high-Cu catalyst to SO_2 + O_2 discussed in the previous section (Figure 4.9). Also, the concentration of the "unreactive" $[Cu_2^{II}(NH_3)_4O_2]^{2+}$ component stabilizes at approximately the same level as after exposure of the high-Cu catalyst to SO_2 + O_2. At each subsequent exposure to SO_2, less and less Cu^I is formed, concomitantly with a decreasing amount of the "reactive" $[Cu_2^{II}(NH_3)_4O_2]^{2+}$ component. Two explanations can be suggested for this effect.

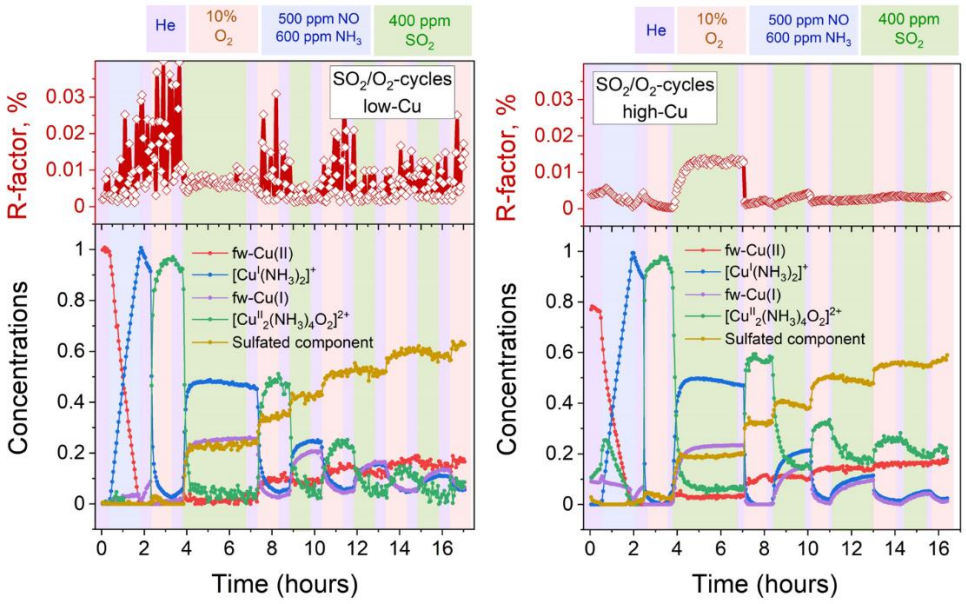

Figure 4.10. Quantification of Cu compounds during the in situ Cu K-edge XANES measurements from linear combination fits, using the reference spectra shown in Figure 2. Upper panels: R-factors of the linear combination fits. Lower panels: Concentration profiles for the different Cu species during reduction in NH_3+NO, the formation of the $[Cu_2^{II}(NH_3)_4O_2]^{2+}$ complex, and consequent exposures of the $[Cu_2^{II}(NH_3)_4O_2]^{2+}$ complex to SO_2 and O_2, for the low-Cu (left) and high-Cu (right) catalysts. Reproduced from Molokova et al., 2023. [1]

The first one suggests that some of the $[Cu_2^{II}(NH_3)_4O_2]^{2+}$ complexes become physically inaccessible to SO_2. This could happen due to physical poisoning of the Cu-CHA catalyst proposed by Bjerregaard et al. [7] According to this mechanism, the formation of the sulfated species prevents the mobility of $[Cu^{I}(NH_3)_4]^{+}$ in the catalyst's cages. A similar effect can explain the non-reactivity of some $[Cu_2^{II}(NH_3)_4O_2]^{2+}$ complexes to SO_2. The inaccessibility of the $[Cu_2^{II}(NH_3)_4O_2]^{2+}$ complexes to SO_2 may also happen when two $[Cu_2^{II}(NH_3)_4O_2]^{2+}$ complexes occupy the same cage, thus impeding the interaction with SO_2 and the formation of a sulfated

component. This conclusion agrees with earlier measurements of a limited uptake of SO_2 in Cu-CHA catalysts [8, 9], and the observation that Cu-CHA catalysts show residual activity after saturation with SO_2 [8]. With such an interpretation, the structure of $[Cu_2^{II}(NH_3)_4O_2]^{2+}$ complex remains unchanged, directly reflected in the XANES spectra.

The second explanation for the persistence of the component assigned to $[Cu_2^{II}(NH_3)_4O_2]^{2+}$ complex involves a transformation of the $[Cu_2^{II}(NH_3)_4O_2]^{2+}$ complex to a different structure, having similar coordination of the Cu-ions. A possible candidate is a peroxo-dicopper complex Cu_2O_2 attached to framework, [10] which can be formed by exposure of the Cu-CHA to O_2 at 400-500 °C. Such species are expected to have a very similar XANES spectrum as the $[Cu_2^{II}(NH_3)_4O_2]^{2+}$ complexes because the coordination of the Cu-ions is similar, and the oxidation state is the same. Therefore, XANES spectra of such framework-bound complexes may be difficult to distinguish from those of $[Cu_2^{II}(NH_3)_4O_2]^{2+}$ complex by MCR-ALS analysis, which merges them into a single component.

This explanation is also supported by the presence of the component assigned to $[Cu_2^{II}(NH_3)_4O_2]^{2+}$ complexes during the initial oxidation of the high-Cu catalyst at 500 °C in the pre-treatment part of the experiment. At this stage of the protocol, it would be impossible to form $[Cu_2^{II}(NH_3)_4O_2]^{2+}$ complexes due to the absence of NH_3, which is required for the formation of the $[Cu_2^{II}(NH_3)_4O_2]^{2+}$ complexes.

Also, since the peroxo-dicopper complexes Cu_2O_2 are essentially fw-Cu^{II} species, their reactivity to SO_2 is very low, as shown in Chapter 3 and our recent paper. [11]

4.8 Uptake of SO_2 monitored by XAQ and SO_2-TPD

The goal of adding O_2 in the gas mixture with SO_2 was to increase the SO_2 uptake by the catalyst. The results of XAS decomposition techniques in previous sections show an increase of the component assigned to sulfated species. In this section the SO_2 uptake by the catalyst is discussed. It was quantified by two methods: X-ray adsorbate quantification (XAQ) [12] and SO_2-TPD.

The XAQ was described in detail in Section 2.3.1. This technique relies on the phenomenon that the total absorption of X-rays depends on the composition of the sample. Therefore, the increase in total X-ray absorption during SO_2 exposure reflects the increase in the amount of SO_2 in the sample. So, the S/Cu ratio can be calculated. S/Cu ratio from the XAQ signal was calculated during the in situ XAS experiment, where $[Cu_2^{II}(NH_3)_4O_2]^{2+}$ complexes were exposed to SO_2 alone and to SO_2+O_2 gas mixture. Figure 4.11 shows the measured XAQ signals for the low Cu and high Cu catalysts during exposure to SO_2 and SO_2 + O_2. All S/Cu curves have a similar shape, exhibiting rather fast changes in the first 30-40 minutes of the measurement, followed by a much slower growth at a later stage. The final S/Cu levels reached in the presented experiments are 0.32 for the low-Cu sample and 0.22 for the high-Cu sample. In the presence of O_2, the final levels increase to S/Cu=1.04 and 0.63 for the low-Cu and high-Cu catalysts, respectively.

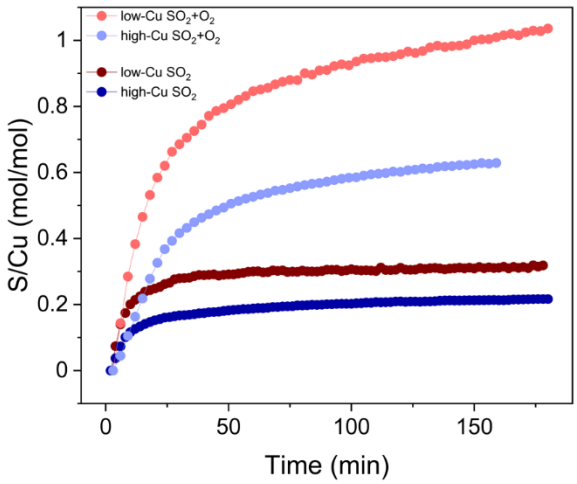

Figure 4.11. S/Cu ratio calculated from XAQ during exposure to SO_2 and SO_2+O_2 for low-Cu (0.8 wt% Cu/CHA) and high Cu (3.2 wt% Cu/CHA) catalysts. Reproduced from Molokova et al., 2023. [1]

The second method to measure SO_2 uptake is SO_2-TPD. It is applied to a saturated sample. We used the samples that we measured in situ XAS. In SO_2-TPD, the desorption of SO_2 is monitored as a function of temperature during heating of the catalyst. Figure 4.12 shows the SO_2-TPD data for the two catalysts after exposure to SO_2 and SO_2 + O_2; the SO_2-TPD of a Cu-free CHA a Cu-free CHA impregnated with $(NH_4)_2SO_4$ is included for comparison. All desorption curves for the Cu-CHA catalysts show a desorption feature in the range of 400-600 °C and one in the range of 750-1000 °C. Because these profiles are different from that of the adsorbed $(NH_4)_2SO_4$ on the Cu-free zeolite reference, we conclude that the SO_2 in the Cu-CHA catalysts predominantly interacts with the Cu, [11] without a significant amount of free $(NH_4)_2SO_4$. This agrees with the conclusion that SO_2 mainly reacts with the $[Cu_2^{II}(NH_3)_4O_2]^{2+}$ complex. The features in the range 750-1000 °C remain largely unaffected by the presence of O_2, while the peak around 420 °C becomes larger and shows a slight shift towards

higher temperatures. These results indicate that the presence of O_2 leads to a larger amount of SO_2 in the Cu-CHA catalysts and that SO_2 binds predominantly to the Cu ions in the zeolite, in agreement with our earlier results [11].

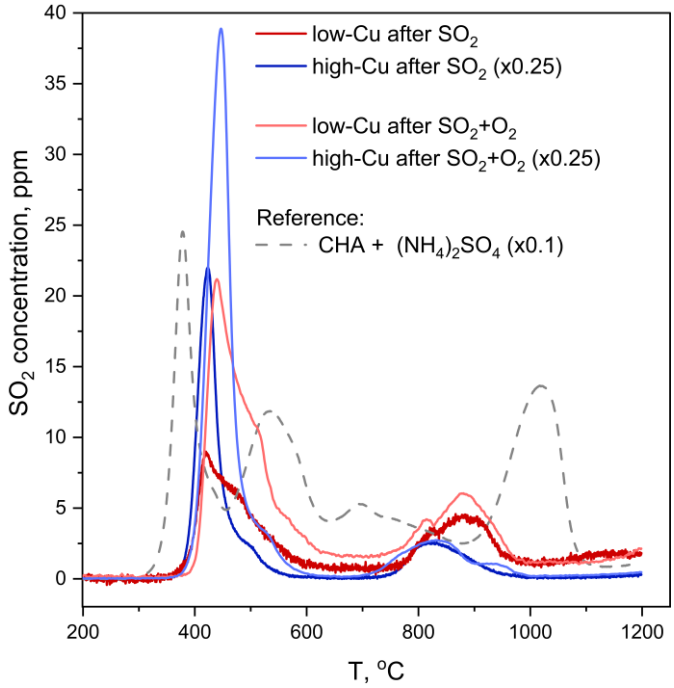

Figure 4.12. SO_2-TPD profiles collected after exposure of the catalysts to SO_2 (red and blue lines) and SO_2+O_2 (orange and light blue lines) in comparison to a reference SO_2-TPD curve of a Cu-free CHA zeolite impregnated with 20 wt % $(NH_4)_2SO_4$, downscaled ×10. Pre-treatment is the same as for the procedures followed by in situ XAS. The curves for the high Cu catalysts (3.2 wt% Cu/CHA) (blue and light blue lines) are downscaled ×4. Reproduced from Molokova et al., 2023. [1]

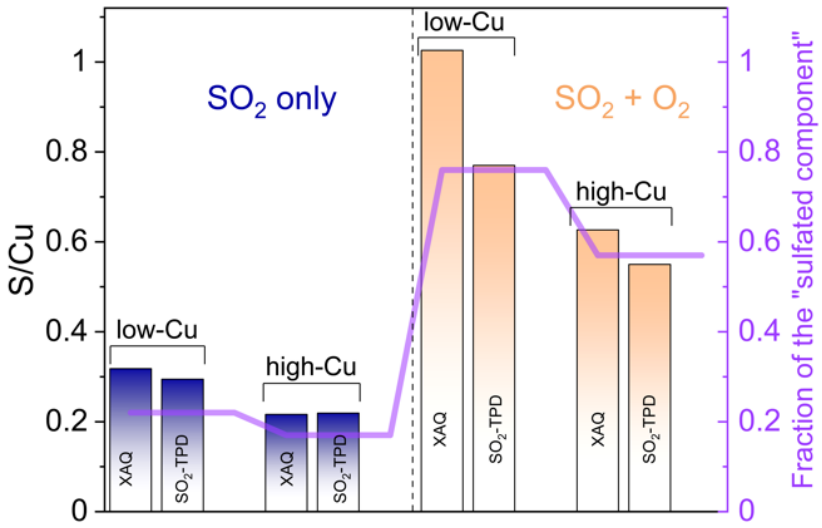

Figure 4.13 S/Cu ratios in the low-Cu (0.8 wt% Cu/CHA) and high-Cu (3.2 wt% Cu/CHA) samples after exposure to SO_2 and $SO_2 + O_2$ obtained from XAQ and SO_2-TPD compared to the concentration of the sulfated component obtained from the XANES LCF. Reproduced from Molokova et al., 2023. [1]

XAQ and TPD show that exposure to SO_2+O_2 leads to a greater sulfur uptake compared to the exposure to only SO_2 (Figure 4.13). Importantly, the S/Cu molar ratio is in good correspondence with the concentration of the sulfated component in the XANES LCF, which confirms the assignment of the latter mainly to sulfated species. [1] Also, there is a good agreement between XAQ and SO_2-TPD, confirming again the reliability of XAQ.

4.9 Sulfur K-edge XANES and Kα XES

To resolve the oxidation state of sulfur and the structure of sulfur species in the sulfated Cu-CHA catalyst, we measured S K-edge XANES during the exposure of the $[Cu_2^{II}(NH_3)_4O_2]^{2+}$ complex to SO_2 and Kα-XES spectra at the end of the exposure. Figure 4.14 shows the evolution of S K-edge

XANES spectra during exposure of the $[Cu_2^{II}(NH_3)_4O_2]^{2+}$ complex to SO_2. The spectra were collected in fluorescence. The increase of the edge jump corresponds to the increasing concentration of sulfur, which means that S is accumulated in the sample.

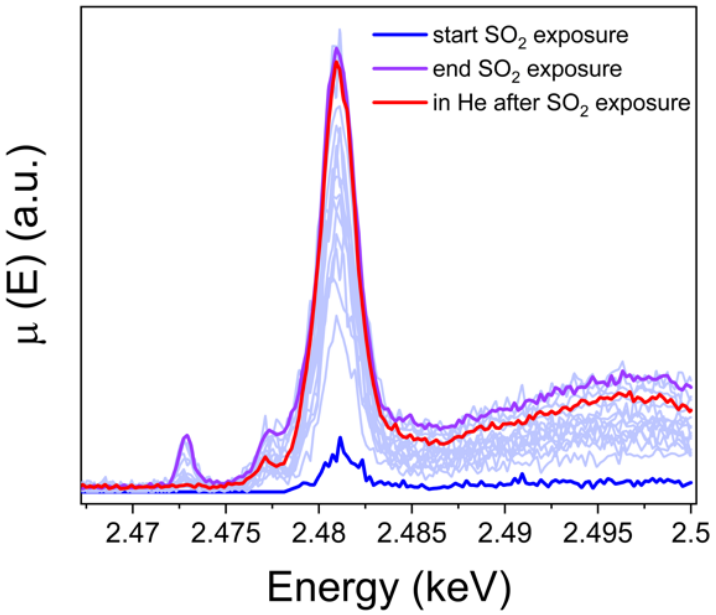

Figure 4.14. S K-edge XANES spectra of the high-Cu catalyst (3.2 wt% Cu/CHA) collected in situ during exposure of the $[Cu_2^{II}(NH_3)_4O_2]^{2+}$ complex to SO_2 at 200 °C and in He after exposure to SO_2. Reproduced from Molokova et al., 2023. [1]

To identify the structure the sulfated species and the oxidation state of S, the XANES and K_α XES spectra of the catalyst after exposure to SO_2 were compared with references. The comparison is presented in Figure 4.15. Panel (a) shows that S in the sample predominately exists in the S^{6+} oxidation state, most probably forming an SO_4^{2-} group. Panel (b) presents K_α XES spectra of the $[Cu_2^{II}(NH_3)_4O_2]^{2+}$ complex after exposure to SO_2 in comparison with references. The positions of the two features at 2.3066 and 2.3078 keV in the K_α XES and the shape of the K_α line of the complex

agree well with the references containing S^{6+} in SO_4^{2-} group, which is in line with the findings from S K-edge XANES. [1]

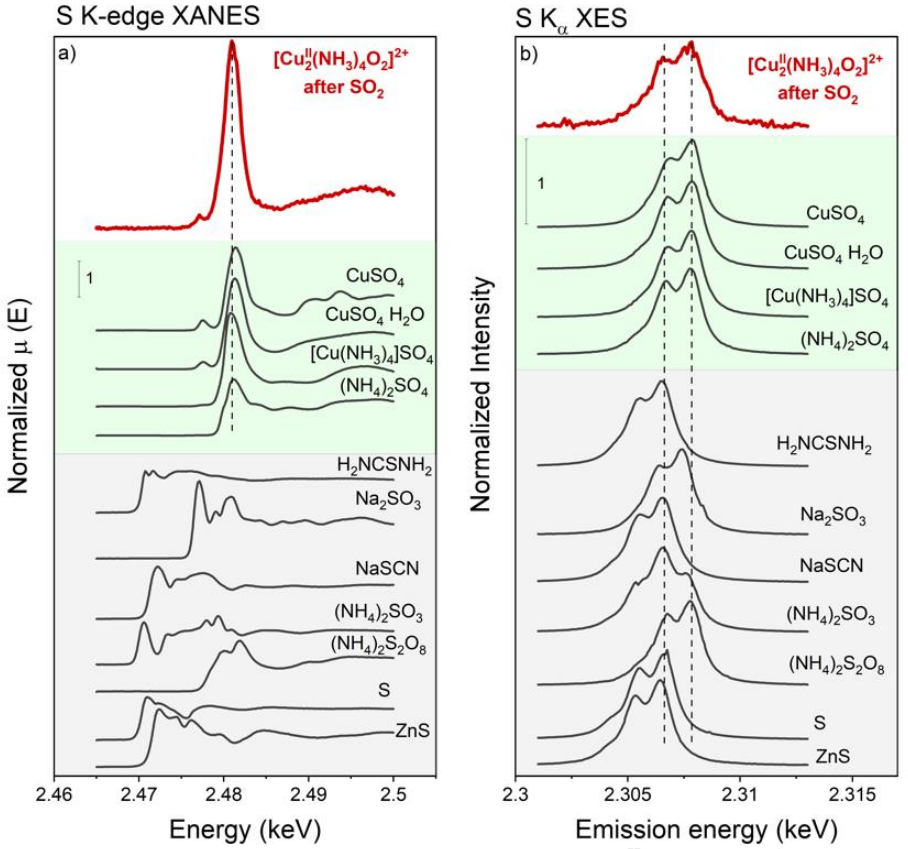

Figure 4.15. S K-edge XANES spectra of the $[Cu_2^{II}(NH_3)_4O_2]^{2+}$ complex exposed to SO_2 and of the reference compounds. K-alpha XES spectra of the $[Cu_2^{II}(NH_3)_4O_2]^{2+}$ complex exposed to SO_2 and references. High-Cu catalyst (3.2 wt% Cu/CHA). Reproduced from Molokova et al., 2023. [1]

4.10 The sulfated component

Among the spectra obtained by MCR-ALS in Section 4.5 we can identify the $[Cu^I(NH_3)_2]^+$, fw-Cu^{II}, fw-Cu^I and $[Cu_2^{II}(NH_3)_4O_2]^{2+}$ complexes. The structures of some of these species are still under debate, but the pre-treatment procedures to obtain the corresponding spectra and the oxidation state of Cu in these species are well known. Together with the known

species, we obtained a new component, which we assigned to sulfated species. The assignment is confirmed by the fact that it appears when the catalyst is exposed to SO_2 and by the correlation of the concentration of the sulfated component and the SO_2 uptake shown in Section 4.8. Section 4.9 also unravels the oxidation state and local environment of S atoms (S^{6+} in an SO_4^{2-} group). From XANES results in Section 4.6, it is possible to suggest that Cu in the sulfated component exists in Cu^{2+} oxidation state. However, a more detailed study of the structure of the sulfated component would improve the investigation of the reaction mechanism.

To elucidate the structure of the species associated with the sulfated component, we compared the spectrum generated by MCR-ALS with the experimental spectra of 3 references: $[Cu^{II}(NH_3)_4]SO_4 \cdot H_2O$, the $[Cu_2^{II}(NH_3)_4O_2]^{2+}$ complex formed in Cu-CHA and $Cu_2^{II}(NH_3)_4$ complex in solution (Figure 4.16). The XANES spectrum of the sulfated species is very similar to the spectrum of $Cu(NH_3)_4SO_4 \cdot H_2O$. Therefore, we propose that the species give rise to the sulfated component contain 4-coordinated Cu^{II} in the square-planar environment similar to the one of $Cu(NH_3)_4SO_4$, where a square-planar Cu^{II} ion is coordinated to four NH_3 ligands. It is also possible that a geometrically similar Cu^{II} configuration with mixed NH_3/O ligands realizes in the zeolite, since the XANES spectrum is expected to be very similar. Because the S atoms are not directly coordinated to the Cu in the structure of the $[Cu^{II}(NH_3)_4]SO_4 \cdot H_2O$, and the Cu-S distance is about 4.6 Å, it is not possible to determine the precise location of the S atom in the sulfated species in the zeolite based on XANES data alone.

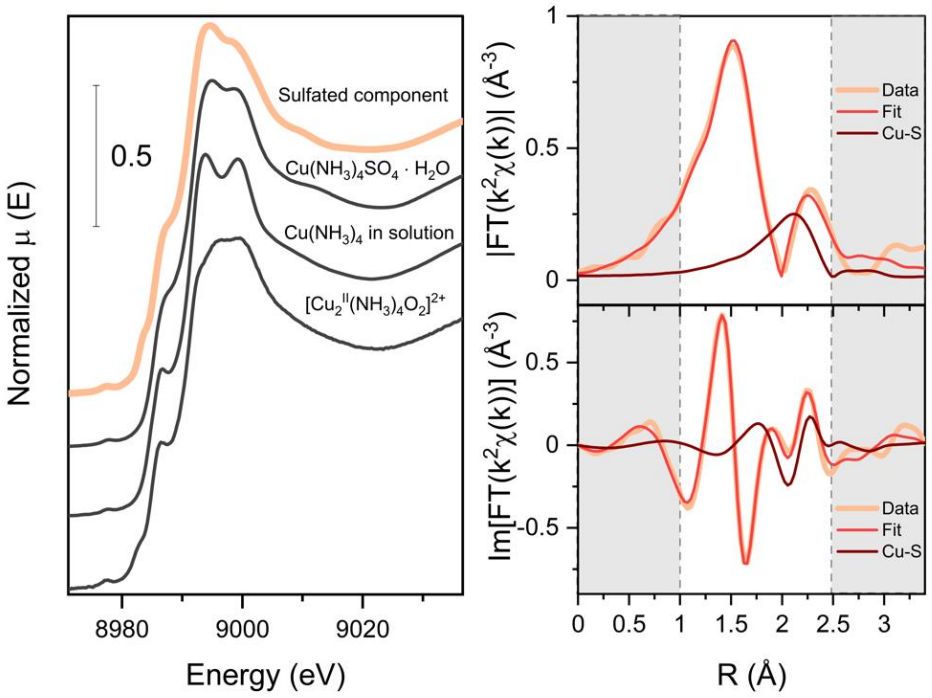

Figure 4.16. Comparison of the sulfated component obtained with MCR-ALS with the Cu K-edge XANES spectra of the $[Cu(NH_3)_4]SO_4 \cdot H_2O$, $[Cu_2^{II}(NH_3)_4O_2]^{2+}$ complex inside the CHA and $Cu^{II}_2(NH_3)_4$ in solution (left); the fitting results for the reconstructed EXAFS of the sulfated component (right). Reproduced from Molokova et al., 2023. [1]

To locate the S atoms in the "sulfated component", we extracted the EXAFS part of the sulfated component by subtracting the weighted reference spectrum for fw-Cu^{II} from the spectrum after exposure of the low-Cu catalyst to SO_2 and O_2, using the weight coefficients derived from the LCF in Section 4.6. Then EXAFS spectrum of the sulfated component was fitted with two N and two O in the first shell and S in the second shell. The fitting results are reported in Table 4.1. Figure 4.16 shows the comparison of the resulting fit with the EXAFS spectrum. Also, the contribution of the Cu-S path is highlighted. This analysis shows a Cu-S distance of 2.58 Å, which is much shorter than in the $Cu(NH_3)_4SO_4 \cdot H_2O$

reference compound (4.6 Å). This means that the structure of the sulfated component is different from $Cu(NH_3)_4SO_4 \cdot H_2O$.

Table 4.1 Results of the EXAFS fitting for sulfated component. [1]

Path	N	S_0^2	σ^2, Å^2	R, Å	E_0, eV	R-factor
Cu-O	2	0.9(1)	0.002(2)	1.94(2)	2.4	0.02
Cu-N	2		0.003(3)	2.09(2)		
Cu-S	1		0.006(2)	2.58(2)		

4.11 Unraveling the mechanism of the sulfation reaction

The final goal of this Chapter is to propose a mechanism describing the reaction of SO_2 with Cu-CHA catalysts. The results presented above contain important points crucial for understanding the mechanism.

First, sulfur XES and XANES show that S is stored in the sample as S^{6+}, most probably as SO_4^{2-} tetrahedra. This indicates an oxidation of SO_2 by the $[Cu_2^{II}(NH_3)_4O_2]^{2+}$ complex. A formation of an SO_4^{2-} group in the absence of O_2 in the gas implies the oxygen transfer from the $[Cu_2^{II}(NH_3)_4O_2]^{2+}$ complexes to the SO_2 molecule.

Second, in the reaction of SO_2 with the $[Cu_2^{II}(NH_3)_4O_2]^{2+}$ complexes in absence of O_2, the S/Cu ratio reaches only around 25 % (Figure 4.13). Nevertheless, all Cu in the catalyst changes its coordination environment, since all $[Cu_2^{II}(NH_3)_4O_2]^{2+}$ complexes are converted (Figure 4.7). The fact that all Cu in the catalyst is affected at a S/Cu uptake of 0.25, suggests that a single SO_2 molecule reacts with at least two $[Cu_2^{II}(NH_3)_4O_2]^{2+}$ complexes. This requires either sufficient mobility of the $[Cu_2^{II}(NH_3)_4O_2]^{2+}$ complexes or that first a mobile intermediate product is

formed in the reaction between SO_2 and the first complex, which then reacts with a second $[Cu_2^{II}(NH_3)_4O_2]^{2+}$. Since the mobility of the bulky $[Cu_2^{II}(NH_3)_4O_2]^{2+}$ complex is expected to be limited, the formation of a smaller mobile intermediate product seems more likely.

Bringing these considerations together, we arrive at a reaction pathway consisting of two steps. In the first step (Eq. 4.1), SO_2 reacts with a $[Cu_2^{II}(NH_3)_4O_2]^{2+}$ complex, peroxo bond breaks, a mobile SO_aX intermediate forms, and Cu^{II} reduces to Cu^{I}. The Cu^{I} appears in the form of diamino $[Cu^{I}(NH_3)_2]^{+}$ and fw-Cu^{I}, as indicated by the LCF (Figure 4.7). A possible candidate for the mobile intermediate SO_aX is SO_3, formed by oxidation of SO_2, upon the formation of Cu^{I}-species. It is known that SO_3 has similar effect on the NH_3-SCR activity of Cu-CHA as SO_2, [8, 13-15] which would be consistent with the proposed reaction scheme. However, our data do not allow to determine the exact structure of the mobile SO_aX complex, so the formation of SO_3 remains to be proven (or ruled out) experimentally.

In the second step (Eq. 4.2), the mobile SO_aX intermediate reacts with another $[Cu_2^{II}(NH_3)_4O_2]^{2+}$complex, breaking the peroxo-bond to form the $(SO_4)^{2-}$ group within the "sulfated component" ($Cu^{II}SO_4Z$) and another linear diamino complex $[Cu^{I}(NH_3)_2]^{+}$. Z in the sulfated species $Cu^{II}SO_4Z$ may comprise O, framework O or NH_3 to result in a square-planar coordination of Cu with 4-ligands proven by our EXAFS and XANES results (Figure 4.16). Such two-step reaction scheme is in line with the Cu concentration profiles obtained by the LCF analysis in the case of exposure to SO_2 in absence of O_2. Note that Equations 4.1 and 4.2 aim to summarize

the experimental findings in this article, and therefore do not represent a complete mechanism of the reaction of SO_2 with the Cu-CHA catalyst.

$$Cu_2^{II}(NH_3)_4O_2 + SO_2 \rightarrow Cu^{I}(NH_3)_2 + \text{fw-}Cu^{I} + SO_aX + \ldots \qquad (4.1)$$

$$SO_aX + Cu_2^{II}(NH_3)_4O_2 \rightarrow Cu^{I}(NH_3)_2 + Cu^{II}SO_4Z + \ldots \qquad (4.2)$$

When the sample is exposed to SO_2 in the presence of O_2, we observe an initial transient formation of the same Cu^{I} intermediates, as in case of the exposure to SO_2 alone (Figure 4.9). This indicates that O_2 reoxidizes the $[Cu^{I}(NH_3)_2]^+$ complexes into new $[Cu_2^{II}(NH_3)_4O_2]^{2+}$ complexes. In this way, the Cu^{I}-species formed in the reaction with SO_2 become available again for further reaction with SO_2. Such a reaction scheme also implies that it is possible to reactivate the Cu^{I} species formed in the reaction with SO_2 by exposing these to O_2 to form new $[Cu_2^{II}(NH_3)_4O_2]^{2+}$ complexes; a re-exposure to SO_2 should then lead to additional SO_2 uptake. This is corroborated by the results obtained with alternating exposure of the Cu-CHA catalysts to SO_2 and O_2 (Figure 4.10), showing alternating conversion of the $[Cu_2^{II}(NH_3)_4O_2]^{2+}$ complexes in the SO_2 phases and their restitution from the Cu^{I} during the exposures to O_2.

However, the exposure of the sample to alternating SO_2/O_2 cycles (Figure 4.10) also reveals that the growth of the sulfated component is not only limited to SO_2 but also occurs when the sample is exposed to O_2. Moreover, during the later stages of the cycles (3rd and 4th cycle), the growth of the sulfated component is observed only in the presence of O_2, while exposure to SO_2 alone at this stage does not lead to its formation at all. Nonetheless, even at this stage the reactive $[Cu_2^{II}(NH_3)_4O_2]^{2+}$ complexes undergo decomposition in the presence of SO_2, resulting in

sulfur adsorption on the sample surface, as further evidenced by the in situ evolution of the S/Cu ratio obtained from the XAQ signal (Figure 4.17).

A possible explanation for this effect is that at the late stages of the cycles, when the reactive Cu species are few, it is less likely to have two $[Cu_2^{II}(NH_3)_4O_2]^{2+}$ complexes close enough to perform the second step of the sulfation reaction (Eq. 4.2). Therefore, the mobile sulfur species SO_aX formed in the first step (Eq. 4.1) can be converted into the sulfated Cu species only after the stock of $[Cu_2^{II}(NH_3)_4O_2]^{2+}$ complexes is replenished upon the exposure to O_2. It is possible that in such regime SO_aX undergo further transformations (e.g. reacting with NH_3 or NH_4^+) before reacting with newly formed $[Cu_2^{II}(NH_3)_4O_2]^{2+}$ and yielding the sulfated Cu species, but the obtained data do not allow to unambiguously identify the corresponding reaction pathways. Nonetheless, the observed effect serves as indirect confirmation of the multi-step nature of sulfation process involving at least two $[Cu_2^{II}(NH_3)_4O_2]^{2+}$ complexes per SO_2.

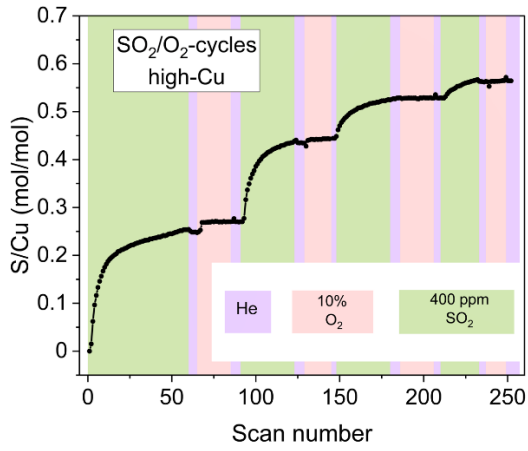

Figure 4.17. The evolution of the XAQ signal in the Procedures SO_2/O_2-cycles for the high-Cu sample (3.2 wt% Cu/CHA). Reproduced from Molokova et al., 2023. [1]

4.12 Conclusions

This Chapter investigated the interaction of the $[Cu_2^{II}(NH_3)_4O_2]^{2+}$ complexes with SO_2. In situ XAS measurements at Cu K-edge combined with XAS spectral decomposition techniques allowed us to follow the reaction and identify the reaction intermediates and reaction products. Upon reacting the $[Cu_2^{II}(NH_3)_4O_2]^{2+}$ complex with SO_2, a mixture of fw-Cu^{I} (approximately 1/4 of total Cu), $[Cu^{I}(NH_3)_2]^{+}$ complexes (approximately 1/2) and a new sulfated Cu^{II} compound (approximately 1/4) are formed. The presence of oxygen in the gas mixture with SO_2 enhances the reaction, leading to higher concentrations of the sulfated species and an increased S/Cu ratio in the sample. This effect is explained by reoxidation of the $[Cu^{I}(NH_3)_2]^{+}$ species to the reactive $[Cu_2^{II}(NH_3)_4O_2]^{2+}$ complexes. The catalysts with 0.8 wt% Cu/CHA and 3.2 wt% Cu/CHA demonstrated similar results.

Following a multi-technique experimental approach, the structure of the Cu and S local environment of sulfated species accumulated in the sample was uncovered. Copper in the sulfated species exists as Cu^{2+} and adopts a square-planar coordination with four light ligands in the first coordination shell, which, most probably, are NH_3 and O. Sulfur in the sulfated species is in the S^{6+} oxidation state, forming an SO_4 group. The sulfur atom is located in the second shell of Cu at an approximate distance of 2.6 Å, suggesting that Cu and S are connected through two oxygen ligands.

4.13 References

1. Molokova A. Yu., A. R. K., Borfecchia E., Mathon O., Bordiga S., Wen F., Berlier G., Janssens T. V.W., and Lomachenko K. A., Elucidating the reaction mechanism of SO2 with Cu-CHA catalysts for NH3-SCR by X-ray absorption spectroscopy. *Chem. Sci.* **2023 (accepted)**.

2. Martini, A.; Borfecchia, E., Spectral Decomposition of X-ray Absorption Spectroscopy Datasets: Methods and Applications. *Crystals* **2020,** *10* (8), 46.
3. Martini, A.; Borfecchia, E.; Lomachenko, K. A.; Pankin, I. A.; Negri, C.; Berlier, G.; Beato, P.; Falsig, H.; Bordiga, S.; Lamberti, C., Composition-driven Cu-speciation and reducibility in Cu-CHA zeolite catalysts: a multivariate XAS/FTIR approach to complexity. *Chem Sci* **2017,** *8* (10), 6836-6851.
4. Paolucci, C.; Khurana, I.; Parekh, A. A.; Li, S. C.; Shih, A. J.; Li, H.; Di Iorio, J. R.; Albarracin-Caballero, J. D.; Yezerets, A.; Miller, J. T.; Delgass, W. N.; Ribeiro, F. H.; Schneider, W. F.; Gounder, R., Dynamic multinuclear sites formed by mobilized copper ions in NOx selective catalytic reduction. *Science* **2017,** *357* (6354), 898-903.
5. Martini, A.; Negri, C.; Bugarin, L.; Deplano, G.; Abasabadi, R. K.; Lomachenko, K. A.; Janssens, T. V. W.; Bordiga, S.; Berlier, G.; Borfecchia, E., Assessing the Influence of Zeolite Composition on Oxygen-Bridged Diamino Dicopper(II) Complexes in Cu-CHA DeNOx Catalysts by Machine Learning-Assisted X-ray Absorption Spectroscopy. *J Phys Chem Lett* **2022,** *13* (26), 6164-6170.
6. Negri, C.; Selleri, T.; Borfecchia, E.; Martini, A.; Lomachenko, K. A.; Janssens, T. V. W.; Cutini, M.; Bordiga, S.; Berlier, G., Structure and Reactivity of Oxygen-Bridged Diamino Dicopper(II) Complexes in Cu-Ion-Exchanged Chabazite Catalyst for NH3-Mediated Selective Catalytic Reduction. *J. Am. Chem. Soc.* **2020,** *142* (37), 15884-15896.
7. Bjerregaard, J. D.; Votsmeier, M.; Grönbeck, H., Mechanism for SO2 poisoning of Cu-CHA during low temperature NH3-SCR. *J. Catal.* **2023,** *417*, 497-506.
8. Hammershoi, P. S.; Jangjou, Y.; Epling, W. S.; Jensen, A. D.; Janssens, T. V. W., Reversible and irreversible deactivation of Cu-CHA NH3-SCRcatalysts by SO2 and SO3. *Appl. Catal. B: Environ* **2018,** *226*, 38-45.
9. Hammershoi, P. S.; Jensen, A. D.; Janssens, T. V. W., Impact of SO2-poisoning over the lifetime of a Cu-CHA catalyst for NH3-SCR. *Appl. Catal. B: Environ* **2018,** *238*, 104-110.
10. Ipek, B.; Wulfers, M. J.; Kim, H.; Göltl, F.; Hermans, I.; Smith, J. P.; Booksh, K. S.; Brown, C. M.; Lobo, R. F., Formation of [Cu2O2]2+ and [Cu2O]2+ toward C–H Bond Activation in Cu-SSZ-13 and Cu-SSZ-39. *ACS Catal.* **2017,** *7* (7), 4291-4303.
11. Molokova, A. Y.; Borfecchia, E.; Martini, A.; Pankin, I. A.; Atzori, C.; Mathon, O.; Bordiga, S.; Wen, F.; Vennestrøm, P. N. R.; Berlier, G.; Janssens, T. V. W.; Lomachenko, K. A., SO2 Poisoning of Cu-CHA deNOx Catalyst: The Most Vulnerable Cu Species Identified by X-ray Absorption Spectroscopy. *JACS Au* **2022,** *2* (4), 787–792.
12. Lomachenko, K. A.; Molokova, A. Y.; Atzori, C.; Mathon, O., Quantification of Adsorbates by X-ray Absorption Spectroscopy: Getting TGA-

like Information for Free. *The Journal of Physical Chemistry C* **2022,** *126* (11), 5175–5179.
13. Cheng, Y. S.; Lambert, C.; Kim, D. H.; Kwak, J. H.; Cho, S. J.; Peden, C. H. F., The different impacts of SO2 and SO3 on Cu/zeolite SCR catalysts. *Catal. Today* **2010,** *151* (3-4), 266-270.
14. Jangjou, Y.; Wang, D.; Kumar, A.; Li, J.; Epling, W. S., SO2 Poisoning of the NH3-SCR Reaction over Cu-SAPO-34: Effect of Ammonium Sulfate versus Other S-Containing Species. *ACS Catal.* **2016,** *6* (10), 6612-6622.
15. Auvray, X.; Arvanitidou, M.; Högström, Å.; Jansson, J.; Fouladvand, S.; Olsson, L., Comparative Study of SO2 and SO2/SO3 Poisoning and Regeneration of Cu/BEA and Cu/SSZ-13 for NH3 SCR. *Emission Control Science and Technology* **2021,** *7* (4), 232-246.

5 Chemical poisoning of Cu-CHA by SO_2. How the chemistry of the reaction of $[Cu_2^{2+}(NH_3)_4O_2]^{2+}$ with NO changes upon exposure to SO_2+O_2

5.1 Introduction

Chapter 3 found that $[Cu_2^{2+}(NH_3)_4O_2]^{2+}$ is the most sensitive to SO_2 among Cu intermediates forming in Cu-CHA during the NH_3-SCR cycle.[1] $[Cu_2^{2+}(NH_3)_4O_2]^{2+}$ is also known as an important species for NH_3-SCR. [2-4] So, as we have already discussed, the reactivity of the $[Cu_2^{2+}(NH_3)_4O_2]^{2+}$ complex to SO_2 can be the key factor for the SO_2 poisoning of the Cu-CHA catalyst.

In Chapter 4, we found a possible mechanism of the interaction of the $[Cu_2^{2+}(NH_3)_4O_2]^{2+}$ complexes with SO_2 and the structure of the sulfated Cu species forming as a product of the oxidation of SO_2 by the $[Cu_2^{2+}(NH_3)_4O_2]^{2+}$ complex. We also found that the presence of O_2 enhances the sulfur uptake by the sample and the formation of the sulfated species. Moreover, the concentration of the sulfated species correlates with the S/Cu ratio, which is confirmed by two independent techniques. [5]

Based on the presented results, the current hypothesis is that the SO_2 poisoning of the Cu-CHA is caused by the reaction between the $[Cu_2^{2+}(NH_3)_4O_2]^{2+}$ complexes and SO_2 preventing the participation of the $[Cu_2^{2+}(NH_3)_4O_2]^{2+}$ complexes in the NH_3-SCR catalytic cycle and leading to accumulation of sulfated Cu species in the zeolites. However, no experimental evidence exists that SO_2 interrupts the NH_3-SCR cycle. On the contrary, in the theoretical study of Bjerregaard et al. [6], the main reason for the deactivation is proposed to be physical. Namely, the formation of

ammonium bisulfate in the catalysts cages prevents the mobility of $[Cu^{+}(NH_3)_2]^{+}$ complexes and the formation of new $[Cu_2^{2+}(NH_3)_4O_2]^{2+}$ complexes. [6-9] If the $[Cu_2^{2+}(NH_3)_4O_2]^{2+}$ complexes are not formed, the NH_3-SCR redox cycle stops. Nevertheless, while we still have $[Cu_2^{2+}(NH_3)_4O_2]^{2+}$ complexes, even in the presence of SO_2, the catalytic cycle can be completed, and the $[Cu_2^{2+}(NH_3)_4O_2]^{2+}$ complexes can interact with NO at 200 °C as before.

The authors do not exclude the formation of the sulfated Cu species. However, they attribute their formation to the minor cause of the poisoning, probably corresponding to the irreversible part of the deactivation. [6, 10] This is not yet experimentally confirmed.

Since there are sulfated Cu species, chemical poisoning may also take place. As an addition to the physical effect or as the primary poisoning mechanism.

Thus, the goal of this Chapter was to monitor the reaction between $[Cu_2^{2+}(NH_3)_4O_2]^{2+}$ complexes and NO in the fresh and SO_2-poisoned catalyst to verify if the reaction between $[Cu_2^{2+}(NH_3)_4O_2]^{2+}$ and NO changes upon SO_2 exposure. Specifically, if the kinetics of the reaction changes, indicating the Cu-CHA catalyst's chemical poisoning by SO_2.

5.2 Samples

This Chapter investigates Cu-CHA samples with 3.2 wt% Cu/CHA (high-Cu).

5.3 Experimental methods

In this chapter, we used temperature programmed reduction measurements with NO (NO-TPR) on the Cu-CHA catalyst to monitor the reaction's kinetics between the catalyst and NO. We also used in situ Cu K-edge XAS (XANES and EXAFS) for monitoring the oxidation state of the Cu during the interaction of the catalyst with SO_2 and NO; Linear Combination fitting (LCF) and Multivariate Curve Resolution Alternating least squares (MCR-ALS) analysis for identification of the Cu intermediates forming during the experiment. The outlet of the cell during the in situ XAS experiment was connected to the Mass spectrometer for monitoring the gas composition during the reaction. We also performed an in situ FTIR experiment following the same protocol as in the XAS experiment to identify better the chemical species forming in the reaction.

5.4 Experimental protocol

The NO-TPR experiment on the fresh catalyst consisted of the formation of the $[Cu_2^{2+}(NH_3)_4O_2]^{2+}$ complex described in detail in Chapter 3 Section 3.3, the cooling of the system to 50 °C and then exposure to 500 ppm of NO while heating to 550 °C with a ramp rate of 1 °C/min.

The NO-TPR experiment of the sulfated catalyst consisted of the formation of the $[Cu_2^{2+}(NH_3)_4O_2]^{2+}$ complex, the exposure to 400 ppm SO_2 for 3 hours, the cooling of the system to 50 °C and then exposure to 500 ppm of NO while heating to 550 °C with a ramp rate of 1 °C/min.

Following the results of the NO-TPR, we conducted an in situ XAS experiment at Cu K-edge and an in situ FTIR experiment using the same experimental protocols.

The experimental protocol for the fresh catalyst (Protocol (1)) included two steps after the standard pre-treatment of the catalyst at 550 °C in 10 % O_2: 1. The formation of the $[Cu_2^{2+}(NH_3)_4O_2]^{2+}$ complex and 2. The exposure of the $[Cu_2^{2+}(NH_3)_4O_2]^{2+}$ complex to NO at 200 °C. The experimental scheme of the procedure is presented in Figure 5.1.

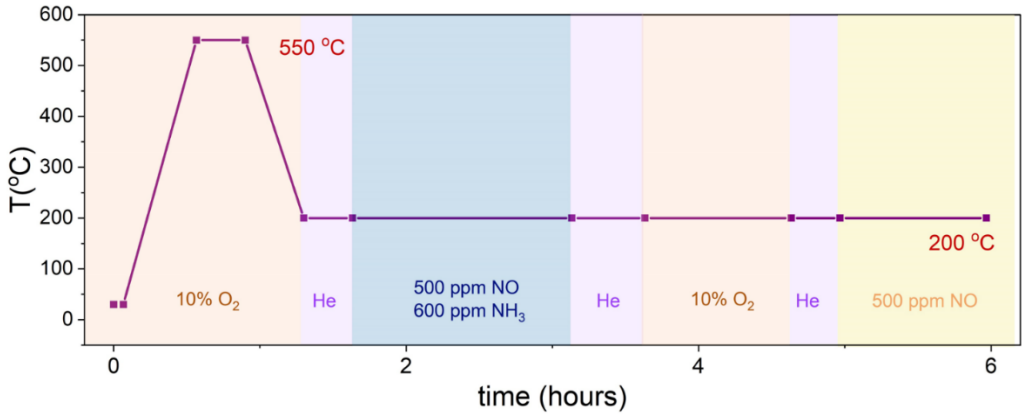

Figure 5.1 Scheme of the experimental protocol (1) of the exposure of the $[Cu^{II}_2(NH_3)_4O_2]^{2+}$ to NO at 200 °C.

The experimental protocol for the sulfated catalyst (Protocol (2)) included four steps after the standard pretreatment: 1. The formation of the $[Cu_2^{2+}(NH_3)_4O_2]^{2+}$ complex; 2. The exposure of the $[Cu_2^{2+}(NH_3)_4O_2]^{2+}$ complex to a mixture of SO_2 and O_2; 3. The exposure to NO at 200 °C, and 4. Heating to 300 °C in NO.

The experimental scheme of the procedure is presented in Figure 5.2. We chose to expose the $[Cu_2^{2+}(NH_3)_4O_2]^{2+}$ complex to a mixture of SO_2 and O_2 instead of SO_2 only because earlier in Chapter 4, we show that the mechanism of the sulfation in these two cases is similar, but in the presence

of O_2, the SO_2 uptake and the formation of the sulfated species are more efficient.

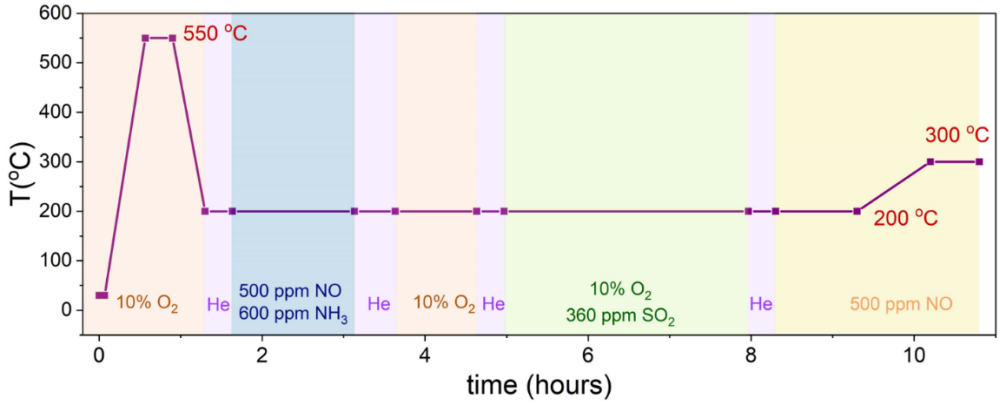

Figure 5.2 Scheme of the experimental protocol (2) of the exposure of the $[Cu^{II}_2(NH_3)_4O_2]^{2+}$ to a mixture of SO_2/O_2/He at 200 °C, to NO at 200 °C and heating to 300 °C in NO.

5.5 NO-TPR: how the kinetics of the reaction between $[Cu_2^{2+}(NH_3)_4O_2]^{2+}$ and NO changes after SO_2 poisoning

The chemical mechanism of the interaction of Cu-CHA with NO is an essential part of the SCR cycle and, consequently, a subject of many studies. [4, 11-16] In this work, we focus on the kinetics of the reaction between $[Cu_2^{2+}(NH_3)_4O_2]^{2+}$ complexes and NO for the fresh and SO_2 poisoned sample. To this aim, we carried out NO-TPR experiments, which have been proposed as a characterization technique to quantify the amount of Cu active sites in Cu-CHA.[13]

In this work, the consumption of NO by its reaction with $[Cu_2^{II}(NH_3)_4O_2]^{2+}$ complexes in the fresh 3.2 wt% Cu/CHA sample is found at 120 °C (Figure 5.3). The shift of this peak to around 250 °C for the SO_2-treated sample indicates that the chemistry of the reaction of NO has changed and that the

low temperature reaction at 200 °C is blocked. This proves that the interaction with SO_2 results in the chemical poisoning of the catalyst.

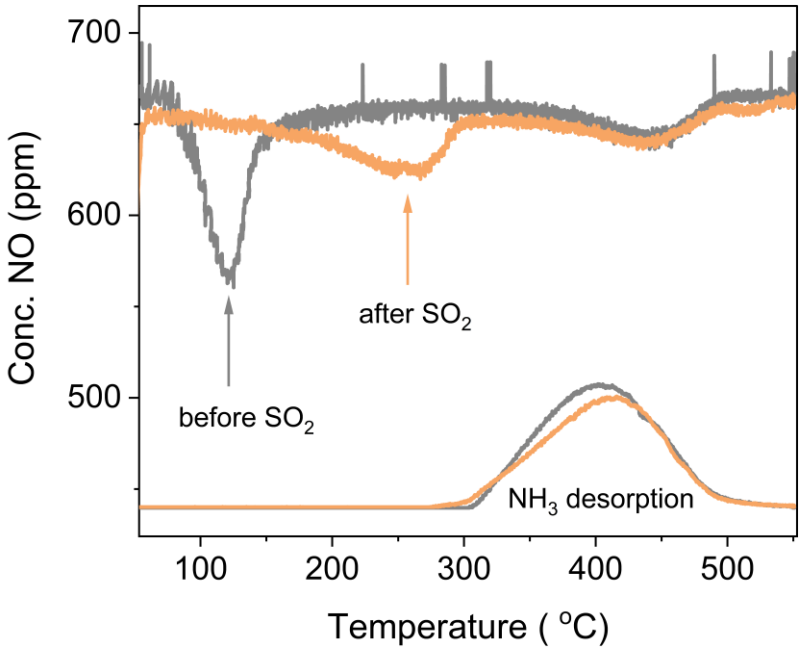

Figure 5.3. NO-TPR measurements and NH_3-TPD measurements for the fresh $[Cu_2^{2+}(NH_3)_4O_2]^{2+}$ complex and $[Cu_2^{2+}(NH_3)_4O_2]^{2+}$ complex after the exposure to SO_2.

We also monitored the desorption of NH_3 in this experiment (NH_3-TPD). The desorption of NH_3 starts at around 300 °C for both fresh and SO_2 poisoned catalyst. According to a theoretical study,[17] the peak of NH_3 desorption around 400-430 °C corresponds to the desorption of NH_3 from the Brønsted sites, that is to the decomposition of ammonium ions. In our experiments, NH_3 from ammonium ions is produced after (i.e. at a higher temperature than) the reaction between NO and the $[Cu_2^{II}(NH_3)_4O_2]^{2+}$ complexes or the sulphated ones is completed. This shows the significance of the chemical poisoning in the SO_2 poisoning of the Cu-CHA. If the poisoning was a physical effect, the reaction with NO could not be restored

until the ammonium sulfates and bisulfates preventing the mobility of the $[Cu(NH_3)_2]^+$ complexes decomposed. But according to our results in Figure 5.3, our SO_2-TPD results in Chapter 3, and to literature[18], both ammonium sulfate and bisulfate decompose only at temperatures higher than 345-350 °C.

5.6 XANES and EXAFS: monitoring the local structure of Cu upon the reaction between $[Cu_2^{2+}(NH_3)_4O_2]^{2+}$ and NO for fresh and SO_2 poisoned catalyst

Following the results of the NO consumption experiment and considering that the temperature region of interest for the low-temperature SCR is 200-350 °C, we decided to monitor the Cu oxidation state and local environment with Cu K edge XANES and EXAFS during the following two experimental protocols:

(1) Exposure of the fresh $[Cu_2^{2+}(NH_3)_4O_2]^{2+}$ to NO at 200 °C.

(2) Exposure of the fresh $[Cu_2^{2+}(NH_3)_4O_2]^{2+}$ to SO_2+O_2 at 200 °C and:

   a. Exposure to NO at 200 °C;

   b. Then heating up to 300 °C in NO.

This set of experiments allows us to monitor how the Cu oxidation state and local environment changes in the condition of the normal reaction between fresh $[Cu_2^{2+}(NH_3)_4O_2]^{2+}$ complexes and NO (1) in the state of the blocked reaction with NO due to the chemical poisoning of the catalyst (2a), and in the condition of restored reaction with NO (2b).

Figure 5.4 shows the XANES and FT-EXAFS spectra of the sample during treatments (1) and (2a,b). In protocol (1), we expose $[Cu_2^{2+}(NH_3)_4O_2]^{2+}$ species to NO. Several studies show that this reaction leads to the reduction of Cu [13, 16, 19]. This is confirmed by our XANES results on the fresh $[Cu_2^{2+}(NH_3)_4O_2]^{2+}$ complex (Figure 5.4). The weak 1s-3d transition at 8977.3 eV characteristic for Cu^{II} species disappears, while the 1s-4p transition at 8982.5 eV grows. In the EXAFS part, the intensity of the first shell decreases significantly, indicating the decomposition of the $[Cu_2^{2+}(NH_3)_4O_2]^{2+}$ complexes. The peak in the second shell broadens, which may reveal a presence of a mixture of different Cu species.

When we expose the fresh $[Cu_2^{2+}(NH_3)_4O_2]^{2+}$ complexes to a mixture of SO_2+O_2, the prevalent species is the "sulfated component", and all Cu is in a Cu^{2+} oxidation state.[5] Following the protocol, we expose the sample to NO at 200 °C (2a). There is some reduction of Cu according to the XANES results. The 1s-4p transition at 8982.5 eV is slightly growing but to a lesser extent compared to the reaction with fresh $[Cu_2^{2+}(NH_3)_4O_2]^{2+}$ complexes. In the EXAFS region the intensity of the first shell decreases, but also much less compared to the fresh sample.

Following the experimental protocol, we heat the sample to 300 °C in NO (2b). From the XANES point of view, it completes the reduction of the Cu as in the case of a fresh sample. In the EXAFS part, there is a further decrease of the first shell and a broadening of the second shell, comparable to the results for the fresh sample (1).

Overall, the XANES and EXAFS results confirm the NO consumption results. We can conclude that SO_2 poisoning blocks the reaction between

$[Cu_2^{2+}(NH_3)_4O_2]^{2+}$ complexes and NO at 200 °C, but at 300 °C, there is a reaction that results in a similar Cu oxidation state and local environment as for the fresh sample.

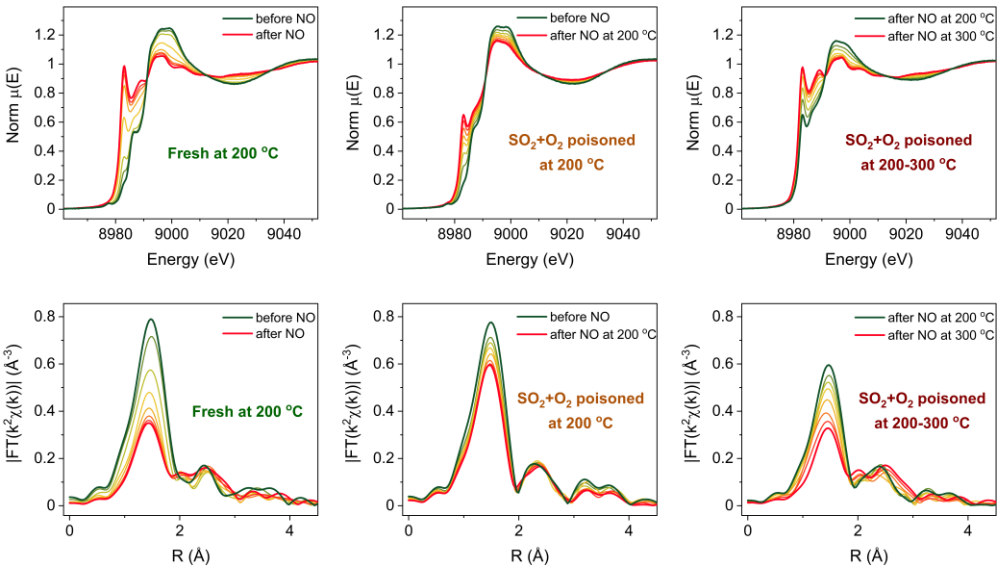

Figure 5.4. Cu K-edge XANES (top panel) and FT-EXAFS spectra (bottom panel) collected in situ during the exposure of fresh $[Cu_2^{2+}(NH_3)_4O_2]^{2+}$ species to NO at 200 °C (left), SO_2+O_2 poisoned $[Cu_2^{2+}(NH_3)_4O_2]^{2+}$ species to NO at 200 °C (middle), and SO_2+O_2 poisoned $[Cu_2^{2+}(NH_3)_4O_2]^{2+}$ species to NO at 200-300 °C (right).

To monitor the changes in XANES during the experimental protocols and resolve the forming species, we performed a combined MCR-ALS and LCF study, as was done in Chapter 4. This allowed us to obtain the evolution of the species during the procedures. As components for the LCF as in Chapter 4, we took experimental spectra of fw-Cu^{II}, $[Cu_2^{2+}(NH_3)_4O_2]^{2+}$ and $[Cu^{+}(NH_3)_2]^{+}$, and MCR-generated spectra of fw-Cu^{I} and the sulfated component (Figure 5.5).

In protocol (1), all the pre-treatment stages of the procedure aimed to prepare $[Cu_2^{2+}(NH_3)_4O_2]^{2+}$ complexes, and the final spectrum of the complex correspond to the previous results. The result of the interaction of the fresh dimer with NO is a mixture of fw-Cu^{I} and $[Cu^{+}(NH_3)_2]^{+}$ (Figure 5.6). So, the final oxidation state of Cu is indeed Cu^{I}.

In protocol (2a,b) we prepare the $[Cu_2^{2+}(NH_3)_4O_2]^{2+}$ complexes and expose them to SO_2+O_2. The resulting spectrum is a mixture of the sulfated component, fw-Cu^{II}, and $[Cu_2^{2+}(NH_3)_4O_2]^{2+}$ complexes, also described in detail in Chapter 4.

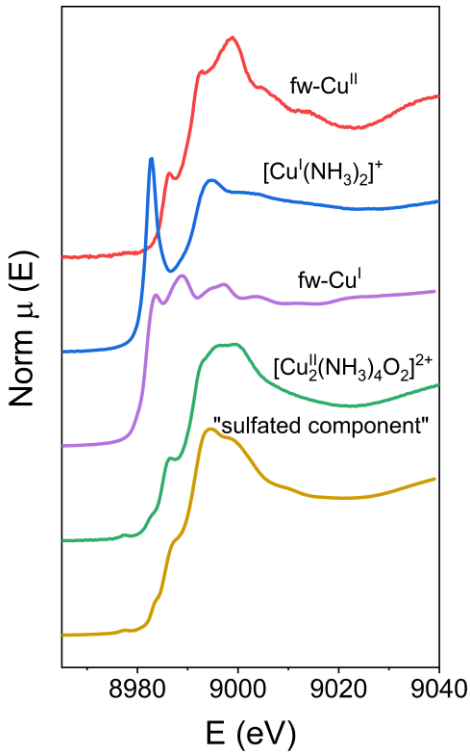

Figure 5.5. Spectra used as references in the linear combination fit. The spectra of fw-Cu^{II}, $[Cu^{I}(NH_3)_2]^{+}$, and $[Cu_2^{II}(NH_3)_4O_2]^{2+}$ are experimental spectra. The spectra of fw-Cu^{I} and the "sulfated component" were obtained with MCR-ALS.

Following protocol (2a) we expose the SO_2+O_2 poisoned $[Cu_2^{2+}(NH_3)_4O_2]^{2+}$ complexes to NO at 200 °C. The concentration of the sulfated component is decreasing, and the concentrations of the fw-Cu^I and $[Cu^+(NH_3)_2]^+$ are going up. Fw-Cu^{II} is not affected at all by the presence of NO, and the concentration of the $[Cu_2^{2+}(NH_3)_4O_2]^{2+}$ complexes decreases.

When we start heating the system to 300 °C (2b), the concentrations of the sulfated component, fw-Cu^{II}, and $[Cu_2^{2+}(NH_3)_4O_2]^{2+}$ complexes quickly go to zero. The fw-Cu^I and $[Cu^+(NH_3)_2]^+$ concentrations go up and stabilize.

Upon heating the system to 300 °C, we observe the formation of the same reaction products as those obtained for the fresh sample at 200 °C, although with a slightly different ratio between the components. Namely, the concentration of $[Cu^+(NH_3)_2]^+$ is 12-15 % lower. Less species with NH_3 form, probably because some NH_3 was likely lost from the sample during the exposure to SO_2+O_2. The formation of around 15 % of ammonium-free fw-Cu^{II} during exposure to SO_2+O_2 aligns with this hypothesis.

Based on the findings obtained through LCF analysis, it is evident that the restoration of the $[Cu_2^{2+}(NH_3)_4O_2]^{2+}$ complexes does not occur. Consequently, the heating process does not involve the transformation of the sulfated species to the $[Cu_2^{2+}(NH_3)_4O_2]^{2+}$ complexes capable of reacting with NO. Instead, the sulfated species themselves react with NO. And higher temperatures are necessary for the sulfated species to react with NO.

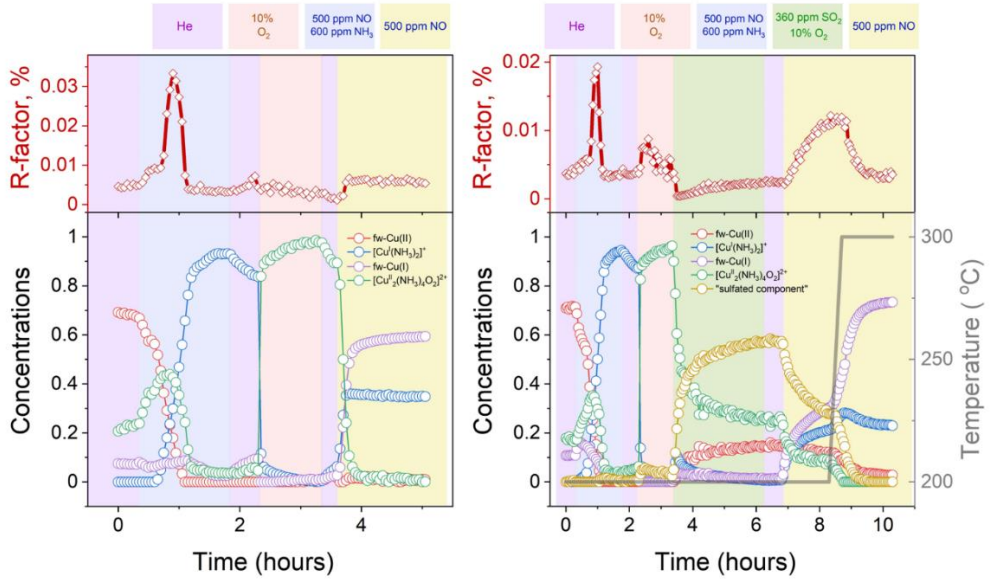

Figure 5.6. Linear combination fit results for the experimental procedures. Left – exposure of the $[Cu_2^{2+}(NH_3)_4O_2]^{2+}$ to NO at 200 °C; Right – exposure of the $[Cu_2^{2+}(NH_3)_4O_2]^{2+}$ to SO_2+O_2, then to NO at 200°C, and then to NO at 200-300 °C. Upper panels – R-factors of the fit as a function of time, lower panels – concentration profiles of the reference spectra as a function of time.

5.7 Mass spectrometry results

We monitored the outlet gas composition with a mass spectrometer during the XAS experiment. The results also provide valuable insights into the reaction of the fresh and SO_2-poisoned $[Cu_2^{2+}(NH_3)_4O_2]^{2+}$ complexes with NO.

In the case of the fresh $[Cu_2^{2+}(NH_3)_4O_2]^{2+}$ complexes exposed to NO (Protocol (1)), when we introduce NO to the system, we immediately see NO consumption and production of N_2 and H_2O (Figure 5.7 left panel).

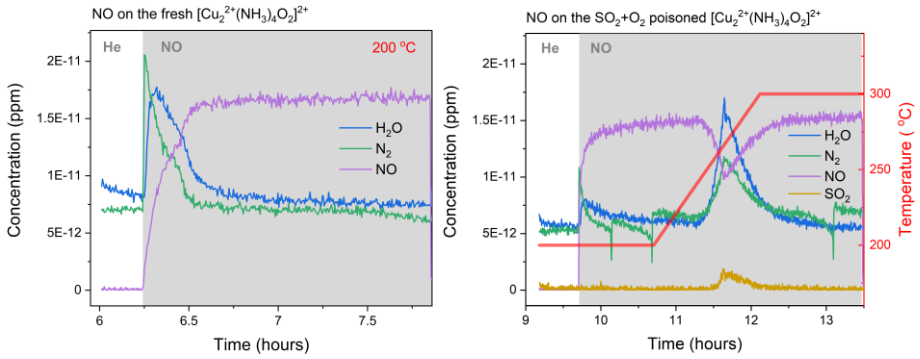

Figure 5.7. Mass spectrometer data during the exposure of fresh (left panel) and SO_2 poisoned (right panel) $[Cu_2^{2+}(NH_3)_4O_2]^{2+}$ complexes to NO.

In the case of the poisoned $[Cu_2^{2+}(NH_3)_4O_2]^{2+}$ complexes (Protocol (2a,b)), the main peak of the NO consumption and the production of N_2 and H_2O is shifted to a higher temperature, around 250 °C (Figure 5.7 right panel). This is in line with our previous investigations. There is desorption of SO_2, corresponding to the decomposition of the sulfated species visible on LCF results. This occurs at the same temperature of N_2 and H_2O evolution, confirming the hypothesis that NO is reacting with the sulphated component.

In the case of the poisoned $[Cu_2^{2+}(NH_3)_4O_2]^{2+}$ complexes, we also observed some NO consumption and production of N_2 and H_2O at the beginning of the exposure to NO at 200 °C, although significantly lower than for the fresh sample. This suggests that some of the $[Cu_2^{2+}(NH_3)_4O_2]^{2+}$ complexes that did not react with SO_2, according to LCF results, retained their ability to react with NO. One possibility is that the portion of $[Cu_2^{2+}(NH_3)_4O_2]^{2+}$ complexes previously referred to as "unreactive" in Chapter 4 actually correspond to $[Cu_2^{2+}(NH_3)_4O_2]^{2+}$ complexes able to react with NO.

Since the reaction of the Cu-CHA catalyst with NO can be restored by heating it to 300 °C, the effect of forming the sulfated Cu species also corresponds to the reversible part of the deactivation. This means that the reversible part of the deactivation consists of two processes: the restoration of the reaction with NO at 300 °C and the decomposition of the ammonium bisulfate at 400 °C.

5.8 FTIR results

The in situ FTIR experiments followed the same protocols as in situ XAS experiments.

Figure 5.8 presents the FTIR spectra of the $[Cu_2^{II}(NH_3)_4O_2]^{2+}$ exposed to NO at 200 °C (Protocol (1)); $[Cu_2^{II}(NH_3)_4O_2]^{2+}$ exposed to SO_2/O_2/He at 200 °C, then to NO at 200 °C, and then to NO at 300 °C (Protocol (2)). The $[Cu_2^{2+}(NH_3)_4O_2]^{2+}$ spectrum is subtracted in all four spectra to identify the spectral features better. The $[Cu_2^{2+}(NH_3)_4O_2]^{2+}$ and fw-Cu^{II} spectra are presented in Figure 5.9 as reference spectra.

When we expose the $[Cu_2^{2+}(NH_3)_4O_2]^{2+}$ complexes in the fresh Cu-CHA catalyst to NO (Protocol (1)), the OH stretching mode (ν OH) of Brønsted sites [20, 21] in the region 3530-3630 cm^{-1} grows, and the broad and complex absorption related to νOH of NH_3 and NH_4^+ (2500-3500 cm^{-1}) goes down [20, 22, 23]. See Figure 5.8. The corresponding bending modes of NH_3 and NH_4^+ (1620 and 1439 cm^{-1}) also go down. This indicates the consumption of NH_3 from $[Cu_2^{2+}(NH_3)_4O_2]^{2+}$ complexes and of NH_4^+ from the Brønsted sites, which are restored. This is an interesting result, since it indicates an involvement of the NH_3 stored as NH_4^+ at the framework negative charges of the zeolites.

The consumption of the NH_3 and NH_4^+ from the Brønsted sites in the presence of NO at 200 °C does not agree with the interpretation of the NH_3 desorption presented in Section 5.5. Another interpretation of the NH_3 desorption peak in Figure 5.3 is the desorption of NH_3 from $[Cu^I(NH_3)_2]^+$ complexes. [17, 24] This interpretation fits better with FTIR results and with XANES results demonstrating the formation of the $[Cu^I(NH_3)_2]^+$ complexes upon exposure of the $[Cu_2^{II}(NH_3)_4O_2]^{2+}$ to NO.

In the following Protocol (2), $[Cu_2^{2+}(NH_3)_4O_2]^{2+}$ complexes are exposed to SO_2+O_2, and the signal of the Brønsted sites (3530-3630 cm^{-1}) stays unchanged. See the purple line in Figure 5.8. However, the NH_4^+ (1439 cm^{-1} and broad positive band between 3150 and 2720 cm^{-1}) is growing, while NH_3 adsorbed on Cu ions decreases (negative band at 1620 cm^{-1}). According to the results shown in Chapter 4, when the $[Cu_2^{2+}(NH_3)_4O_2]^{2+}$ complexes are exposed to SO_2+O_2, around 15 % of Cu forms fw-Cu^{II}, so some NH_3 can be released. The interpretation of the growth of NH_4^+ during the reaction with SO_2+O_2 is not straightforward. One could argue that the released NH_3 molecules are protonated by Brønsted sites forming ammonium, but no changes are observed in the Brønsted region. Another possibility could be the formation of ammonium sulphate or bisulfate, predicted by DFT calculations.

After the exposure to SO_2+O_2, the Cu-CHA catalyst is exposed to NO at 200 °C (red line in Figure 5.8). This causes a decrease of the NH_4^+ formed during the reaction with SO_2+O_2, a decrease of adsorbed NH_3 and a restoration of the Brønsted sites. This is similar to what observed by reaction of NO with the $[Cu_2^{2+}(NH_3)_4O_2]^{2+}$ complexes. However, at 200

°C it was impossible to reach the state of the fresh $[Cu_2^{2+}(NH_3)_4O_2]^{2+}$ complexes reacting with NO (light-blue line in Figure 5.8).

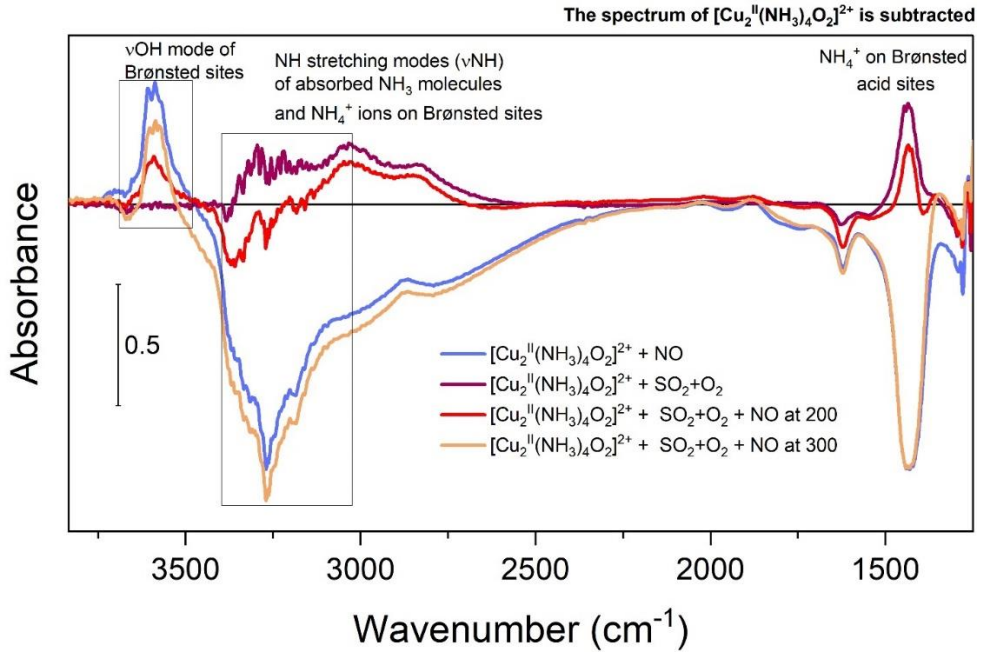

Figure 5.8 in situ FTIR spectra of Cu-CHA catalyst during exposure of the $[Cu_2^{2+}(NH_3)_4O_2]^{2+}$ complexes to NO at 200 °C, a mixture of SO_2/O_2/He and NO at 200 °C, NO after heating to 300 °C. The initial spectrum of the $[Cu_2^{2+}(NH_3)_4O_2]^{2+}$ is subtracted.

The heating of the Cu-CHA catalyst to 300 °C in NO results in the complete release of NH_3 and NH_4^+ from the Brønsted sites, reaching a final state (orange line in Figure 5.8) comparable to the state of the $[Cu_2^{2+}(NH_3)_4O_2]^{2+}$ complexes reacting with NO in the fresh catalyst (light-blue line in Figure 5.8). The signal of the Brønsted sites does not completely reach the level of the fresh catalyst. It is noteworthy that the consumption of NH_4^+ groups in this step is not in agreement with its assignment to ammonium sulphate or bisulphate, since these are expected to decompose at higher temperature (345-350 °C and higher).

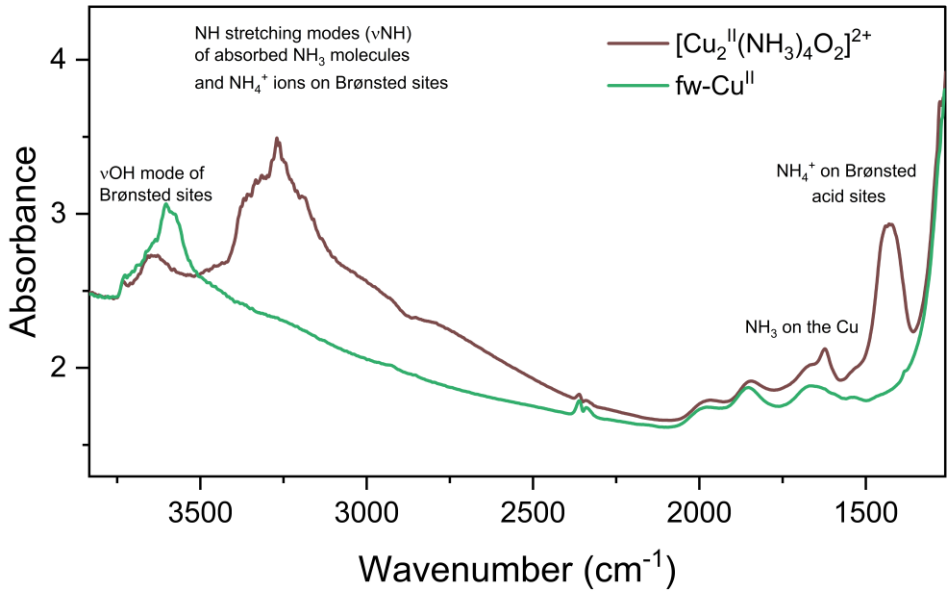

Figure 5.9 in situ FTIR spectra of the $[Cu_2^{2+}(NH_3)_4O_2]^{2+}$ complex and fw-Cu^{II} species in Cu-CHA catalyst.

These results confirm that restoring the reaction between the sulfated catalyst and NO is possible by heating the system to 300 °C. However, the observed changes in the region of NH_4^+ suggests a complexity in the mechanism that still needs to be understood.

5.9 Conclusions

This Chapter investigates the reaction between the $[Cu_2^{2+}(NH_3)_4O_2]^{2+}$ complexes in the fresh and sulfated Cu-CHA catalyst. The NO-TPR results reveal significant changes in the reaction kinetics between Cu-CHA and NO upon exposure to SO_2. This indicates that the exposure of the Cu-CHA catalyst to SO_2 causes chemical poisoning at low temperatures (200 °C). It is possible to restore the reaction with NO by heating the catalyst to 300 °C. The in situ Cu K-edge XAS and in situ FTIR spectroscopy confirm the result. The analysis of the outlet gas during the in situ XAS experiment

also confirms that the exposure of the Cu-CHA catalyst to SO_2 or SO_2/O_2 blocks the reaction between Cu-CHA and NO at 200 °C, and the heating to 300 °C restores the reaction. While these findings do not exclude the potential influence of physical poisoning by SO_2 on Cu-CHA, they emphasize the significant role of chemical poisoning in the reversible deactivation of the Cu-CHA catalyst.

5.10 References

1. Molokova, A. Y.; Borfecchia, E.; Martini, A.; Pankin, I. A.; Atzori, C.; Mathon, O.; Bordiga, S.; Wen, F.; Vennestrøm, P. N. R.; Berlier, G.; Janssens, T. V. W.; Lomachenko, K. A., SO2 Poisoning of Cu-CHA deNOx Catalyst: The Most Vulnerable Cu Species Identified by X-ray Absorption Spectroscopy. *JACS Au* **2022,** *2* (4), 787–792.
2. Paolucci, C.; Di Iorio, J. R.; Schneider, W. F.; Gounder, R., Solvation and Mobilization of Copper Active Sites in Zeolites by Ammonia: Consequences for the Catalytic Reduction of Nitrogen Oxides. *Acc Chem Res* **2020,** *53* (9), 1881-1892.
3. Paolucci, C.; Khurana, I.; Parekh, A. A.; Li, S. C.; Shih, A. J.; Li, H.; Di Iorio, J. R.; Albarracin-Caballero, J. D.; Yezerets, A.; Miller, J. T.; Delgass, W. N.; Ribeiro, F. H.; Schneider, W. F.; Gounder, R., Dynamic multinuclear sites formed by mobilized copper ions in NOx selective catalytic reduction. *Science* **2017,** *357* (6354), 898-903.
4. Feng, Y.; Wang, X.; Janssens, T. V. W.; Vennestrøm, P. N. R.; Jansson, J.; Skoglundh, M.; Grönbeck, H., First-Principles Microkinetic Model for Low-Temperature NH3-Assisted Selective Catalytic Reduction of NO over Cu-CHA. *ACS Catal.* **2021**, 14395-14407.
5. Molokova A. Yu., A. R. K., Borfecchia E., Mathon O., Bordiga S., Wen F., Berlier G., Janssens T. V.W., and Lomachenko K. A., Elucidating the reaction mechanism of SO2 with Cu-CHA catalysts for NH3-SCR by X-ray absorption spectroscopy. *Chem. Sci.* **2023 (accepted)**.
6. Bjerregaard, J. D.; Votsmeier, M.; Grönbeck, H., Mechanism for SO2 poisoning of Cu-CHA during low temperature NH3-SCR. *J. Catal.* **2023,** *417*, 497-506.
7. Jangjou, Y.; Do, Q.; Gu, Y. T.; Lim, L. G.; Sun, H.; Wang, D.; Kumar, A.; Li, J. H.; Grabow, L. C.; Epling, W. S., Nature of Cu Active Centers in Cu-SSZ-13 and Their Responses to SO2 Exposure. *ACS Catal.* **2018,** *8* (2), 1325-1337.

8. Wijayanti, K.; Xie, K.; Kumar, A.; Kamasamudram, K.; Olsson, L., Effect of gas compositions on SO2 poisoning over Cu/SSZ-13 used for NH3-SCR. *Applied Catalysis B: Environmental* **2017,** *219*, 142-154.
9. Jangjou, Y.; Wang, D.; Kumar, A.; Li, J.; Epling, W. S., SO2 Poisoning of the NH3-SCR Reaction over Cu-SAPO-34: Effect of Ammonium Sulfate versus Other S-Containing Species. *ACS Catal.* **2016,** *6* (10), 6612-6622.
10. Hammershoi, P. S.; Jangjou, Y.; Epling, W. S.; Jensen, A. D.; Janssens, T. V. W., Reversible and irreversible deactivation of Cu-CHA NH3-SCR catalysts by SO2 and SO3. *Appl. Catal. B: Environ* **2018,** *226*, 38-45.
11. Chen, L.; Janssens, T. V. W.; Vennestrom, P. N. R.; Jansson, J.; Skoglundh, M.; Gronbeck, H., A Complete Multisite Reaction Mechanism for Low-Temperature NH3-SCR over Cu-CHA. *ACS Catal.* **2020,** *10* (10), 5646-5656.
12. Daya, R.; Trandal, D.; Menon, U.; Deka, D. J.; Partridge, W. P.; Joshi, S. Y., Kinetic Model for the Reduction of CuII Sites by NO + NH3 and Reoxidation of NH3-Solvated CuI Sites by O2 and NO in Cu-SSZ-13. *ACS Catal.* **2022**, 6418-6433.
13. Hammershøi, P. S.; Negri, C.; Berlier, G.; Bordiga, S.; Beato, P.; Janssens, T. V. W., Temperature-programmed reduction with NO as a characterization of active Cu in Cu-CHA catalysts for NH3-SCR. *Catal. Sci. Technol.* **2019,** *9* (10), 2608-2619.
14. Janssens, T. V. W.; Falsig, H.; Lundegaard, L. F.; Vennestrom, P. N. R.; Rasmussen, S. B.; Moses, P. G.; Giordanino, F.; Borfecchia, E.; Lomachenko, K. A.; Lamberti, C.; Bordiga, S.; Godiksen, A.; Mossin, S.; Beato, P., A Consistent Reaction Scheme for the Selective Catalytic Reduction of Nitrogen Oxides with Ammonia. *ACS Catal.* **2015,** *5* (5), 2832-2845.
15. Mesilov, V.; Pon, L.; Dahlin, S.; Bergman, S. L.; Pettersson, L. J.; Bernasek, S. L., Computational Study of Noble Metal CHA Zeolites: NO Adsorption and Sulfur Resistance. *The Journal of Physical Chemistry C* **2022**.
16. Negri, C.; Selleri, T.; Borfecchia, E.; Martini, A.; Lomachenko, K. A.; Janssens, T. V. W.; Cutini, M.; Bordiga, S.; Berlier, G., Structure and Reactivity of Oxygen-Bridged Diamino Dicopper(II) Complexes in Cu-Ion-Exchanged Chabazite Catalyst for NH3-Mediated Selective Catalytic Reduction. *J. Am. Chem. Soc.* **2020,** *142* (37), 15884-15896.
17. Chen, L.; Janssens, T. V. W.; Skoglundh, M.; Grönbeck, H., Interpretation of NH3-TPD Profiles from Cu-CHA Using First-Principles Calculations. *Topics in Catalysis* **2018,** *62* (1-4), 93-99.
18. Zhou, C.; Zhang, L.; Deng, Y.; Ma, S.-C., Research progress on ammonium bisulfate formation and control in the process of selective catalytic reduction. *Environmental Progress & Sustainable Energy* **2016,** *35* (6), 1664-1672.
19. Negri, C.; Borfecchia, E.; Martini, A.; Deplano, G.; Lomachenko, K. A.; Janssens, T. V. W.; Berlier, G.; Bordiga, S., In situ X-ray absorption study of Cu

species in Cu-CHA catalysts for NH3-SCR during temperature-programmed reduction in NO/NH3. *Research on Chemical Intermediates* **2021,** *47* (1), 357-375.
20. Negri, C.; Borfecchia, E.; Cutini, M.; Lomachenko, K. A.; Janssens, T. V. W.; Berlier, G.; Bordiga, S., Evidence of Mixed-Ligand Complexes in Cu−CHA by Reaction of Cu Nitrates with NO/NH3 at Low Temperature. *ChemCatChem* **2019,** *11* (16), 3828-3838.
21. Vimont, A.; Thibault-Starzyk, F.; Daturi, M., Analysing and understanding the active site by IR spectroscopy. *Chem Soc Rev* **2010,** *39* (12), 4928-50.
22. Giordanino, F.; Borfecchia, E.; Lomachenko, K. A.; Lazzarini, A.; Agostini, G.; Gallo, E.; Soldatov, A. V.; Beato, P.; Bordiga, S.; Lamberti, C., Interaction of NH3 with Cu-SSZ-13 Catalyst: A Complementary FTIR, XANES, and XES Study. *J. Phys. Chem. Lett.* **2014,** *5* (9), 1552-1559.
23. A. Zecchina, L. M., * S. Bordiga, C. Paze`, and E. Gianotti, Vibrational Spectroscopy of NH4+ Ions in Zeolitic Materials: An IR Study. *J. Phys. Chem. B* **1997,** *101*, 10128-10135.

24. Borfecchia, E.; Negri, C.; Lomachenko, K. A.; Lamberti, C.; Janssens, T. V. W.; Berlier, G., Temperature-dependent dynamics of NH3-derived Cu species in the Cu-CHA SCR catalyst. *React Chem Eng* **2019,** *4* (6), 1067-1080.

6 Summary and conclusions

The main objective of this work was the investigation of the SO_2 poisoning of the Cu-CHA deNO_x catalyst.

First, the most SO_2 reactive Cu species were identified using in situ XAS at Cu K-edge. Since in the NH_3-SCR redox cycle, Cu atoms change the oxidation state and local environment, it was essential to investigate the impact of SO_2 on different Cu species. Among Cu intermediates forming during the NH_3-SCR catalytic cycle, the $[Cu_2^{II}(NH_3)_4O_2]^{2+}$ complex was the most reactive to SO_2. Before, $[Cu_2^{II}(NH_3)_4O_2]^{2+}$ was proved to be the key intermediate of the NH_3-SCR redox cycle, directly participating in NO reduction. Consequently, the reactivity of the $[Cu_2^{II}(NH_3)_4O_2]^{2+}$ complex can be the main reason for the poisoning of the Cu-CHA by SO_2 and the interruption of the NH_3-SCR catalytic cycle.

Second, the vulnerability of the $[Cu_2^{II}(NH_3)_4O_2]^{2+}$ complex was also confirmed by estimating the SO_2 uptake by the Cu-CHA catalyst using the SO_2-TPD and a new method, XAQ. XAQ was developed during one of the project's experiments and made it possible to monitor the S/Cu ratio in the sample in situ during the XAS experiment. XAQ and SO_2-TPD also showed that the presence of O_2 enhances the reaction between the $[Cu_2^{II}(NH_3)_4O_2]^{2+}$ and SO_2 by oxidizing Cu^I species into the reactive $[Cu_2^{II}(NH_3)_4O_2]^{2+}$ complexes.

Third, a combination of experimental and data analysis techniques allowed us to identify the intermediates and products of the reaction between the $[Cu_2^{II}(NH_3)_4O_2]^{2+}$ complex and SO_2, propose a mechanism of the reaction, and resolve the structure of the sulfated Cu species. The multi-technique

approach included in situ XAS at Cu K-edge, in situ XAS at S K-edge, S Kα XES, MCR-ALS method, LCF, and EXAFS fitting.

Finally, it was shown that exposure to SO_2 causes chemical poisoning of the Cu-CHA catalyst. NO-TPR measurements demonstrated that the kinetics of the reaction of the Cu-CHA with NO changes upon exposure to SO_2. The in situ XAS, in situ FTIR, and mass-spectrometry measurements confirmed that the reaction between the Cu-CHA and NO was blocked at 200 °C and shifted to higher temperatures. These results did not exclude the effect of physical poisoning. However, the importance of the chemical poisoning and the formation of the sulfated Cu species was proven.

In conclusion, the study provided insights important for understanding the SO_2 poisoning of the Cu-CHA catalyst. Concerning the future perspectives, verifying the presented results under Operando conditions in the SCR gas mixture (NH_3, NO, O_2, H_2O) would be interesting. It would be helpful to monitor the formation of the sulfated Cu species in the presence of SO_2 in the SCR gas and to verify the correlation of the concentration of the sulfated species with the loss in activity. A better understanding of the SO_2 poisoning mechanism can help to find solutions for dealing with the deactivation without replacing the catalyst and to make the air cleaner.

7 Report on PhD activities

7.1 Publications

1. SO_2 Poisoning of Cu-CHA deNO_x Catalyst: The Most Vulnerable Cu Species Identified by X-ray Absorption Spectroscopy. Anastasia Yu. Molokova, Elisa Borfecchia, Andrea Martini, Ilia A. Pankin, Cesare Atzori, Olivier Mathon, Silvia Bordiga, Fei Wen, Peter N. R. Vennestrøm, Gloria Berlier, Ton V. W. Janssens, and Kirill A. Lomachenko. *JACS Au* **2022** *2* (4), 787-792. DOI: 10.1021/jacsau.2c00053

2. Quantification of Adsorbates by X-ray Absorption Spectroscopy: Getting TGA-like Information for Free. Kirill A. Lomachenko, Anastasia Yu. Molokova, Cesare Atzori, and Olivier Mathon. *The Journal of Physical Chemistry C* **2022** *126* (11), 5175-5179. DOI: 10.1021/acs.jpcc.2c00226

3. Elucidating the reaction mechanism of SO_2 with Cu-CHA catalysts for NH_3-SCR by X-ray absorption spectroscopy. Anastasia Yu. Molokova, Reza K. Abasabadi, Elisa Borfecchia, Olivier Mathon, Silvia Bordiga, Fei Wen, Gloria Berlier, Ton V.W. Janssens and Kirill A. Lomachenko. *Chemical Science* **2023 (accepted)**

7.2 Conferences

* - personally attended the conference

int. – international conference, nat. – national conference

[*, int, poster] **A. Yu. Molokova**, O. Mathon, G. Berlier, E. Borfecchia, S. Bordiga, T.V.W.Janssens, F. Wen, P.N.R. Vennestrøm, K.A. Lomachenko. Investigation of Cu-zeolite-based industrial deNOx catalyst by means of X-ray absorption spectroscopy. 26.02.2021, Hercules 2021 Poster Session, online.

[*, nat, poster] **A. Yu. Molokova**, G. Berlier, E. Borfecchia, S. Bordiga, T.V.W. Janssens, O. Mathon, P.N.R. Vennestrøm, F. Wen, K.A. Lomachenko. Monitoring sulphur poisoning of Cu-CHA deNOx catalysts by X-ray absorption spectroscopy. 21-23.06.2021, SILS 2021, online.

[*, int, oral] **A.Yu. Molokova**, G. Berlier, E. Borfecchia, T.V.W. Janssens, S. Bordiga, F. Wen, P.N.R. Vennestrøm, K.A. Lomachenko "Cu-CHA deNOx catalyst: Sulfur poisoning monitored by X-ray absorption spectroscopy" 6-8.06.2022, Nordic symposium on catalysis, Espoo, Finland.

[*, int, oral] **A.Yu. Molokova**, G. Berlier, E. Borfecchia, T.V.W. Janssens, S. Bordiga, F. Wen, P.N.R. Vennestrøm, K.A. Lomachenko "Observation of sulphur poisoning of Cu-CHA deNOx catalysts by X-ray absorption spectroscopy" 27-30.06.2022, ISHHC19, Oslo (online).

[*, int, oral+poster] **A.Yu. Molokova**, G. Berlier, E. Borfecchia, C. Atzori, O. Mathon, S. Bordiga, F. Wen, P.N.R.Vennestrøm, T.V.W. Janssens, K.A. Lomachenko "Monitoring the SO_2 poisoning of Cu-CHA deNOx catalysts by X-ray absorption spectroscopy" 06-07.07. 2022, InnovaXN Plenary event, European Photon and Neutron (EPN) Campus Grenoble – France.

[*, int, poster] **A.Yu. Molokova,** G. Berlier, E. Borfecchia, C. Atzori, O. Mathon, S. Bordiga, F. Wen, P.N.R.Vennestrøm, T.V.W. Janssens, K.A. Lomachenko, The mechanism of the SO_2 poisoning of the Cu-CHA $deNO_x$ catalyst, 04.06.2023, InnovaXN Plenary Event, Grenoble, France.

[*, int, poster] **A.Yu. Molokova**, G. Berlier, E. Borfecchia, T.V.W. Janssens, S. Bordiga, F. Wen, P.N.R. Vennestrøm, K.A. Lomachenko, SO_2 poisoning of Cu-CHA $deNO_x$ catalyst monitored by X-ray spectroscopy, 06-08.02.2023, ESRF Users Meeting 2023, Grenoble, France.

[*, int, poster] **A.Yu. Molokova**, G. Berlier, E. Borfecchia, T.V.W. Janssens, S. Bordiga, F. Wen, P.N.R. Vennestrøm, K.A. Lomachenko, SO_2 poisoning of the Cu-CHA deNO_x catalyst monitored by X-ray absorption spectroscopy, 27.08-01.09.2023, Europacat 2023, Prague, Czech Republic.

[int, poster] R. K. Abasabadi, A. Y. Molokova, K. A. Lomachenko, P. N. R. Vennestrøm, F. Wen, T. V. W. Janssens, S. Bordiga, E. Borfecchia, G. Berlier, Effect of the Si/Al ratio on SO_2 poisoning of Cu-CHA zeolites studied by in situ DR UV-Vis spectroscopy and deactivation measurements, 7-11.05.2023, Operando VII, Grindelwald, Switzerland

[int, oral] R. K. Abasabadi, A. Y. Molokova, K. A. Lomachenko, P. N. R. Vennestrøm, F. Wen, T. V. W. Janssens, S. Bordiga, E. Borfecchia, G. Berlier, Following SO_2 poisoning of Cu^+ and Cu^{2+} on CHA zeolites for the NH_3-SCR reaction: an in situ UV-Vis study, 3-8.07.2022, IZC2022, Valencia, Spain

7.3 Schools

XAS/XES School 2021 on Advanced Synchrotron Methods: X-ray Absorption and Emission spectroscopy, Moscow, Russia (online), 02-04 June 2021

HERCULES 2021: Higher European Research Course for Users of Large Experimental Systems, online, from 22 February to 26 March 2021 (5 weeks)

InnovaXN School of Innovation and Entrepreneurship (Grenoble, France) 15-18 November 2022

8 Acknowledgements

I am deeply grateful to the individuals and institutions whose support, guidance, and encouragement have been essential in the successful completion of this PhD journey.

First, I would like to thank my supervisors, Dr. Kirill Lomachenko, Prof. Gloria Berlier, and Dr. Ton V.W. Janssens, for their constant support, deep knowledge and wisdom, and active participation in every aspect of the project. Working with you has been incredible!

I want to thank Dr. Elisa Borfecchia, Prof. Silvia Bordiga, Dr. Fei Wen, Reza K. Abasabadi, Dr. Peter N.R. Vennestrøm, and Dr. Andrea Martini, who have shared ideas and provided valuable perspectives on the project. We had a lot of interesting and inspiring discussions. Thank you!

I would like to acknowledge the administration of the InnovaXN program and the administration of the doctoral school at the University of Turin for their efficiency and patience, which provided a conducive environment to explore, learn and evolve.

A special note of gratitude goes to my colleagues and friends at the ESRF, Dr. Olivier Mathon, Dr. Cesare Atzori, Dr. Davide Salusso, Sofia Balugani, Luca Bugarin, Clément Bonnet, and Dr. Elvina Dilmieva. Your wise advice has been an essential source of inspiration, and your support means a lot to me. I hope we stay in touch.

Finally, I am very grateful to my family, especially my mom, who has always supported every one of my ideas.

Thank you all for being a part of this journey!

8.1 InnovaXN project

This project has received funding from the European Union's Horizon 2020 research and innovation programme under the Marie Skłodowska-Curie grant agreement No 847439.

InnovaXN brings in collaboration two large-scale research facilities: European Synchrotron Radiation Facility (ESRF) and Institute Laue-Langevin (ILL), with Industrial partners and Universities. This project is a collaboration between the ESRF (BM23 and ID24 beamlines), the University of Turin, and Umicore, a leading European producer of automotive catalysts.

9 Appendix

The copies of the publications produced during the PhD are reported below.

JACS Au
AN OPEN ACCESS JOURNAL OF THE AMERICAN CHEMICAL SOCIETY

pubs.acs.org/jacsau

Letter

SO_2 Poisoning of Cu-CHA deNO_x Catalyst: The Most Vulnerable Cu Species Identified by X-ray Absorption Spectroscopy

Anastasia Yu. Molokova, Elisa Borfecchia, Andrea Martini, Ilia A. Pankin, Cesare Atzori, Olivier Mathon, Silvia Bordiga, Fei Wen, Peter N. R. Vennestrøm, Gloria Berlier, Ton V. W. Janssens,* and Kirill A. Lomachenko*

Cite This: *JACS Au* 2022, 2, 787−792

Read Online

ACCESS | Metrics & More | Article Recommendations | Supporting Information

ABSTRACT: Cu-exchanged chabazite zeolites (Cu-CHA) are effective catalysts for the NH_3-assisted selective catalytic reduction of NO (NH_3-SCR) for the abatement of NO_x emission from diesel vehicles. However, the presence of a small amount of SO_2 in diesel exhaust gases leads to a severe reduction in the low-temperature activity of these catalysts. To shed light on the nature of such deactivation, we characterized a Cu-CHA catalyst under well-defined exposures to SO_2 using *in situ* X-ray absorption spectroscopy. By varying the pretreatment procedure prior to the SO_2 exposure, we have selectively prepared Cu^I and Cu^{II} species with different ligations, which are relevant for the NH_3-SCR reaction. The highest reactivity toward SO_2 was observed for Cu^{II} species coordinated to both NH_3 and extraframework oxygen, in particular for $[Cu^{II}_2(NH_3)_4O_2]^{2+}$ complexes. Cu species without either ammonia or extraframework oxygen ligands were much less reactive, and the associated SO_2 uptake was significantly lower. These results explain why SO_2 mostly affects the low-temperature activity of Cu-CHA catalysts, since the dimeric complex $[Cu^{II}_2(NH_3)_4O_2]^{2+}$ is a crucial intermediate in the low-temperature NH_3-SCR catalytic cycle.

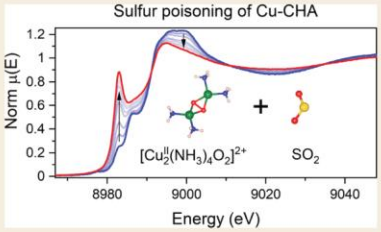

KEYWORDS: *selective catalytic reduction, Cu-CHA, deNO_x catalysis, sulfur poisoning, X-ray absorption spectroscopy, X-ray adsorbate quantification, XAS, XAQ*

The emission of nitrogen oxides (NO_x) from diesel vehicles is a global environmental challenge.[1,2] State of the art exhaust gas aftertreatment systems contain catalysts for selective catalytic reduction of NO_x by ammonia (NH_3-SCR), capable of reducing well over 90% of the NO_x emitted by the engine. In the NH_3-SCR reaction, NO reacts with NH_3 in the presence of O_2 to form N_2 and H_2O. At present, Cu-exchanged chabazites (Cu-CHA) are the preferred catalysts for NH_3-SCR, due to their superior low-temperature activity (150−350 °C)[3,4] and hydrothermal stability.[5,6] The temperature dependence of the NH_3-SCR activity of Cu-CHA catalysts shows a minimum at around 350 °C, which indicates that the reaction mechanism at low temperatures is different from that at higher temperatures.[7]

The NH_3-SCR reaction cycle for the low-temperature activity is a redox cycle, consisting of a series of oxidation and reduction steps, in which the oxidation state of Cu changes between Cu^I and Cu^{II}. The NO and NH_3 coordinate to Cu in the zeolite, giving rise to a variety of Cu species along the NH_3-SCR cycle.[8−11] The low-temperature activity of Cu-CHA catalysts originates from the ability to form mobile $Cu^I(NH_3)_2$ complexes under SCR conditions. Pairs of these species constitute the active Cu sites capable of O_2 activation via the formation of $[Cu^{II}_2(NH_3)_4O_2]^{2+}$ dimers around 200 °C, which is a crucial step in the NH_3-SCR reaction cycle.[12,13]

In practice, the application of Cu-CHA catalysts for the NH_3-SCR is restricted to ultralow-sulfur diesel fuels, due to the fact that a few ppm of SO_2 present in the exhaust gas drastically reduces the activity at low temperatures.[3,4,14] Multiple studies show that SO_2 affects the Cu mobility, the amount of Cu active sites,[14] and the redox behavior of the Cu in the NH_3-SCR cycle.[9,15] Most studies have focused on the overall effect of SO_2 on the performance of the catalysts,[14−21] while the chemistry behind SO_2 poisoning at the molecular level remains poorly understood. To determine a mechanism for SO_2 poisoning, one must identify the species in the Cu-CHA catalysts that interact with SO_2. To this end, we have selectively prepared well-defined Cu^I and Cu^{II} species with

Received: January 27, 2022
Revised: April 4, 2022
Accepted: April 5, 2022
Published: April 11, 2022

of the XANES data on the basis of references for the linear $[Cu^{I}(NH_3)_2]^+$ complex and pure $Cu^{II}(NH_3)_4$ groups (aqueous $[Cu^{II}(NH_3)_4]^{2+}$ or solid-state $[Cu^{II}(NH_3)_4]SO_4{\cdot}H_2O$) resulted in visible discrepancies with the data (Figure S7 in the Supporting Information). A better agreement is obtained when the spectrum of oxygen-bridged diamine dicopper complex $[Cu^{II}_2(NH_3)_4O_2]^{2+}$ is used as a Cu^{II} reference in combination with $[Cu^{I}(NH_3)_2]^+$, with approximately equal weights for each component (Figure 2). The necessary stock of available oxygen

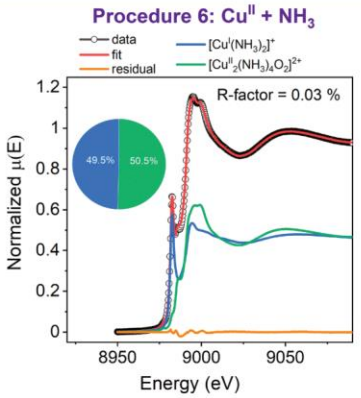

Figure 2. Linear combination fit of Cu K-edge XANES spectra obtained in Cu-CHA after exposing fw-Cu^{II} species to NH_3 at 200 °C (Cu^{II} + NH_3 pretreatment).

needed for the formation of the mixed-ligand species is expected to be present in the sample, as a wavelet analysis of the EXAFS collected after heating to 550 °C and cooling to 200 °C in 10% O_2/He flow reveals the presence of Cu−Cu scattering usually attributed to the oxygen-containing dimers[29,30] (Figure S8 in the Supporting Information), which may be susceptible to form mixed-ligand species upon exposure to NH_3.

The evolution of XANES spectra upon interaction with SO_2 shows that the most susceptible species are Cu^{II} with mixed $(NH_3)_xO_y$ ligation, whereas Cu^{I} species or Cu^{II} in the absence of NH_3 are much less affected. These findings are supported by X-ray adsorbate quantification (XAQ) data,[31] collected simultaneously with the XAS measurements during the exposure to SO_2, and a TPD analysis of a parallel set of catalyst samples, exposed to the same pretreatments used in XANES experiments (Figure 3a). We find the highest sulfur content (S/Cu ratio) for the $[Cu^{II}_2(NH_3)_4O_2]^{2+}$ and Cu^{II} + NH_3 procedures. The sulfur uptake of the $[Cu^{I}(NH_3)_2]^+$ and fw-Cu^{II} moieties was ca. 3 times lower, and for the bare fw-Cu^{I} species, it was ca. 6 times lower. These results show that the reaction between the $[Cu^{II}_2(NH_3)_4O_2]^{2+}$ species and SO_2 contributes the most to the accumulation of SO_2 in the Cu-CHA catalyst.

Interestingly, the sulfur content in the Cu^{II} + NH_3 sample lies between those for samples with pure $[Cu^{I}(NH_3)_2]^+$ and $[Cu^{II}_2(NH_3)_4O_2]^{2+}$ species, which in combination with the linear combination fit shown in Figure 2 suggests that the

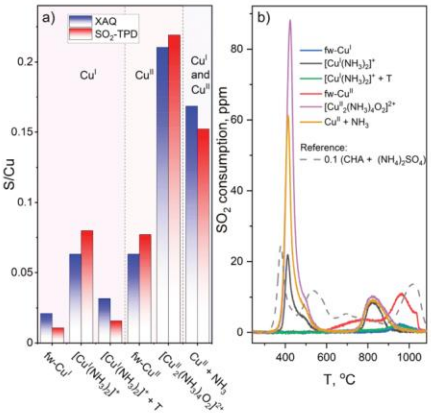

Figure 3. (a) S/Cu ratios in the samples after exposure to SO_2 obtained from SO_2-TPD and XAQ. (b) SO_2-TPD profiles collected after exposure of the species obtained in procedures 1−6 to SO_2 in comparison to a reference SO_2-TPD curve of a CHA zeolite without Cu impregnated with 20 wt % $(NH_4)_2SO_4$, downscaled ×10.

reactivity of the $Cu^{II}(NH_3)_xO_y$ species obtained after Cu^{II} + NH_3 treatment toward SO_2 is similar to that of $[Cu^{II}_2(NH_3)_4O_2]^{2+}$.

By comparing the SO_2-TPD curves of Cu-CHA samples with that of $(NH_4)_2SO_4$, adsorbed on Cu-free CHA (Figure 3b), we can also deduce that the elevated sulfur content in the samples with the $Cu^{II}(NH_3)_xO_y$ species is due to the reactivity toward SO_2 and not to the formation of $(NH_4)_2SO_4$ in a reaction of SO_2 with NH_3 and NH_4^+ groups stored in the zeolite framework. For the adsorbed $(NH_4)_2SO_4$, we observe SO_2 desorption at around 380, 530, and 1000 °C (gray curve in Figure 3b). The desorption at 380 °C matches the known thermal decomposition of $(NH_4)_2SO_4$;[32] the other two peaks are probably due to the interaction of either $(NH_4)_2SO_4$ or products of its decomposition with the zeolite, their precise interpretation being beyond the scope of the present argument. For all three Cu-CHA samples containing NH_3 before exposure to SO_2 ($[Cu^{I}(NH_3)_2]^+$, $[Cu^{II}_2(NH_3)_4O_2]^{2+}$, and ($Cu^{II}$ + NH_3) procedures), we observe SO_2 desorption at around 420 °C (Figure 3b). As this does not match any of the observed desorption characteristics of $(NH_4)_2SO_4$ in Cu-free Cu-CHA, the SO_2-TPD feature at 420 °C reflects an interaction of Cu with SO_2. Interestingly, the SO_2-TPD curve for the sample with the dominant fw-Cu^{II} species shows a significant SO_2 desorption peak close to 1000 °C, which, together with the lack of changes in Cu K-edge XANES upon exposure to SO_2, indicates the formation of some sulfur deposits not directly coordinated to Cu.

The presence of Cu−N and Cu−O bonds in the $[Cu^{II}_2(NH_3)_4O_2]^{2+}$ complex has been independently confirmed by valence-to-core XES.[27,33,34] XES spectra at different stages of pretreatment leading to the formation of $[Cu^{II}_2(NH_3)_4O_2]^{2+}$ dimers are reported in Figure 4. The origin of the Kβ'' satellite peak is the transition from the ligand s orbitals to Cu 1s, which makes its position sensitive to the species directly coordinated to Cu and allows it to discriminate

https://doi.org/10.1021/jacsau.2c00053
JACS Au 2022, 2, 787−792

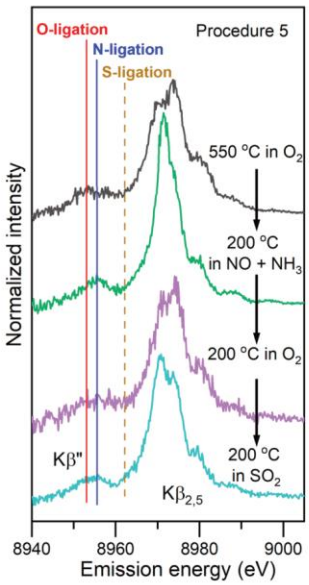

Figure 4. Background-subtracted Cu Kβ valence-to-core XES spectra for different stages of procedure 5 leading to the formation of the $[Cu^{II}_2(NH_3)_4O_2]^{2+}$ complex and its exposure to SO_2.

among Cu−O, Cu−N, and Cu−S bonds.[35−37] Figure 4 shows that after heating in O_2 Cu is predominantly coordinated by oxygens (as expected for the fw-Cu^{II} species), whereas after exposure to NO + NH_3 N ligands are dominating, as expected for a $[Cu^{I}(NH_3)_2]^+$ linear complex. After subsequent exposure to O_2 and formation of $[Cu^{II}_2(NH_3)_4O_2]^{2+}$ dimers, the peak broadens, confirming the presence of both Cu−N and Cu−O bonds. These bonds remain after exposure to SO_2, while no significant contribution from Cu−S bonds[38] is observed, suggesting that the possible SO_2 binding to the Cu is carried out through an oxygen atom.

In conclusion, the *in situ* XAS and XES measurements of different Cu intermediates formed in a Cu-CHA catalyst exposed to SO_2 demonstrate that Cu^{II} species with mixed NH_3 and O ligation of Cu are particularly reactive toward SO_2, whereas Cu^{I} species and Cu^{II} without NH_3 are much less affected by it. In particular, the $[Cu^{II}_2(NH_3)_4O_2]^{2+}$ complex, which is formed upon activation of O_2 in the NH_3-SCR cycle, shows a clear reaction with SO_2, resulting in a partial reduction of the Cu^{II} and accumulation of sulfur in the zeolite. Therefore, we conclude that this reaction is responsible for the poisoning of Cu-CHA catalysts in NH_3-SCR by SO_2.

■ ASSOCIATED CONTENT

Supporting Information

The Supporting Information is available free of charge at https://pubs.acs.org/doi/10.1021/jacsau.2c00053.

Experimental details, XANES linear combination fits before SO_2 exposure, wavelet transform analysis of the sample heated in O_2, and EXAFS fitting results (PDF)

■ AUTHOR INFORMATION

Corresponding Authors

Kirill A. Lomachenko − *European Synchrotron Radiation Facility, 38043 Grenoble Cedex 9, France;* orcid.org/0000-0003-0238-1719; Email: lomachenko@esrf.fr

Ton V. W. Janssens − *Umicore Denmark ApS, 2970 Hørsholm, Denmark;* orcid.org/0000-0002-1225-0942; Email: tonv.w.janssens@eu.umicore.com

Authors

Anastasia Yu. Molokova − *European Synchrotron Radiation Facility, 38043 Grenoble Cedex 9, France; Department of Chemistry and NIS Centre, University of Turin, 10125 Turin, Italy;* orcid.org/0000-0003-2053-2031

Elisa Borfecchia − *Department of Chemistry and NIS Centre, University of Turin, 10125 Turin, Italy;* orcid.org/0000-0001-8374-8329

Andrea Martini − *Department of Chemistry and NIS Centre, University of Turin, 10125 Turin, Italy; The Smart Materials Research Institute, Southern Federal University, 344090 Rostov-on-Don, Russia;* orcid.org/0000-0001-8820-2157

Ilia A. Pankin − *The Smart Materials Research Institute, Southern Federal University, 344090 Rostov-on-Don, Russia*

Cesare Atzori − *European Synchrotron Radiation Facility, 38043 Grenoble Cedex 9, France;* orcid.org/0000-0002-3227-7421

Olivier Mathon − *European Synchrotron Radiation Facility, 38043 Grenoble Cedex 9, France*

Silvia Bordiga − *Department of Chemistry and NIS Centre, University of Turin, 10125 Turin, Italy;* orcid.org/0000-0003-2371-4156

Fei Wen − *Umicore AG & Co, 63457 Hanau, Germany*

Peter N. R. Vennestrøm − *Umicore Denmark ApS, 2970 Hørsholm, Denmark;* orcid.org/0000-0002-6744-5640

Gloria Berlier − *Department of Chemistry and NIS Centre, University of Turin, 10125 Turin, Italy;* orcid.org/0000-0001-7720-3584

Complete contact information is available at: https://pubs.acs.org/10.1021/jacsau.2c00053

Funding

This project has received funding from the European Union's Horizon 2020 research and innovation programme under the Marie Skłodowska-Curie grant agreement No. 847439.

Notes

The authors declare no competing financial interest.

■ ACKNOWLEDGMENTS

ESRF is kindly acknowledged for the provision of beamtime at the BM23 and ID26 beamlines. We thank N. Daffé and B. Detlefs for help during the XES experiment at ID26.

■ REFERENCES

(1) Lambert, C. K. Perspective on SCR NO_x control for diesel vehicles. *React. Chem. Eng.* **2019**, *4* (6), 969−974.

(2) Gounder, R.; Moini, A. Automotive NO_x abatement using zeolite-based technologies. *React. Chem. Eng.* **2019**, *4* (6), 966−968.

(3) Hammershoi, P. S.; Jensen, A. D.; Janssens, T. V. W. Impact of SO_2-poisoning over the lifetime of a Cu-CHA catalyst for NH_3-SCR. *Appl. Catal., B* **2018**, *238*, 104−110.
(4) Hammershoi, P. S.; Jangjou, Y.; Epling, W. S.; Jensen, A. D.; Janssens, T. V. W. Reversible and irreversible deactivation of Cu-CHA NH_3-SCRcatalysts by SO_2 and SO_3. *Appl. Catal., B* **2018**, *226*, 38−45.
(5) Peden, C. H. F. Cu/Chabazite catalysts for 'Lean-Burn' vehicle emission control. *J. Catal.* **2019**, *373*, 384−389.
(6) Borfecchia, E.; Lomachenko, K. A.; Giordanino, F.; Falsig, H.; Beato, P.; Soldatov, A. V.; Bordiga, S.; Lamberti, C. Revisiting the nature of Cu-sites in activated Cu-SSZ-13 catalyst for SCR reaction. *Chem. Sci.* **2015**, *6*, 548−563.
(7) Gao, F.; Walter, E. D.; Kollar, M.; Wang, Y.; Szanyi, J.; Peden, C. H. F. Understanding ammonia selective catalytic reduction kinetics over Cu/SSZ-13 from motion of the Cu ions. *J. Catal.* **2014**, *319*, 1−14.
(8) Feng, Y.; Wang, X.; Janssens, T. V. W.; Vennestrøm, P. N. R.; Jansson, J.; Skoglundh, M.; Grönbeck, H. First-Principles Microkinetic Model for Low-Temperature NH_3-Assisted Selective Catalytic Reduction of NO over Cu-CHA. *ACS Catal.* **2021**, *11*, 14395−14407.
(9) Janssens, T. V. W.; Falsig, H.; Lundegaard, L. F.; Vennestrom, P. N. R.; Rasmussen, S. B.; Moses, P. G.; Giordanino, F.; Borfecchia, E.; Lomachenko, K. A.; Lamberti, C.; Bordiga, S.; Godiksen, A.; Mossin, S.; Beato, P. A Consistent Reaction Scheme for the Selective Catalytic Reduction of Nitrogen Oxides with Ammonia. *ACS Catal.* **2015**, *5* (5), 2832−2845.
(10) Gao, F.; Mei, D.; Wang, Y.; Szanyi, J.; Peden, C. H. Selective Catalytic Reduction over Cu/SSZ-13: Linking Homo- and Heterogeneous Catalysis. *J. Am. Chem. Soc.* **2017**, *139* (13), 4935−4942.
(11) Paolucci, C.; Khurana, I.; Parekh, A. A.; Li, S. C.; Shih, A. J.; Li, H.; Di Iorio, J. R.; Albarracin-Caballero, J. D.; Yezerets, A.; Miller, J. T.; Delgass, W. N.; Ribeiro, F. H.; Schneider, W. F.; Gounder, R. Dynamic multinuclear sites formed by mobilized copper ions in NO_x selective catalytic reduction. *Science* **2017**, *357* (6354), 898−903.
(12) Jones, C. B.; Khurana, I.; Krishna, S. H.; Shih, A. J.; Delgass, W. N.; Miller, J. T.; Ribeiro, F. H.; Schneider, W. F.; Gounder, R. Effects of dioxygen pressure on rates of NO_x selective catalytic reduction with NH_3 on Cu-CHA zeolites. *J. Catal.* **2020**, *389*, 140−149.
(13) Negri, C.; Selleri, T.; Borfecchia, E.; Martini, A.; Lomachenko, K. A.; Janssens, T. V. W.; Cutini, M.; Bordiga, S.; Berlier, G. Structure and Reactivity of Oxygen-Bridged Diamino Dicopper(II) Complexes in Cu-Ion-Exchanged Chabazite Catalyst for NH_3-Mediated Selective Catalytic Reduction. *J. Am. Chem. Soc.* **2020**, *142* (37), 15884−15896.
(14) Tang, Y. D.; Wang, D.; Wang, X.; Zha, Y. H.; An, H. M.; Kamasamudram, K.; Yezerets, A. Impact of low temperature sulfur exposure on the aging of small pore Cu-zeolite SCR catalyst. *Catal.* **2021**, *360*, 234−240.
(15) Mesilov, V. V.; Bergman, S. L.; Dahlin, S.; Yang, X.; Xi, S. B.; Ma, Z. R.; Lian, X.; Wei, C.; Pettersson, L. J.; Bernasek, S. L. Differences in oxidation-reduction kinetics and mobility of Cu species in fresh and SO_2-poisoned Cu-SSZ-13 catalysts. *Appl. Catal., B* **2021**, *284*, 119756.
(16) Mesilov, V.; Xiao, Y.; Dahlin, S.; Bergman, S. L.; Pettersson, L. J.; Bernasek, S. L. First-Principles Calculations of Condition-Dependent Cu/Fe Speciation in Sulfur-Poisoned Cu- and Fe-SSZ-13 Catalysts. *J. Phys. Chem. C* **2021**, *125* (8), 4632−4645.
(17) Feng, Y.; Janssens, T. V. W.; Vennestrøm, P. N. R.; Jansson, J.; Skoglundh, M.; Grönbeck, H. The Role of H^+- and Cu^+-Sites for N_2O Formation during NH_3-SCR over Cu-CHA. *J. Phys. Chem. C* **2021**, *125* (8), 4595−4601.
(18) Millan, R.; Cnudde, P.; van Speybroeck, V.; Boronat, M. Mobility and Reactivity of Cu^+ Species in Cu-CHA Catalysts under NH_3-SCR-NO_x Reaction Conditions: Insights from AIMD Simulations. *JACS Au* **2021**, *1* (10), 1778−1787.
(19) Krishna, S. H.; Jones, C. B.; Gounder, R. Temperature dependence of Cu(I) oxidation and Cu(II) reduction kinetics in the selective catalytic reduction of NO_x with NH_3 on Cu-chabazite zeolites. *J. Catal.* **2021**, *404*, 873−882.
(20) Mesilov, V. V.; Dahlin, S.; Bergman, S. L.; Xi, S.; Han, J.; Olsson, L.; Pettersson, L. J.; Bernasek, S. L. Regeneration of sulfur-poisoned Cu-SSZ-13 catalysts: Copper speciation and catalytic performance evaluation. *Appl. Catal., B* **2021**, *299*, 120626.
(21) Negri, C.; Borfecchia, E.; Martini, A.; Deplano, G.; Lomachenko, K. A.; Janssens, T. V. W.; Berlier, G.; Bordiga, S. In situ X-ray absorption study of Cu species in Cu-CHA catalysts for NH_3-SCR during temperature-programmed reduction in NO/NH_3. *Rev. Chem. Intermed.* **2021**, *47* (1), 357−375.
(22) Mathon, O.; Beteva, A.; Borrel, J.; Bugnazet, D.; Gatla, S.; Hino, R.; Kantor, I.; Mairs, T.; Munoz, M.; Pasternak, S.; Perrin, F.; Pascarelli, S. The time-resolved and extreme conditions XAS (TEXAS) facility at the European Synchrotron Radiation Facility: the general-purpose EXAFS bending-magnet beamline BM23. *J. Synchrotron Radiat.* **2015**, *22* (6), 1548−1554.
(23) Glatzel, P.; Harris, A.; Marion, P.; Sikora, M.; Weng, T. C.; Guilloud, C.; Lafuerza, S.; Rovezzi, M.; Detlefs, B.; Ducotte, L. The five-analyzer point-to-point scanning crystal spectrometer at ESRF ID26. *J. Synchrotron Radiat.* **2021**, *28*, 362−371.
(24) Borfecchia, E.; Negri, C.; Lomachenko, K. A.; Lamberti, C.; Janssens, T. V. W.; Berlier, G. Temperature-dependent dynamics of NH_3-derived Cu species in the Cu-CHA SCR catalyst. *React. Chem. Eng.* **2019**, *4* (6), 1067−1080.
(25) Martini, A.; Borfecchia, E.; Lomachenko, K. A.; Pankin, I. A.; Negri, C.; Berlier, G.; Beato, P.; Falsig, H.; Bordiga, S.; Lamberti, C. Composition-driven Cu-speciation and reducibility in Cu-CHA zeolite catalysts: a multivariate XAS/FTIR approach to complexity. *Chem. Sci.* **2017**, *8* (10), 6836−6851.
(26) Kau, L. S.; Spira-Solomon, D. J.; Penner-Hahn, J. E.; Hodgson, K. O.; Solomon, E. I. X-ray absorption edge determination of the oxidation state and coordination number of copper. Application to the type 3 site in Rhus vernicifera laccase and its reaction with oxygen. *J. Am. Chem. Soc.* **1987**, *109* (21), 6433−6442.
(27) Giordanino, F.; Borfecchia, E.; Lomachenko, K. A.; Lazzarini, A.; Agostini, G.; Gallo, E.; Soldatov, A. V.; Beato, P.; Bordiga, S.; Lamberti, C. Interaction of NH_3 with Cu-SSZ-13 Catalyst: A Complementary FTIR, XANES, and XES Study. *J. Phys. Chem. Lett.* **2014**, *5* (9), 1552−1559.
(28) Chen, L.; Janssens, T. V. W.; Vennestrom, P. N. R.; Jansson, J.; Skoglundh, M.; Gronbeck, H. A Complete Multisite Reaction Mechanism for Low-Temperature NH_3-SCR over Cu-CHA. *ACS Catal.* **2020**, *10* (10), 5646−5656.
(29) Martini, A.; Signorile, M.; Negri, C.; Kvande, K.; Lomachenko, K. A.; Svelle, S.; Beato, P.; Berlier, G.; Borfecchia, E.; Bordiga, S. EXAFS wavelet transform analysis of Cu-MOR zeolites for the direct methane to methanol conversion. *Phys. Chem. Chem. Phys.* **2020**, *22* (34), 18950−18963.
(30) Sushkevich, V. L.; Safonova, O. V.; Palagin, D.; Newton, M. A.; van Bokhoven, J. A. Structure of copper sites in zeolites examined by Fourier and wavelet transform analysis of EXAFS. *Chem. Sci.* **2020**, *11* (20), 5299−5312.
(31) Lomachenko, K. A.; Molokova, A. Y.; Atzori, C.; Mathon, O. Quantification of Adsorbates by X-ray Absorption Spectroscopy: Getting TGA-like Information for Free. *J. Phys. Chem. C* **2022**, *126* (11), 5175−5179.
(32) Kiyoura, R.; Urano, K. Mechanism, Kinetics, and Equilibrium of Thermal Decomposition of Ammonium Sulfate. *Ind. Eng. Chem. Process* **1970**, *9* (4), 489−494.
(33) Gunter, T.; Carvalho, H. W. P.; Doronkin, D. E.; Sheppard, T.; Glatzel, P.; Atkins, A. J.; Rudolph, J.; Jacob, C. R.; Casapu, M.; Grunwaldt, J. D. Structural snapshots of the SCR reaction mechanism on Cu-SSZ-13. *Chem. Commun.* **2015**, *51* (44), 9227−9230.
(34) Gunter, T.; Doronkin, D. E.; Boubnov, A.; Carvalho, H. W. P.; Casapu, M.; Grunwaldt, J. D. The SCR of NO_x with NH_3 Examined by Novel X-ray Emission and X-ray Absorption Methods. *Top. Catal.* **2016**, *59* (10−12), 866−874.
(35) Lomachenko, K. A.; Borfecchia, E.; Negri, C.; Berlier, G.; Lamberti, C.; Beato, P.; Falsig, H.; Bordiga, S. The Cu-CHA deNO$_x$ catalyst in action: temperature-dependent NH_3-assisted selective

https://doi.org/10.1021/jacsau.2c00053
JACS Au 2022, 2, 787−792

catalytic reduction monitored by operando XAS and XES. *J. Am. Chem. Soc.* **2016**, *138* (37), 12025−12028.
(36) Glatzel, P.; Bergmann, U. High resolution 1s core hole X-ray spectroscopy in 3d transition metal complexes - electronic and structural information. *Coord. Chem. Rev.* **2005**, *249* (1−2), 65−95.
(37) Vegelius, J. R.; Kvashnina, K. O.; Klintenberg, M.; Soroka, I. L.; Butorin, S. M. Cu $K\beta_{2,5}$ X-ray emission spectroscopy as a tool for characterization of monovalent copper compounds. *J. Anal. At. Spectrom.* **2012**, *27* (11), 1882−1888.
(38) Muller, P.; Neuba, A.; Florke, U.; Henkel, G.; Kuhne, T. D.; Bauer, M. Experimental and Theoretical High Energy Resolution Hard X-ray Absorption and Emission Spectroscopy on Biomimetic Cu_2S_2 Complexes. *J. Phys. Chem. A* **2019**, *123* (16), 3575−3581.

https://doi.org/10.1021/jacsau.2c00053
JACS Au 2022, 2, 787−792

THE JOURNAL OF PHYSICAL CHEMISTRY C
A JOURNAL OF THE AMERICAN CHEMICAL SOCIETY

pubs.acs.org/JPCC

Article

Quantification of Adsorbates by X-ray Absorption Spectroscopy: Getting TGA-like Information for Free

Kirill A. Lomachenko,* Anastasia Yu. Molokova, Cesare Atzori, and Olivier Mathon

Cite This: *J. Phys. Chem. C* 2022, 126, 5175−5179

Read Online

ACCESS | Metrics & More | Article Recommendations | Supporting Information

ABSTRACT: Hard X-ray absorption spectroscopy (XAS) is frequently applied in catalysis and gas sorption studies to monitor changes in oxidation states, coordination numbers, and interatomic distances of active sites under *in situ* and *operando* conditions. However, transmission XAS data can reveal also the change in the total amount of guest species adsorbed on the whole sample. Surprisingly, to the best of our knowledge, the latter property has never been exploited. Here, we present a simple method to quantify the amount of adsorbates from XAS data collected during the interaction of the sample with gases or liquids. The method relies on monitoring the change of the total absorption level below the measured absorption edge and does not require any additional instrumentation or modification of the XAS data collection procedure. Essentially, it is a way to obtain the information analogous to the one delivered by temperature-programmed reduction (TPR), temperature-programmed desorption (TPD), or thermogravimetric analysis (TGA) directly from XAS at no extra cost.

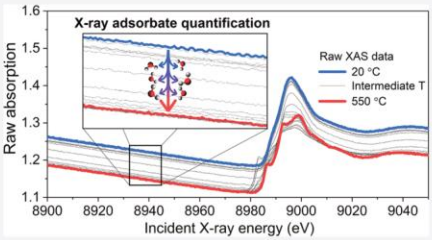

INTRODUCTION

X-ray absorption spectroscopy (XAS) is a versatile element-selective tool to determine the parameters of local atomic and electronic structure of materials, such as interatomic distances, bond angles, coordination numbers, and oxidation states.[1,2] Elemental selectivity is an advantage of the XAS-based methods, which is particularly important in chemical studies where the research interest is focused on particular minority species (active sites) arranged inside the hosting matrices. This is often the case of functionalized MOFs, metal-exchanged zeolites, supported nanoparticles, and doped oxides (the list is certainly not exhaustive). High penetration depth of hard X-rays allows to collect data under *in situ* and *operando* conditions, which is particularly useful in catalysis.

XAS measurements are mainly conducted at synchrotron beamlines, so the availability of the method is much lower compared to the laboratory techniques. To get the most from the beamtime, *in situ* and *operando* XAS experiments are often accompanied by simultaneous complementary measurements, such as X-ray diffraction, mass spectrometry, infrared spectroscopy, gas chromatography, UV−vis spectroscopy, etc. Such an approach yields complementary datasets collected in identical conditions, providing extra information about the sample and serving as diagnostics to compare the conditions at the beamline with those adopted in the laboratory.

Despite their obvious value for gas sorption and catalytic studies, thermogravimetric analysis (TGA) and techniques for gas adsorption/desorption quantification such as temperature-programmed desorption or reduction (TPD/TPR) are seldom coupled with XAS measurements in the same experiment due to difficulties in constructing the combined setup and different requirements for sample preparation. To address this problem, here, we suggest a simple method to extract TGA/TPD/TPR-like information directly from XAS data, hereafter designated X-ray adsorbate quantification (XAQ).

METHODS

While the X-ray absorption near-edge structure (XANES) and the extended X-ray absorption fine structure (EXAFS) comprise features at or above the absorption edge, XAQ focuses on the flat region at approximately 50−150 eV below the absorption edge. Adsorption or desorption of molecules caused by the variation of external conditions (temperature, gas feed, irradiation) change the total absorption coefficient of the sample, causing the vertical shift of the spectrum. The XAQ method essentially relates the amplitude of this shift to the amount of adsorbed or desorbed species.

The experimentally observed change of the total absorption $\Delta\mu_{tot}$ in two different measurements has two main contributions

Received: January 11, 2022
Revised: February 23, 2022
Published: March 14, 2022

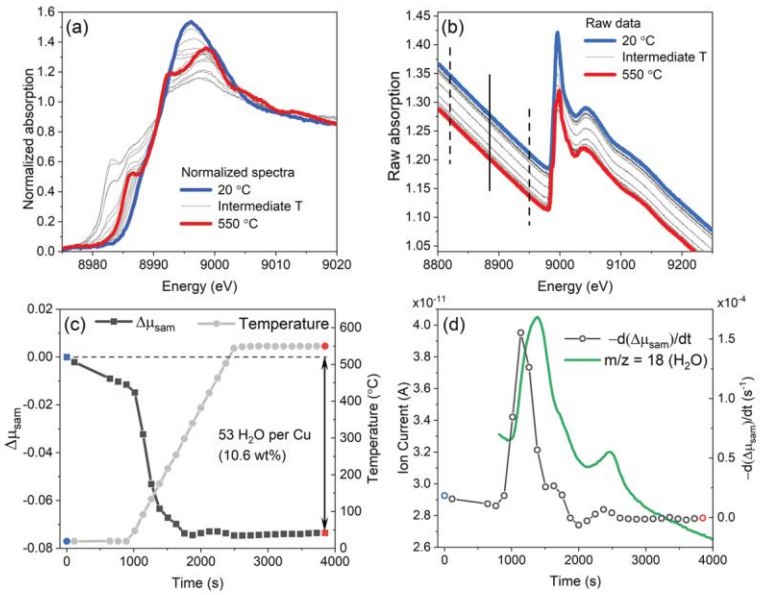

Figure 1. (a) Normalized Cu K-edge XANES spectra collected during heating of Cu-CHA zeolite from RT to 550 °C in 10% O_2/He flow. (b) Same data without normalization. Dashed lines indicate the XAQ fitting region and solid line shows its center where the total absorption is evaluated. (c) XAQ signal during heating (left) and temperature profile (right). (d) Time derivative of the XAQ signal (left axis) and water mass-spectrometer signal collected simultaneously with the XAS measurements.

$$\Delta\mu_{tot} = \Delta\left(\ln\frac{I_0}{I_1}\right) = \Delta\mu_{sam} + \Delta\mu_{gas} \tag{1}$$

where μ_{sam} and μ_{gas} are the total absorption of the sample and the gas inside the experimental cell, respectively; I_0 and I_1 are the counts of the ionization chambers measuring the intensity of the incident and transmitted radiation, respectively.

$\Delta\mu_{tot}$ can be obtained directly from the experimental data by calculating the difference of the total absorption in the XAQ region between the first spectrum of the procedure of interest and each consecutive spectrum. To increase precision, the XAQ region of around 50−100 eV can be fitted by a straight line and its value in the center of the region can be taken as μ_{tot} for each spectrum.

$\Delta\mu_{gas}$ is negligible compared to $\Delta\mu_{sam}$ when the concentration of reactive components is limited to a few hundred ppm, the rest being light He carrier gas, or when the temperature, pressure, and composition of the gas feed do not change. Otherwise, it has to be calculated using the simple expression provided in the Supporting Information (SI).

Measuring $\Delta\mu_{tot}$ and calculating (or neglecting) $\Delta\mu_{gas}$ allows to calculate $\Delta\mu_{sam}$

$$\Delta\mu_{sam} = \Delta\mu_{tot} - \Delta\mu_{gas} \tag{2}$$

which can then be directly linked to the molar surface density of adsorbed or desorbed species Θ_{ads} (that is, the amount of moles of the adsorbate per unit area of the sample surface exposed to the X-ray beam) by the following expression (derivation provided in the SI)

$$\Theta_{ads} = \Delta\mu_{sam}\left(2r_e\lambda N_A\sum_j N_j f_j''\right)^{-1} \tag{3}$$

where r_e is the electron radius, λ is the X-ray wavelength, N_A is the Avogadro number, N_j and f_j'' are the number of atoms and imaginary part of the atomic scattering factor of jth atomic species constituting the molecule of adsorbates.

Since the mass, bulk density, elemental composition, and shape (e.g., diameter of the pressed pellet or capillary with loose powder) of the sample are usually known, obtaining Θ_{ads} then allows to calculate the adsorption capacity (in moles of adsorbates per unit mass of the sample)

$$n_{ads} = \frac{\Theta_{ads}}{\rho_{sam}^{A}} \tag{4}$$

where ρ_{sam}^{A} is the surface density of the sample. It is equally straightforward to obtain a molar ratio between the adsorbates and particular atomic species present in the sample.

Calculation (3) can be carried out using the existing codes to optimize the mass or thickness of the samples for XAS measurements, such as XAFSmass,[3] all terms being either tabulated[4,5] or known from the experimental conditions. Very similar calculations with the same codes are required to

https://doi.org/10.1021/acs.jpcc.2c00226
J. Phys. Chem. C 2022, 126, 5175−5179

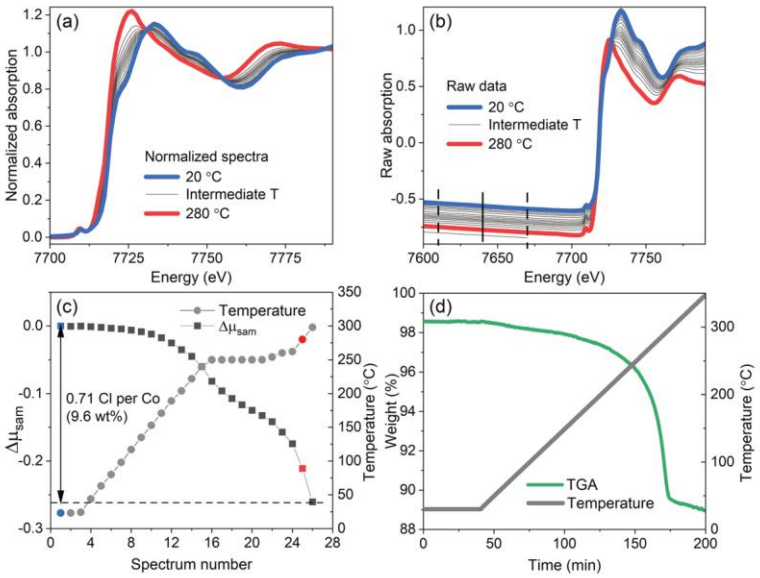

Figure 2. (a) Normalized Co K-edge XANES spectra collected during the heating of Co_2Cl_4BTDD MOF from RT to 290 °C in He flow. (b) Same data without normalization. Dashed lines indicate the XAQ fitting region and solid line shows its center where the total absorption is evaluated. (c) XAQ signal during heating (left) and temperature profile (right). The point at 300 °C corresponds to the spectrum that was stopped after the data in the XAQ region were collected (bottom-most curve in panel b). (d) TGA of the same material performed separately. Panel (a) adapted with permission from Tulchinsky et al.,[9] copyright 2017 American Chemical Society.

calculate the absorption edge step for each sample, so the majority of XAS users are already familiar with them.

■ RESULTS AND DISCUSSION

To illustrate the possibilities of the XAQ approach, Figure 1 shows the activation of copper-exchanged chabazite zeolite (Cu-CHA) with Si/Al = 6.7 and Cu/Al = 0.06, employed as the deNO_x catalyst. The sample was heated in the flow of 10% O_2 in He flow (100 mL/min) from room temperature to 550 °C at the BM23 beamline of the ESRF.[6] This treatment causes the dehydration of the zeolite and coordination of the isolated Cu centers to the zeolitic framework (Figure 1a).

The evolution of Cu K-edge XANES spectra agrees well with the literature data for Cu-CHA zeolites with similar Cu/Al and Si/Al ratios.[7,8] The usual way of presenting normalized XANES data, such as in Figure 1a, however, does not allow to appreciate the change of the total absorption level due to desorption of water. However, in the raw data, the vertical shift of the spectra is clearly visible (Figure 1b). The corresponding XAQ signal shows a pronounced time and temperature dependence (Figure 1c) with the dehydration being completed at around 300 °C, equivalent to desorption of ca. 53 water molecules per Cu ion, or 10.6 wt % of the whole material (details of the calculation are presented in the SI). It is in good agreement with the TGA value of 11.7 wt %, the slight discrepancy being due to the partial dehydration of the sample in the dry gas flow during the alignment of the pellet under the beam before the first XAS spectrum was measured. Water desorption was also confirmed by a mass spectrometer connected to the outlet of the experimental cell during the XAS experiment (Figure 1d). Notably, the derivative of the XAQ signal agrees well with the signal of m/z = 18 (water), showing even faster and sharper time response due to its insensitivity to the large dead volume of the experimental cell that affects the MS data.

Another example of application of the XAQ technique is dechlorination of the Co_2Cl_4BTDD (BTDD = bis(1H-1,2,3-triazolo[4,5-*b*],[4,5-i])dibenzo[1,4]dioxin) metal-organic framework.[9] This material was the first MOF reported to reversibly capture and release halogens, such as chlorine and bromine. The Co(III)−Co(II) redox process accompanying the desorption of one chlorine per Co during heating to 300 °C was revealed by XANES spectroscopy (Figure 2a).[9] The resulting XANES spectrum of the MOF after heating was similar to the one of the parent Co_2Cl_2BTDD Co(II) MOF before chlorination, thus proving the reversibility of the process. However, the amount of desorbed chlorine was not measured during the XAS experiment, which did not make possible direct comparison of XAS conditions with those employed for separate TGA measurements. The advantage of the XAQ method is that it allows such quantification even if it was not foreseen in the original experiment. Since the XAS data were collected including more than 100 eV below the absorption edge (Figure 2b), XAQ signal could be reliably

https://doi.org/10.1021/acs.jpcc.2c00226
J. Phys. Chem. C 2022, 126, 5175−5179

extracted from raw data (Figure 2c). The drop in the total absorption was equivalent to the loss of around 0.71 Cl atoms per Co, constituting 9.6 wt % of the material. It is in good agreement with the value of ca. 9.5 wt % obtained by TGA (Figure 2d).[9] These data ensure the compatibility of the conditions employed for TGA measurements with those during the synchrotron XAS experiment, thus confirming the reliability of the collected XAS data.

As demonstrated above, the XAQ method delivers the information analogous to the one typically obtained from TGA or TPD/TPR. Importantly, with XAQ, this information is collected at the same time, in the same conditions and from the same spot on the sample as the XAS data, which ensures perfect compatibility of the two datasets.

Nonetheless, there are several important points to be considered when assessing the feasibility of XAQ extraction from XAS data. In particular, $\Delta\mu_{sam}$ exhibits strong dependence on the atomic number of the adsorbates and the energy of the incident radiation, which can be approximately expressed as $\Delta\mu_{sam} \propto \frac{Z^4}{E^3}$. It makes the detection of heavy adsorbates easier compared to the light ones and leads to a significant decrease of the XAQ contrast at high energy, which makes the quantification of low amounts of light adsorbates difficult at high-energy edges.

In addition, inhomogeneities of the sample can introduce errors in the XAQ signal during the temperature ramps if the experimental cell moves with respect to the beam because of the thermal expansion. This effect is detrimental also for the XAS data quality and therefore should be avoided regardless of the need for XAQ measurements by designing the experimental cells with minimal thermal expansion, by compensating for the thermal expansion moving the sample stage, or by preparing highly homogeneous samples.

Finally, a significant temperature gradient may exist along the X-ray optical path inside the sample cell, so the average temperature of the gas mixture may be different from the sample temperature. Assessing this gradient by an additional thermocouple would allow to decrease the associated error in the calculation of $\Delta\mu_{gas}$ in the experiments with varied temperature. Alternatively, $\Delta\mu_{gas}$ can be measured directly by conducting XAS scans without the sample in the short pre-edge region at the temperatures of interest. An ultimate solution would be to use experimental cells with short optical path and diluted gas mixtures, thus decreasing the absolute value of $\Delta\mu_{gas}$.

CONCLUSIONS

To summarize, the XAQ method allows to determine from the transmission XAS data the amount of guest species adsorbed on the sample during the interaction with reactive gases or liquids. While it is unreasonable to perform a synchrotron XAS experiment only to obtain XAQ data, an important advantage of XAQ is that it can be extracted from properly collected transmission XAS spectra without any modification of the experimental procedure or need for additional equipment or software. Notably, combining XAQ with XANES/EXAFS does not cause an increase in the measurement time because the data in the XAQ region usually are collected anyway, being essential for normalization of the XANES and EXAFS spectra. The method offers a possibility to get quantitative information analogous to what is usually obtained by TPD, TPR, or TGA but simultaneously with XAS measurements and essentially at no extra cost with respect to the performed XAS experiment.

ASSOCIATED CONTENT

Supporting Information

The Supporting Information is available free of charge at https://pubs.acs.org/doi/10.1021/acs.jpcc.2c00226.

Derivation of expression (3); accounting for gas inside the reactor cell; quantification of adsorbates for the cases reported in Figures 1 and 2 (PDF)

AUTHOR INFORMATION

Corresponding Author

Kirill A. Lomachenko − *European Synchrotron Radiation Facility, 38043 Grenoble, France;* orcid.org/0000-0003-0238-1719; Email: lomachenko@esrf.fr

Authors

Anastasia Yu. Molokova − *European Synchrotron Radiation Facility, 38043 Grenoble, France; Department of Chemistry and NIS Centre, University of Turin, 10125 Turin, Italy;* orcid.org/0000-0003-2053-2031

Cesare Atzori − *European Synchrotron Radiation Facility, 38043 Grenoble, France;* orcid.org/0000-0002-3227-7421

Olivier Mathon − *European Synchrotron Radiation Facility, 38043 Grenoble, France*

Complete contact information is available at: https://pubs.acs.org/10.1021/acs.jpcc.2c00226

Notes

The authors declare no competing financial interest.

ACKNOWLEDGMENTS

The authors thank S. Bordiga, E. Borfecchia, and G. Berlier (University of Turin, Italy) for fruitful discussions, T.V.W. Janssens, F. Wen, and P.N.R. Vennestroem (Umicore, Denmark) for providing the Cu-CHA sample, and M. Dincă and Y. Tulchinsky (MIT, USA) for providing the TGA data of Co_2Cl_4BTDD MOF. This project has received funding from the European Union's Horizon 2020 research and innovation programme under the Marie Skłodowska−Curie grant agreement no. 847439.

REFERENCES

(1) Bordiga, S.; Groppo, E.; Agostini, G.; van Bokhoven, J. A.; Lamberti, C. Reactivity of Surface Species in Heterogeneous Catalysts Probed by In Situ X-ray Absorption Techniques. *Chem. Rev.* **2013**, *113*, 1736−1850.

(2) Timoshenko, J.; Cuenya, B. R. In Situ/Operando Electrocatalyst Characterization by X-ray Absorption Spectroscopy. *Chem. Rev.* **2021**, *121*, 882−961.

(3) Klementiev, K.; Chernikov, R. XAFSmass: a program for calculating the optimal mass of XAFS samples. *J. Phys.: Conf. Ser.* **2016**, *712*, No. 012008.

(4) Chantler, C. T. Theoretical form-factor, attenuation and scattering tabulation for Z=1-92 from E=1-10 eV to E=0.4-1.0 MeV. *J. Phys. Chem. Ref. Data* **1995**, *24*, 71−591.

(5) Henke, B. L.; Gullikson, E. M.; Davis, J. C. X-ray interactions - photoabsorption, scattering, transmission, and reflection at E=50-30,000 eV, Z=1-92. *At. Data Nucl. Data Tables* **1993**, *54*, 181−342.

(6) Mathon, O.; Beteva, A.; Borrel, J.; Bugnazet, D.; Gatla, S.; Hino, R.; Kantor, I.; Mairs, T.; Munoz, M.; Pasternak, S.; et al. The time-resolved and extreme conditions XAS (TEXAS) facility at the

European Synchrotron Radiation Facility: the general-purpose EXAFS bending-magnet beamline BM23. *J. Synchrotron Radiat.* **2015**, *22*, 1548−1554.
(7) Paolucci, C.; Parekh, A. A.; Khurana, I.; Di Iorio, J. R.; Li, H.; Caballero, J. D. A.; Shih, A. J.; Anggara, T.; Delgass, W. N.; Miller, J. T.; et al. Catalysis in a Cage: Condition-Dependent Speciation and Dynamics of Exchanged Cu Cations in SSZ-13 Zeolites. *J. Am. Chem. Soc.* **2016**, *138*, 6028−6048.
(8) Negri, C.; Martini, A.; Deplano, G.; Lomachenko, K. A.; Janssens, T. V. W.; Borfecchia, E.; Berlier, G.; Bordiga, S. Investigating the role of Cu-oxo species in Cu-nitrate formation over Cu-CHA catalysts. *Phys. Chem. Chem. Phys.* **2021**, *23*, 18322−18337.
(9) Tulchinsky, Y.; Hendon, C. H.; Lomachenko, K. A.; Borfecchia, E.; Melot, B. C.; Hudson, M. R.; Tarver, J. D.; Korzyński, M. D.; Stubbs, A. W.; Kagan, J. J.; et al. Reversible Capture and Release of Cl_2 and Br_2 with a Redox-Active Metal−Organic Framework. *J. Am. Chem. Soc.* **2017**, *139*, 5992−5997.

https://doi.org/10.1021/acs.jpcc.2c00226
J. Phys. Chem. C 2022, 126, 5175−5179